

AD-A082 823

STANFORD UNIV CALIF DEPT OF CIVIL ENGINEERING

F/G 20/4

FINITE ELEMENT SIMULATION OF SIMPLE THREE-DIMENSIONAL FULLY CAV-ETC(U)

NOV 79 P Y KO, R L STREET

N00014-75-C-0277

UNCLASSIFIED

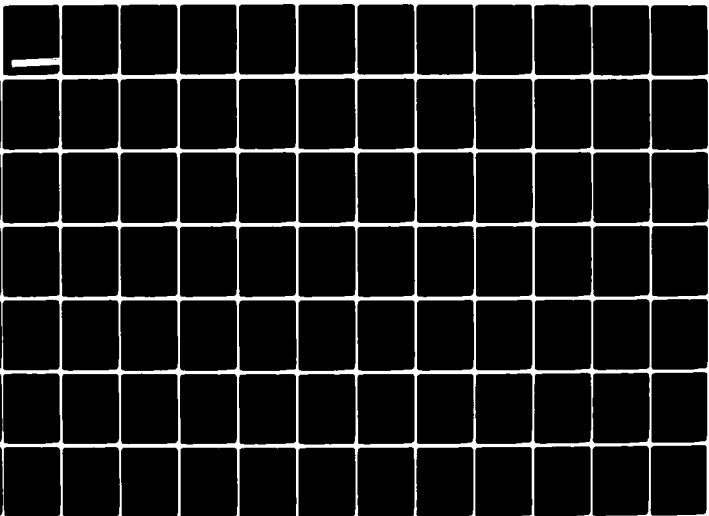
TR-241

NL

FIG 2

AD-A

UB-753



LEVEL II

12

ADA 082823

# FINITE ELEMENT SIMULATION OF SIMPLE THREE-DIMENSIONAL FULLY CAVITATING FLOWS

by  
Peter Y. Ko  
Robert L. Street

SDTIC  
ELECTED  
APR 7 1980  
C

This research was carried out under the General Hydromechanics  
Research Program (SR 023 01 01) of the Naval Sea Systems Command  
and administered by the Naval Ship Research and Development Center

Approved for public release;  
distribution unlimited.



Department of CIVIL ENGINEERING  
STANFORD UNIVERSITY

80 4 7 127

FILE COPY

Department of Civil Engineering  
Stanford University  
Stanford, California 94305

FINITE ELEMENT SIMULATION OF SIMPLE  
THREE-DIMENSIONAL FULLY CAVITATING FLOWS

by

Peter Y. Ko  
Robert L. Street

TECHNICAL REPORT NO. 241

November 1979



This research was carried out under the General Hydromechanics  
Research Program (SR 023 01 01) of the Naval Ship Systems  
Command and administered by the Naval Ship Research and  
Development Center

Approved for public release;  
distribution unlimited.

## ABSTRACT

Based on potential flow theory, a formulation is given for three-dimensional fully cavitating flow with a Riabouchinsky model. The model is nonlinear and the location of the free surface of the cavity is not known priori. Therefore, an iterative procedure is used to locate the free surface boundary. The employment of a trial-free-boundary approach effectively reduces the fully nonlinear model to a linear one, and the solution at each iteration is obtained by means of the finite element method (FEM). Examples studied were fully cavitating flow past flat plates in a water tunnel. Results are given for pure drag flows past circular and elliptic plates and a lifting flow past a circular plate.

Three-dimensional, 20-node, quadratic isoparametric finite elements are used. The locations of the mid-side nodes on the free-surface just off the edge of the plate are found to have significant effects on the separation condition which must be enforced while keeping the Jacobian of the isoparametric transformation nonsingular. The free surface is shown to be a characteristic surface and this leads to the development of a weighting scheme for assigning the free surface potential in the iterative scheme the shifting of the free surface. A new three-dimensional "local" interpolation scheme for the location of the mid-side nodes is also developed for the lifting flow configuration.

The various algorithms were tested against known analytic solutions as well as published numerical and experimental results in two-dimensional and axisymmetric flows. Results from several pure-drag three-dimensional geometries are presented and the cavity shapes and the tunnel wall effects are examined. Then lifting flow results are given.

Because of the change in flow boundary conditions at the separation edge and the failure of the FEM to resolve these conditions accurately, the ability of the numerical solution to maintain a constant pressure over the entire cavity decreases as the three dimensionality of the free surface increases. However, the present procedure produces absolutely stable iterations and shows no sign of drifting of the free surface. It is found that satisfaction of a tangent separation condition of the free

surface from the flat plate body is crucial for the stability of the iterative procedure. Grid refinement in both the streamwise and transverse directions reduces the computational error. While free surface movement between iterations is a useful convergence criterion, a flow-rate balance between upstream and downstream cross-sections appears not to be a good criterion. Finally, alternate formulations which may reduce the difficulties encountered are discussed.

# ACKNOWLEDGEMENTS

The authors are grateful to Dr. Ralph T. Cheng, the United States Geological Survey, and Professor E. Y. Hsu, Stanford University, for their wise counsel. We are indebted to Professor Bruce E. Larock, University of California, Davis, for his assistance by providing the results of his research to us and especially to Dr. C. Taylor, University College of Wales, Swansea, who provided us with the computerprogram PHREATIC3, which forms the basis of the present code.

We would like to thank the staffs of the Computer Center at the Stanford Linear Accelerator Center for providing their help which prevented our computation task from turning into a dilemma, and Mr. David Barbe for his excellence in preparing the illustrations and drafting.

This research was carried out under the General Hydromechanics Research Program (SR-023-01-01) of the Naval Ship Systems Command and administered by the Naval Ship Research and Development Center.

Accession For	
NTIS	<input checked="" type="checkbox"/> CRA&I
DDC TAB	<input type="checkbox"/>
Unannounced	<input type="checkbox"/>
Justification	
By	
Distribution/	
Availability Codes	
Dist	Availability or special
A	

## TABLE OF CONTENTS

ABSTRACT	iii
ACKNOWLEDGMENTS	v
LIST OF TABLES	viii
LIST OF FIGURES	ix
NOMENCLATURE	xi
1. INTRODUCTION	1
1.1 OVERVIEW	1
1.2 REVIEW OF NUMERICAL TECHNIQUES	3
1.2.1 Two-Dimensional Methods	3
1.2.2 Three-Dimensional Methods	4
2. FORMULATION FOR FULLY CAVITATING FLOWS	6
2.1 PHYSICAL MODEL DESCRIPTIONS	6
2.2 FINITE ELEMENT MODEL	9
2.2.1 Finite Element Approximation	10
2.2.2 Isoparametric Transformation and Numerical Integration	13
2.2.3 Implementation of Boundary Conditions	16
2.2.3.1 Flux Boundary--Uniform Flow Upstream	16
2.2.3.2 Boundary Conditions on the Free Surface	18
2.2.3.3 Effect of Midside Node Locations at Separation	18
2.3 COMPUTATION OF AREAS AND FLOWS	21
2.4 CHARACTERISTICS OF THE FREE SURFACE	23
3. ITERATIVE PROCEDURE	26
3.1 OVERVIEW OF THE ITERATIVE PROCEDURE	26
3.2 INTERPOLATION AND EXTRAPOLATION SCHEMES	29
3.2.1 For the Pure Drag Case	29
3.2.2 For the Lifting Flow Case	30
3.3 WEIGHTING SCHEME AT THE FREE SURFACE	32
4. IMPLEMENTATIONS AND TESTS	36
4.1 SPECIFIED IMPLEMENTATIONS	36
4.2 VERIFICATION OF ALGORITHMS	37
4.2.1 Two-Dimensional Geometries	38
4.2.2 Three-Dimensional Geometry	39

5.	CAVITY FLOW RESULTS	41
5.1	RESULTS FOR THREE-DIMENSIONAL, PURE DRAG CASES	42
5.1.1	Circular Plates in Square Water Tunnels	42
5.1.2	Elliptic Plates in Rectangular Water Tunnels	44
5.2	RESULTS FOR A THREE-DIMENSIONAL LIFTING FLOW	44
6.	PERFORMANCE OF THE SOLUTION AND ALTERNATIVE FORMULATIONS	46
6.1	THE NATURE OF THE ITERATIVE PROCESS	46
6.2	ACCURACY OF THE SOLUTIONS	49
6.2.1	Review of Tests and Relevant Results	49
6.2.2	Potential Means to Reduce Solution Errors	55
6.3	ALTERNATIVE FORMULATIONS	57
6.3.1	Other Finite Elements	58
6.3.2	The Boundary Integral Equation Method (BIEM)	59
7.	SUMMARY AND FUTURE WORK	61
	REFERENCES	63
	APPENDIX 1 -- MESH GENERATION AND ELEMENT ORGANIZATION	66
A.1.1	Pure Drag Case	66
A.1.2	Lifting Flow Case	67
	APPENDIX 2 -- LARGE MATRIX EQUATION SOLVING ALGORITHM	68
A.2.1	The Direct Method by Gaussian Elimination	68
A.2.2	Iterative Conjugate Gradient Method	69
A.2.3	Numerical Test	73



# LIST OF TABLES

Table 5.1	Summary of Results for Circular Plates in Square Water Tunnels	74
Table 5.2	Summary of Results for Elliptic Plates in Rectangular Water Tunnels	75

## LIST OF FIGURES

- Figure 2.1      Riabouchinsky cavity flow model
- Figure 2.2      Schematic of finite element solution domain
- Figure 2.3      The isoparametric finite element
- Figure 2.4      Schematic of initial cavity flow problem
- Figure 2.5      Schematic of streamline integration of velocity potential  $\phi$
- Figure 2.6      Element at separation showing quarter point location
- Figure 3.1      Definition of node point locations for periodic cubic spline interpolation
- Figure 3.2      Schematic of node point movement for lifting flow
- Figure 3.3      The three-dimensional isoparametric interpolation
- Figure 4.1      Two-dimensional cavity flow configuration
- Figure 4.2      Sequence of convergence of free surface for the two-dimensional cavity flow
- Figure 4.3      Comparison of simulation of axisymmetric cavity flow by three-dimensional model and Brennen's results (1969). Curves are from Brennen (1969)
- Figure 4.4      Demonstration of convergence of free-surface shifting algorithm
- Figure 5.1      Variation of cavity shape with tunnel width and plate diameter ratio.  $P = 2$ ;  $L = 5$ ; cross-sections just off disk and at cavity mid-section
- Figure 5.2      Variation of cavity shape with tunnel width and plate diameter ratio.  $P = 2$ ;  $L = 10$ ; cross-sections at X-locations indicated
- Figure 5.3      Variation of  $\sigma$  and cavity width with relative tunnel width -- the wall effect
- Figure 5.4      Variation of cavity shape with tunnel size and plate diameter ratio for elliptic plates. Cross-sections as indicated
- Figure 5.5      Finite element grid and configuration of three-dimensional lifting cavity flow; angle of attack =  $60^\circ$
- Figure 5.6      Final cavity shape for the lifting cavity flow with circular plate

- Figure 5.7 Pressure distribution along the centerline of the plate; angle of attack =  $60^\circ$
- Figure 5.8 Pressure distribution  $C_p^*$  on plate; angle of attack =  $60^\circ$
- Figure 6.1 Grid refinement at separation
- Figure 6.2 Effect of grid refinement near separation in circular-plate pure-drag cases:  $W/P = 2.5$ ;  $\sigma = 1.25$
- Figure 6.3 Effect of tunnel size on separation velocities in circular-plate pure drag cases:  $\Delta x P = 0.075$
- Figure 6.4 Variation of freestream velocity  $V_{fs}$  (as a percentage difference from the average freestream velocity) for a circular plate pure drag case
- Figure 6.5 Variation of freestream velocity  $V_{fs}$  for elliptic case E2
- Figure 6.6 Pure drag cases: variation of freestream velocity across end of cavity (as a difference percentage from the average freestream velocity)
- Figure 6.7 Grid refinement for lifting plate case
- Figure A.1.1 Curvilinear axes for node numbering: (a) main flow section  
(b) rod section
- Figure A.1.2 Schematic of the geometry generation procedure for pure drag quarter flow
- Figure A.1.3 Schematic of the geometry generation procedure for lifting flow
- Figure A.1.4 Top view of a typical grid for lifting flow; angle of attack of  $60^\circ$
- Figure A.1.5 Schematic of semi-manual grid adjustment at the separation for the lifting flow
- Figure A.2.1 Schematic diagram showing the data structure for direct method which uses Gaussian Elimination
- Figure A.2.2 Maximum error as defined in Step 3 of CG algorithm versus iteration number for the test problem

# NOMENCLATURE

A	area of the foil
$A_s$	surface area of an element
B	width of the cavity at the centerline
$C_D$	drag coefficient
$C_L$	lift coefficient
$C_D^*$	normalized drag coefficient: $C_D^* = D/(\frac{1}{2}\rho q_c^2 S)$
$C_L^*$	normalized lift coefficient: $C_L^* = \bar{L}/(\frac{1}{2}\rho q_c^2 S)$
$C_p^*$	normalized pressure coefficient: $C_p^* = (P - P_c)/(\frac{1}{2}\rho q_c^2)$
D	half-depth of the water tunnel
$E_i$	equivalent nodal value due to a uniform surface load
F	force on the foil
J	Jacobian matrix for the isoparametric transformation
$K_{ij}^e$	elemental stiffness matrix
$K_{ij}$	global stiffness matrix
$\ell_i$	direction cosine
$\bar{L}$	lift
L	half-length of cavity
$N_i$	shape functions
P	pressure (Section 2)
P	radius of circular plate or minor axis of elliptic plate
$P_\infty$	upstream pressure
$P_c$	pressure in cavity
$P_p$	Pressure at the plate
$P_{2n}$	polynomial of degree 2n
q	magnitude of the velocity vector

$q_c$	magnitude of the velocity vector on the free surface
$q_p$	magnitude of the velocity vector at the foil
$q_s$	magnitude of the velocity vector along a streamline
$Q$	flow through arbitrary cross-section (Section 2)
$Q$	major axis of elliptic plate
$R_i$	forcing terms due to flux boundary
$r$	polar coordinate
$S$	largest possible projected area of the foil (Section 2.1)
$S$	curvilinear streamwise coordinate
$U_\infty$	uniform horizontal upstream velocity
$v$	velocity in y-direction
$V$	average free-stream velocity on the free-surface
$V_C$	average velocity contributed by all elements at a node
$V_F$	average velocity at separation contributed by elements on the free surface
$V_S$	average velocity at separation contributed by elements on the solid boundary
$w$	velocity in z-direction
$W$	half-width of water tunnel
$x$	Cartesian coordinate
$y$	Cartesian coordinate
$z$	Cartesian coordinate
$\alpha$	curvilinear axis
$\bar{\alpha}$	angle of attack
$\beta$	curvilinear axis
$\gamma$	curvilinear axis
$\delta_{ij}$	Dirac Delta function
$\epsilon$	criterion for convergence

$\zeta$	axis in the three-dimensional isoparametric space
$\eta$	axis in the three-dimensional isoparametric space
$\theta$	polar coordinate
$\nu$	nodal connection matrix
$\xi$	axis in the three-dimensional isoparametric space
$\rho$	fluid density
$\sigma$	cavitation number
$\phi$	velocity potential
$\Phi$	boundary values of
$\omega_i$	weights for the Gaussian integration formula
$\overline{\omega_i}$	area of influence of node i
$\Omega$	solution domain

## 1. INTRODUCTION

### 1.1 OVERVIEW

The analytical study of wake and cavity flows began in the 19th century when Kirchhoff introduced an idealized, inviscid-flow, infinite-length-cavity model with free streamlines and solved the accompanying problem via the conformal-mapping technique. Since then, numerous researchers have investigated different aspects of the problem, both analytically and numerically. The development of underwater missiles, high speed hydrofoils and propellers accelerated the research efforts on the analysis of and design for cavity flows. Models were subsequently formed to investigate flows with finite cavities. The Riabouchinsky model, the re-entrant jet model, the open wake model and the vortex model are some of those being used (see, e.g., Wu, 1972).

Cavity flow problems, as represented by potential flow models, are nonlinear. The problems are complicated by the unknown shape and location of the free boundary. For two-dimensional cavity flows, methods, such as the hodograph mapping which is derived from the theory of analytic functions, can be employed to transform the problems onto complex planes where the problem is solved by singular-integral-equation techniques. The evaluation of these functional equations is very difficult in general because of the nonlinearity. But, by and large, the two-dimensional problem for steady state flows has been solved (Tulin, 1963; Street and Larock, 1968; Wu, 1968).

Though efforts have been made to solve the three-dimensional case, there is still no known exact solution or generally usable and fully nonlinear model for the analysis of the three-dimensional fully cavitating flow (see the review of numerical methods for solution of three-dimensional cavity flow problems by Street, 1977). He points out that the techniques for the numerical solution of three-dimensional, fully cavitating flows, based on linearized methods and the method of matched asymptotic expansions, are presently available. However, he also points out that these techniques rely on the use of two-dimensional characteristics of the flow applied strip-wise in the three-dimensional flow field and that the area of fully nonlinear methods is still developing.

Among the linearized models are Widnall's (1966) lifting-surface model, which was found to compare unsatisfactorily with experimental data by Tsen and Guilbaud (1974). The disagreement was credited to the non-linearity of the physical problem. Nishiyama (1970), with the assumption of large aspect ratios, was able to reduce the lifting-surface problem to a lifting-line problem but achieved similar results as Widnall (1966). Jiang and Leehey (1977) combined the essence of these two theories and produced calculations that appear to be the best within the limitations of the linearized theory.

Furuya (1975), using two-dimensional nonlinear streamline theory in the near field and Prandtl's lifting line theory for the far field, and Leehey and Stellingner (1975), using higher order perturbation theory, have gone beyond the linearized models and developed, not linear, but yet not fully nonlinear models. Neither model accounts for wall effects, although Furuya's (1975) model can handle the motion of foils beneath free surfaces in water of infinite depth. A three-dimensional fully nonlinear model is needed for the study of hydrofoils with finite-aspect-ratio and the interpretation of the results from water tunnel tests. It was, therefore, the goal of this research to develop a computational procedure for the simulation of three-dimensional flow about fully cavitating hydrofoils.

Numerical techniques which are commonly used in free surface flow computations are reviewed in Section 1.2. Section 2.1 describes the physical formulation while Section 2.2 gives the finite element (FE) approximation of the three-dimensional fully cavitating flow problem. The computation of flow rates and areas in the FE representation is described in Section 2.3. Section 2.4 describes the characteristic of the free surface which leads to the development of a weighting scheme described in Section 3 together with the iterative procedure for the location of the free surface. Section 4 then gives the implementations and tests of the algorithms while computation results are given in Section 5. Section 6 contains a discussion errors and alternative approaches. Section 7 combines the conclusions and suggestions of possible future work.



## 1.2 REVIEW OF NUMERICAL TECHNIQUES

There are several major categories of numerical techniques which can be applied to free surface flows. There are finite-difference and finite-element methods. Amongst the finite-difference methods one finds formulations in which the problem is solved in a stream function and velocity potential space or in which the solution is found from the distribution of singularities on the free surface of the flow (normally called a boundary integral technique). The application of all these techniques to both two- and three-dimensional free surface flow problems is described below.

### 1.2.1 Two-Dimensional Methods

Mogel and Street (1974) used a finite-difference technique and solved a problem of flow past a disk in a water tunnel by employing a Riabouchinsky model and imaging to achieve an exact formulation. Irregular finite-difference stars were employed along the curved free surface boundary. A very refined finite-difference grid was also used in the neighborhood of the separation point on the flat plate. The solution of the finite-difference equations for the velocity component was achieved by successive over-relaxation. Because the velocity components were employed as the unknowns, the solution required simultaneous satisfaction of the Laplace equation for each velocity component and of the nonlinear free surface boundary conditions. The solution converged and gave reasonable results. However, the cost for the two-dimensional case was subsequently found to be equal to the cost for a solution of similar accuracy for a three-dimensional disk-in-water-tunnel flow by the finite-element method (see Sec. 5).

Brennen (1969) combined a finite-difference technique with a mapping to stream function--velocity potential space to solve the axisymmetric flow past a circular disk in a circular water tunnel using a Riabouchinsky model. A difficulty with the extension of this technique to more general bodies is that the solution is inverse because the stream function--velocity potential space solution must be mapped back to physical space to obtain the final geometry. Brennen's results are used for comparisons with the finite element solution obtained from the three-dimensional model later in the present work.

White and Kline (1975) developed a general method for the solution of turbulent, separated, axisymmetric flows. In their general development they employed a new boundary integral technique for the potential flowfield outside the boundary layers developing in their diffuser flows. Unlike grid techniques, the boundary integral method requires computation of unknowns only over the flow boundary. The solution technique obtains the potential flow from the numerical solution of Green's third identity and iteratively solves for the correct location of an initially unknown free surface. In principle this technique can be extended to general three-dimensional flows. Interestingly, a very similar technique was developed in 1953 by Armstrong and Dunham (1953). They applied a vortex sheet singularity to free streamline flows, thereby generating an integral equation whose solution formed part of an iterative procedure to locate the initially unknown free surface. They solved several axisymmetric cavity flows in an infinite fluid field and obtained reasonable agreement with experiment.

The application of the finite element method to free streamline flows was first made by Chan, et al. (1973 a,b). They showed that the finite element method could be used to solve for the velocity potential in two-dimensional and axisymmetric ideal fluid flows involving a free surface. Sarpkaya and Hiriart (1975) applied a similar technique to solve the free streamline problem of flow in curved jet deflectors.

#### 1.2.2 Three-Dimensional Methods

Jeppson (1972) developed an inverse formulation for three-dimensional flows in which he defined a velocity potential and two additional functions which defined the flow paths. By changing the conventional roles played by the variables of the problem, he converted a free surface with an unknown position in physical space into a plane of known position in the inverse stream function--velocity potential space. The technique is very similar to that of Brennen (1969) cited above and suffers the same disadvantage, namely that the shape of curved solid bodies cannot be prescribed in advance in physical space.

Larock and Taylor (1976) applied finite-element techniques to solve the jetflow from a circular pipe and orifice under the influence of gravity.

The resulting flow is slightly three-dimensional, namely, the jet remains essentially circular but droops under the action of gravity creating a three-dimensional flowfield. They employed the velocity potential as the dependent variable and quadratic isoparametric finite elements in the flow-field discretization. Again, as in other free streamline problems, an iterative procedure had to be used to determine the free surface location whose precise location is initially unknown. They found "convergent" solutions when the jet is not too far from being horizontal (i.e., at high Froude number). However, they reported that "a number of small shifts (of the free surface between two consecutive iterations) can accumulate to a nonnegligible effect." Plausible reasons for the inability of their procedure to converge at low Froude numbers and for the drift of their solution are advanced later herein as the present work is described.

In summary, the works of Mogel and Street (1974), Brennen (1969), and Larock and Taylor (1976) are of special interest. Although developed only for two-dimensional flow and based on a finite difference scheme, Mogel and Street (1974) provided the basic framework for the present study and development of a three-dimensional finite element model. Brennen (1969) found good agreement between his solution and experiments. Hence, his problem was solved herein by the finite element method as a check of the present three-dimensional model. Larock and Taylor (1976) provide an illustration of the application of the finite element method to a three-dimensional problem and gave us insight to problems to be expected and key features to be incorporated into a model.

## 2. FORMULATION FOR FULLY CAVITATING FLOWS

### 2.1 PHYSICAL MODEL DESCRIPTIONS

One common consideration which enters into the development of cavity flow models is the problem of the closure of the cavity. In the Riabouchinsky model, the closure of the cavity is achieved by a mirror image of the foil in the downstream direction as shown in Figure 2.1, with section C being the plane of symmetry. In the present study, the Riabouchinsky model centered within a water tunnel of uniform geometric cross-section is used. It is assumed that both ends of the water tunnel can be extended far away from the foils so that a uniform horizontal velocity can be maintained at the entrance. Because of the symmetry in the flow geometry, only one-eighth (for the pure drag case) or one-quarter (for the lifting case) of the flow field need to be considered.

The flow is assumed to be incompressible, steady and irrotational. Hence, it is governed by the velocity potential  $\phi$  which satisfies the Laplace equation, in Cartesian coordinates,

$$\frac{\partial^2 \phi}{\partial x^2} + \frac{\partial^2 \phi}{\partial y^2} + \frac{\partial^2 \phi}{\partial z^2} = 0 \quad (2.1)$$

within the flow field and

$$\begin{aligned} u &= - \frac{\partial \phi}{\partial x} \\ v &= - \frac{\partial \phi}{\partial y} \\ w &= - \frac{\partial \phi}{\partial z} \end{aligned} \quad (2.2)$$

where  $u$ ,  $v$  and  $w$  are the components of the velocity in the  $x$ ,  $y$ , and  $z$  directions, respectively. Their magnitude  $q = (u^2 + v^2 + w^2)^{1/2}$ . If the effect of gravity is neglected, the Bernoulli equation becomes

$$P + \frac{1}{2} \rho q^2 = \text{constant} \quad (2.3)$$

where  $P$  is the pressure and  $\rho$  is the fluid density. Since the free surface is also a constant pressure surface, from the Bernoulli equation, Equation 2.3,

$$u^2 + v^2 + w^2 = q^2 = \text{constant} \quad (2.4)$$

on the free surface and the change of velocity potential  $\phi$  on the free surface along a streamline is given as

$$-\frac{\partial \phi}{\partial s} = q \quad (2.5)$$

Also the free surface can be described by the streamline conditions, namely,

$$\frac{dx}{u} = \frac{dy}{v} = \frac{dz}{w} \quad (2.6)$$

which mean that the velocity vector is tangent to the free surface.

Because of the symmetry of the flow model, the plane of symmetry (section C, Figure 2.1) of the Riabouchinsky model is also an equipotential surface. Without loss of generality, the potential there can be set to zero. With a prescribed uniform horizontal upstream flow (with velocity  $U_\infty$ ) and no flux conditions at solid boundaries (tunnel walls and the foil), the problem is well defined. However, the location of the free surface is not known a priori. An iterative procedure is described in Section 3 for determining the location of, as well as the constant pressure condition on, the free surface. As a result of using such a trial-free-boundary method, only a linear system of equations has to be solved at each iteration.

The most important nondimensional parameter for cavity flows is the cavitation number  $\sigma$  defined as

$$\sigma = \frac{P_\infty - P_c}{\frac{1}{2} \rho U_\infty^2} \quad (2.7)$$

where the subscript  $c$  denotes the cavity. Equality of cavitation numbers is an indication of the dynamic similarity of two geometrically similar cavity flows. Using Equation 2.3, one can show that

$$\sigma = \frac{q_c^2}{U_\infty^2} - 1 \quad (2.8)$$

The force on the foil is given by

$$F = \int_A (P_p - P_c) dA \quad (2.9)$$

where subscript  $p$  denotes the foil (a plate herein) and  $A$  is the area of the foil. From Equations 2.3 and 2.9,

$$F = \frac{\rho q_c^2 A}{2} - \frac{\rho}{2} \int_A q_p^2 dA \quad (2.10)$$

For the pure drag problem,  $F$  is the drag. For a plate at an angle of attack  $\bar{\alpha}$  the drag  $D$  is given by

$$D = F \sin \bar{\alpha}$$

and the lift  $\bar{L}$  is given by

$$\bar{L} = F \cos \bar{\alpha} . \quad (2.12)$$

The drag and lift coefficients,  $C_D$  and  $C_L$  respectively, are given as follows:

$$C_D = \frac{D}{\frac{1}{2} \rho U_\infty^2 s} \quad (2.13)$$

and

$$C_L = \frac{\bar{L}}{\frac{1}{2} \rho U_\infty^2 s} \quad (2.14)$$

where  $S$  is defined as the largest possible projected area of the foil. It is often convenient to normalize  $C_L$  and  $C_D$  on the velocity  $q_c$  on the free surface. Then,

$$C_D^* = C_D / (1 + \sigma) = \frac{D}{\frac{1}{2} \rho q_c^2 S} \quad (2.13a)$$

and

$$C_L^* = C_L / (1 + \sigma) = \frac{\bar{L}}{\frac{1}{2} \rho q_c^2 S} \quad (2.14a)$$

where the relationship between  $\sigma$ ,  $q_c$  and  $U_\infty$  is given by Equation 2.8.

## 2.2 FINITE ELEMENT MODEL

The finite element method (FEM) was originally developed in the 1950's in the field of structural engineering and used because of its efficiency in stress analysis of large structural systems. Since then, the FEM has become one of the commonly used methods for the approximate numerical solution of a wide spectrum of engineering problems. One of the advantages of the finite element approximation is its simplicity and efficiency for handling irregular boundaries and variation in mesh sizes which are necessary to the solution of free surface problems.

In the FEM, the solution domain is discretized into subregions, called elements, which are defined by their node points (often located at the corners and mid-sides of elements). The FEM then represents the problem solution as a continuous function by using approximation or interpolation functions within each element. These functions are defined in terms of the solution values at the finite set of node points. The solution varies locally within each element according to the form determined by the interpolation function; these normally are prescribed via a summation of a set of shape (or basis) functions. Partial differential equations are then transformed to integral equation formulations which are subsequently replaced by a well-posed set of algebraic equations for the values at the node points.

### 2.2.1 Finite Element Approximation

As described in Section 2.1, the fully cavitating flow problem is nonlinear because of the unknown location of the free surface. However, the nonlinear solution can be achieved by solving a series of linear problems through the use of an iterative procedure which is described in Section 3. It is the linear problem associated with each iteration which is solved by means of the FEM. In particular the velocity potential  $\phi$  is determined for a given configuration then the result is used to determine a more accurate free surface shape. As the application of the FEM to general field problems, i.e., the determination of  $\phi$ , is well documented (see, e.g., Huebner, 1975), only a brief description is given here.

The solution domain  $\Omega$  is discretized into the subregion elements. Each element is defined by node points as shown in Figure 2.2. The continuous unknown function  $\phi$  is approximated by the interpolation function determined by the unknown values  $\phi_i$  at all the node points in the domain. The local variation of the solution within each element is determined by the shape functions because the solution is expressed as a linear combination of the products of the values of the shape functions and the  $\phi_i^e$ , defined at each node point of the element, i.e.,

$$\phi^e = \sum_{i=1}^n N_i \phi_i^e \quad (2.15)$$

where the superscript  $e$  denotes values for element  $e$ . The subscript  $i$  denotes values defined for the  $i^{\text{th}}$  node point,  $n$  is the total number of node points for each element and  $N_i$  are the shape functions;  $\phi_i^e$  is a subset of  $\phi_i$ .

Shape functions are classified by two characteristics, viz., first, the degree of variation within each element, such as linear, quadratic, etc., and, second, the order of continuity of the solution function  $\phi$  between elements, e.g.,  $C^0$  continuity to ensure the continuity of the solution function between boundaries of elements,  $C^1$  continuity to ensure the continuity of the solution function as well as its first derivatives between boundaries of elements, and so on. However, all shape functions satisfy the following condition:



$$N_i(x_j, y_j, z_j) = \delta_{ij} \quad (2.16)$$

The total number of node points  $n$  per element is fixed by the choice of shape functions. The choice of the shape function for the present study is addressed later in this section.

The linear problem to be solved at each iteration is the Laplace equation for the velocity potential  $\phi$ , namely,

$$\frac{\partial}{\partial x_i} \left( \frac{\partial \phi}{\partial x_i} \right) = 0 \quad \text{in } \Omega \quad (2.17)$$

(summation notation is used) with boundary conditions

$$(a) \quad \phi = \phi(x_i) \quad \text{on } S_1 \quad (2.18)$$

$$(b) \quad \frac{\partial \phi}{\partial x_i} l_i + g(x_i) = 0 \quad \text{on } S_2 \quad (2.19)$$

where  $l_i$  are the direction cosines of the outward normal to the surface  $S_2$  (Figure 2.2). This problem is actually solved by application of the variational (Ritz) approach, which uses the variational form of the differential equation rather than the differential equation itself. Thus, the solution  $\phi$  minimizes the functional

$$I(\phi) = \frac{1}{2} \int_{\Omega} \left( \frac{\partial \phi}{\partial x_i} \right)^2 dx_i + \int_{S_2} g\phi dS_2 \quad (2.20)$$

It can be shown that there exist a set of values  $\phi_i$ , defined at all the node points of a finite element mesh, which yield, through the basic functions, the best approximation to the continuous solution  $\phi$  of the differential equation. It can also be shown that this best approximation is unique (Prenter 1975, p. 196). If the total functional is taken to be the sum over all elements, minimization of the functional, Equation 2.20, leads to the following:

$$\begin{aligned}
\frac{\partial I}{\partial \phi_1} &= 0 = \sum_{\text{all elements}} \frac{\partial I^e}{\partial \phi_1} \\
&= \sum_{\text{all elements}} \left\{ \int_{\Omega^e} \left[ \frac{\partial \phi^e}{\partial x} \frac{\partial}{\partial \phi_1} \left( \frac{\partial \phi^e}{\partial x} \right) + \frac{\partial \phi^e}{\partial y} \frac{\partial}{\partial \phi_1} \left( \frac{\partial \phi^e}{\partial y} \right) + \frac{\partial \phi^e}{\partial z} \frac{\partial}{\partial \phi_1} \left( \frac{\partial \phi^e}{\partial z} \right) \right] d\Omega \right. \\
&\quad \left. + \int_{S_2^e} g \frac{\partial \phi^e}{\partial \phi_1} dS_2 \right\} \quad (2.21)
\end{aligned}$$

The validity of the summation on the righthand side of Equation 2.21 is assured by the right choice of shape functions. Zienkiewicz (1971, Section 3.2) gives two criteria to be satisfied by the chosen shape functions. The shape functions chosen herein meet these criteria; in particular, as only the function  $\phi$  and its first derivatives appear in (2.21), a  $C^0$  element and its shape functions are needed.

From Equations 2.15 and 2.21, one obtains, for each element,

$$K_{ij}^e \phi_j^e + R_i^e = 0 \quad (2.22)$$

where the elemental "stiffness" matrix  $K_{ij}^e$  is given by

$$K_{ij}^e = \int_{\Omega^e} \left( \frac{\partial N_i}{\partial x} \frac{\partial N_j}{\partial x} + \frac{\partial N_i}{\partial y} \frac{\partial N_j}{\partial y} + \frac{\partial N_i}{\partial z} \frac{\partial N_j}{\partial z} \right) d\Omega^e \quad (2.23)$$

and the forcing term due to the flux boundary condition on  $S_2$  is given by

$$R_i^e = \int_{S_2^e} g N_i dS_2 \quad (2.24)$$

Note that, if none of the node points of an element is on  $S_2$ , the forcing term  $R_i^e$  vanishes. The global equation is obtained by summing over the elemental equations, i.e.,

$$K_{ij} \phi_j + R_i = 0 . \quad (2.25)$$

Equation 2.25 is a set of linear algebraic equations from which the  $\phi_i$  can be obtained. The global stiffness matrix  $K_{ij}$  is positive definite and symmetric. Both direct and iterative methods for solving this large sparse linear system are reviewed in Appendix 2.

### 2.2.2 Isoparametric Transformation and Numerical Integration

In order to handle irregular boundaries and variation in mesh sizes, a special class of finite elements, the isoparametric finite elements, is used. The idea of using elements with curved sides seems to have originated with Taig (1961) and was generalized by Irons (1966) and Ergatoudis, et al. (1968). The isoparametric transformation uses a set of shape functions to map an irregularly shaped element, which is defined in physical space by means of its node points, onto a regular cube defined in a local coordinate system as shown in Figure 2.3.

Herein, a set of quadratic shape functions is employed. Accordingly in three-dimensions, each isoparametric,  $C^0$ , finite element has 20 node points. The transformation is given explicitly as

$$\left. \begin{aligned} x &= \sum_{i=1}^{20} N_i x_i \\ y &= \sum_{i=1}^{20} N_i y_i \\ z &= \sum_{i=1}^{20} N_i z_i \end{aligned} \right\} \quad (2.26)$$

where  $N_i = N_i(\xi, \eta, \zeta)$  are the shape functions. For isoparametric elements, the shape functions  $N_i$  employed in the coordinate transformation (Equation 2.26) are the same as those employed to represent the unknown field variables (see Equation 2.15). The quadratic shape functions appropriate for the 20-node "serendipity" element (Huebner, 1975) used here are:

for corner nodes, i.e.,  $\xi_1 = \eta_1 = \zeta_1 = \pm 1$  :

$$N_1 = \frac{1}{8}(1 + \xi\xi_1)(1 + \eta\eta_1)(1 + \zeta\zeta_1)(\xi\xi_1 + \eta\eta_1 + \zeta\zeta_1 - 2)$$

for midside nodes at  $\xi_1 = 0$ ,  $\eta_1 = \zeta_1 = \pm 1$  :

$$N_1 = \frac{1}{4}(1 - \xi^2)(1 + \eta\eta_1)(1 + \zeta\zeta_1)$$

for midside nodes at  $\eta_1 = 0$ ,  $\xi_1 = \zeta_1 = \pm 1$  :

$$N_1 = \frac{1}{4}(1 + \xi\xi_1)(1 - \eta^2)(1 + \zeta\zeta_1)$$

for midside nodes at  $\zeta_1 = 0$ ,  $\xi_1 = \eta_1 = \pm 1$  :

$$N_1 = \frac{1}{4}(1 + \xi\xi_1)(1 + \eta\eta_1)(1 - \zeta^2)$$

(2.27)

These  $N_1$  satisfy the constraint, Equation 2.16.

The essence of the transformation is contained in the Jacobian matrix:

$$J = \begin{bmatrix} \frac{\partial x}{\partial \xi} & \frac{\partial y}{\partial \xi} & \frac{\partial z}{\partial \xi} \\ \frac{\partial x}{\partial \eta} & \frac{\partial y}{\partial \eta} & \frac{\partial z}{\partial \eta} \\ \frac{\partial x}{\partial \zeta} & \frac{\partial y}{\partial \zeta} & \frac{\partial z}{\partial \zeta} \end{bmatrix} \quad (2.28)$$

which is unique for every element. Hence, the derivatives of the shape functions are related as

$$\begin{Bmatrix} \frac{\partial N_1}{\partial \xi} \\ \frac{\partial N_1}{\partial \eta} \\ \frac{\partial N_1}{\partial \zeta} \end{Bmatrix} = [J] \begin{Bmatrix} \frac{\partial N_1}{\partial x} \\ \frac{\partial N_1}{\partial y} \\ \frac{\partial N_1}{\partial z} \end{Bmatrix} \quad (2.29)$$

It can also be shown that

$$dx dy dz = |J| d\xi d\eta d\zeta \quad (2.30)$$

However, this transformation is valid if and only if the Jacobian  $|J|$  is nonsingular in an element. If the transformation is consistent, then the sign of the Jacobian  $|J|$  is the same in all elements. It is well known (see, e.g., Strang et al. 1973, 3.3) that all interior angles at the corners of an element should be bounded between 0 and  $\pi$ , and the midside nodes must lie in the middle half of the sides of the element to guarantee nonsingular Jacobians. It is also true that unique relations between the physical  $(x, y, z)$  and local  $(\xi, \eta, \zeta)$  coordinate systems do not exist for elements which fold back upon themselves, i.e., those with singular Jacobians.

Whenever an unique transformation exists, the integration of any function, say  $u(x, y, z)$ , defined in physical space can be performed in isoparametric space (local coordinate system) such that

$$\iiint_{\Omega} u(x, y, z) dx dy dz = \int_{-1}^{+1} \int_{-1}^{+1} \int_{-1}^{+1} u(x(\xi, \eta, \zeta), y(\xi, \eta, \zeta), z(\xi, \eta, \zeta)) \cdot |J| d\xi d\eta d\zeta \quad (2.31)$$

The triple integral on the righthand side of Equation 2.31 can be approximated by means of a Gauss-Legendre quadrature formula which will integrate exactly a polynomial of degree  $2n - 1$  or less as follows

$$\int_{-1}^{+1} P_{2n-1} dx = \sum_{i=1}^n \omega_i P_{2n-1}(x_i) \quad (2.32)$$

where  $x_i$  are the zeroes of the Legendre polynomial of degree  $n$  and  $\omega_i$  are the weights. For a triple integral,

$$\int_{-1}^{+1} \int_{-1}^{+1} \int_{-1}^{+1} u(\xi, \eta, \zeta) d\xi d\eta d\zeta = \sum_{i=1}^n \sum_{j=1}^n \sum_{k=1}^n \omega_i \omega_j \omega_k u(\xi_i, \eta_j, \zeta_k) \quad (2.33)$$

The locations and the corresponding weights can be found in subroutine Gauss described in the Program Manual (Ko and Street, 1979).

### 2.2.3 Implementation of Boundary Conditions

With an assumed location of the free surface, the geometry of the flow field is defined and can be discretized. As noted in Section 2.1, only one-eighth (for the pure drag case) or one-quarter (for the lifting case) of the total flow needs to be considered because of the symmetry of the flow geometry. A schematic of the flow field employed in the FEM solution (for a pure drag case) is shown in Figure 2.4 for the purpose of illustrating the boundary conditions. It is obvious that no-flux conditions are required at the tunnel wall, the plane of symmetry and the surface of the foil as indicated in Figure 2.4. Actually the free surface is also a no-flux boundary. However, the no flux conditions is satisfied only if the free surface is at its true location, where the constant pressure conditions is also satisfied. Therefore, the no-flux condition cannot be imposed at the free surface during the iterative procedure, but the final solution must satisfy such a condition.

#### 2.2.3.1 Flux Boundary--Uniform Flow Upstream

A uniform flow  $U_{\infty}$  is imposed at some reasonable distance upstream from the foil or plate. Because the FEM expresses the continuous solution of the problem in terms of the values at node points, flow distributed over the surface of an element has to be represented by the equivalent nodal values specified at the node points which define the surface. Zienkiewicz (1971, p. 168) has given some distribution values for the allocation of a unit uniform surface load for rectangular surfaces when the mid-side nodes are placed at exactly the 1/2 (quadratic shape function) or 1/3 (cubic shape function) points along the sides of the elements. However, for surfaces with curved sides or where the mid-side nodes are not at symmetrical locations, one has to evaluate an integral for the equivalent nodal values  $E_1$  due to a uniform surface load as follows:

$$E_1 = \iint U_{\infty} N_1 \, dx dy = U_{\infty} \iint N_1 \, dx dy = U_{\infty} \bar{\omega}_1 \quad (2.34)$$

where  $E_i$  is the equivalent nodal value at the  $i^{\text{th}}$  node,  $U_\infty$  is the uniform surface load (in the present case, being the uniform flow upstream),  $N_i$  is the shape function and  $\bar{\omega}_i = \iint N_i dx dy$  is the weight of the  $i^{\text{th}}$  node. Also,  $\bar{\omega}_i$  can be interpreted as the area of influence of the  $i^{\text{th}}$  node and has the following property:

$$\sum_{i=1}^n \bar{\omega}_i = A_s \quad (2.35)$$

where  $n$  is the total number of node points on the surface and  $A_s$  is the area of the surface. The evaluation of  $\bar{\omega}_i$  can be done in isoparametric space as

$$\bar{\omega}_i = \iint_S \bar{N}_i dx dy = \int_{-1}^{+1} \int_{-1}^{+1} \bar{N}_i(\xi, \eta) |\bar{J}| d\xi d\eta \quad (2.36)$$

where  $\bar{N}_i$ , the two-dimensional quadratic shape functions as used in the present study, are given as (cf., Equation 2.27 for the three-dimensional shape functions):

$$\left. \begin{aligned} &\text{for corner nodes: i.e., } \xi_i = \pm 1, \eta_i = \pm 1 : \\ &\quad \bar{N}_i = \frac{1}{4}(1 + \xi\xi_i)(1 + \eta\eta_i)(\xi\xi_i + \eta\eta_i - 1) \\ &\text{for mid-side nodes at } \xi_i = 0, \eta_i = \pm 1 : \\ &\quad \bar{N}_i = \frac{1}{2}(1 - \xi^2)(1 + \eta\eta_i) \\ &\text{for mid-side nodes at } \eta_i = 0, \xi_i = \pm 1 : \\ &\quad \bar{N}_i = \frac{1}{2}(1 + \xi\xi_i)(1 - \eta^2) \end{aligned} \right\} \quad (2.37)$$

and the Jacobian of the transform is given as:

$$|\bar{J}| = \begin{vmatrix} \frac{\partial x}{\partial \xi} & \frac{\partial y}{\partial \xi} \\ \frac{\partial x}{\partial \eta} & \frac{\partial y}{\partial \eta} \end{vmatrix} \quad (2.38)$$

The evaluation of the integral (Equation 2.36) for  $\bar{\omega}_1$  can be accomplished by means of a Gauss-Legendre quadrature formula similar to the one given by Equation 2.33.

#### 2.2.3.2 Boundary Conditions on the Free Surface

From Equations 2.5 and 2.6, it follows that two boundary conditions must be imposed on the free surface. If the potential at the equipotential plane of symmetry (Section AA, Figure 2.4) is set to zero, the potentials at the node points along any assumed streamline, which issues from the edge of the plate or foil, can be estimated according to the constant pressure condition (Equation 2.5) by integration back from Section AA, such that (referring to Figure 2.5),

$$\phi_{i+1}^j = \phi_i^j + \int_{S_i^j}^{S_{i+1}^j} (-q) dS \quad (2.39)$$

where the subscript  $i$  refers to values at node points along the same streamline and the superscript  $j$  refers to different streamlines on the free surface. The potentials at mid-nodes, such as  $S_i^{j+1/2}$ , are interpolated from the values at the adjacent corner nodes,  $S_i^j$  and  $S_i^{j+1}$ . To start the iterative procedure,  $q$  is estimated by use of the upstream uniform flux and a mass conservation balance, subsequently,  $q$  is adjusted to satisfy the separation tangency condition.\*

The second boundary condition, e.g., the tangency of the free surface to the velocity vector (Equation 2.6) is used during the iterative procedure to create new (better) free surfaces by integration downstream from the separation surface on the foil.

#### 2.2.3.3 Effect of Mi-side Node Locations at Separation

The singular properties of isoparametric elements have been observed and studied by several investigators (e.g., Henshell et al. 1975,

---

\*In-flow equals out flow almost exactly once the solution has been iterated a few times and a mass balance is no longer a meaningful test. See Sec. 5.



Barsoum, 1976) in the field of structural analysis. They have demonstrated the possibilities of producing strain singularities of order  $x^{-1/2}$  by placing the mid-side nodes of two-dimensional, quadratic, isoparametric elements at the quarter point along an element side from the corner where the singularity occurs. However, it can be shown that, as a consequence, the Jacobian of the isoparametric transformation is singular; therefore, it may generate undesirable behavior near the singularity. In fact, Hibbitt (1977) showed that in the case of the quadrilateral element used by Barsoum (1976), the strain energy of that element is unbounded even though good numerical results were reported by Barsoum (1976). A similar procedure is used in the present study to improve the behavior of the solution at separation; however, the Jacobian of the isoparametric transformation is kept nonsingular here.

Consider a surface of an element just off the edge of the foil as shown in Figure 2.6. It is desirable for the present physical realization to have (i) the edge  $\alpha$  asymptotically perpendicular to the foil at the separation point S, and (ii) the edge  $\beta$  asymptotically tangent to the foil at the separation (the Kutta condition). From the isoparametric mapping of the edge  $\alpha$ , it can be shown that

$$\left. \frac{dz}{dx} \right|_{13}^{\alpha} = \frac{z_1 - 4z_9 + 3z_{13}}{x_1 - 4x_9 + 3x_{13}} \quad (2.40)$$

To satisfy condition (i), one needs to have  $(dz/dx)|_{13} \equiv 0$  in Equation 2.40 which leads to

$$\begin{aligned} z_1 - 4z_9 + 3z_{13} &= 0 \\ \therefore z_9 &= z_{13} - \left( \frac{z_{13} - z_1}{4} \right) \end{aligned} \quad (2.41)$$

It is clear from Equation 2.41 that the edge  $\alpha$  has zero slope at the separation point S if the mid-side node #9 is placed at the quarter point location from corner node #13 in the z-coordinate. The x-coordinate of mid-side node #9 is still arbitrary. However, to avoid having a singular

Jacobian for the transformation, the x-coordinate of the node #9 should be kept away from the quarter point location. Condition (i) also ensures the continuity of the x-derivative (x-component of the velocity vector in the present study) of the field variable as one moves down the body and past the separation point S (across the element boundaries) and onto the free surface. This character is essential to an accurate satisfaction of the Kutta condition ( $u \equiv 0$ ) on the horizontal component of velocity at separation.

Similarly, from the mapping of edge  $\beta$ ,

$$\left. \frac{dz}{dx} \right|_{\beta} = \frac{-3z_{13} + 4z_{14} - z_{15}}{-3x_{13} + 4x_{14} - x_{15}} \quad (2.42)$$

condition (ii) requires Equation 2.42 to be infinite at the separation point S. This is achieved by setting the denominator of Equation 2.42 to zero; hence,

$$\begin{aligned} -3x_{13} + 4x_{14} - x_{15} &= 0 \\ \therefore x_{14} &= x_{13} - \left( \frac{x_{13} - x_{15}}{4} \right) \end{aligned} \quad (2.43)$$

Therefore, as far as the local shape of the free surface is concerned, the tangent separation condition is satisfied at every iteration if the mid-side node #14 is placed at a quarter point location in the x-coordinate. Similar to the case for condition (i), the z-coordinate of the mid-side node #14 can be arbitrary except that it cannot be at the quarter point location in z because then the Jacobian  $|J|$  of the transformation will become singular. However, it is shown later that the effect of satisfying the "local" separation condition in this manner is not significant. One can conclude that the local behavior of the free surface within the element at separation is not of paramount importance; however, the summed behavior (i.e., the average value of the velocity at a node) does seem to be crucial as shown below.

### 2.3 COMPUTATION OF AREAS AND FLOWS

In the course of the iterative procedure, it is necessary to compute areas of arbitrary plane shapes, flows through arbitrary plane cross-sections, and the sum of squares of the velocities over plane foils of arbitrary shape. The area of the foil and the sum of squares of the velocities over the foil are needed in the computations of the drag and the drag coefficient. The trial velocity on the free surface at Section AA (Figure 2.4) is initially estimated from the total flows through the upstream and downstream cross-sections. All these can be evaluated in a similar fashion in the isoparametric space.

For areas of cross-sections and foils, one can use Equations 2.35 and 2.36. However, the area of any surface of an element also can be obtained as

$$A_s = \iint_{S^e} dx dy = \int_{-1}^{+1} \int_{-1}^{+1} |\bar{J}| d\xi d\eta \quad (2.44)$$

where  $|\bar{J}|$  is the Jacobian of the transformation given by Equation 2.38. For a two-dimensional isoparametric element with  $n$  node points, the Jacobian  $|\bar{J}|$  of the transformation can be computed by

$$\begin{aligned} |\bar{J}| &= \bar{J}_{11}\bar{J}_{22} - \bar{J}_{12}\bar{J}_{21} \\ \text{where } \left. \begin{aligned} \bar{J}_{11} &= \sum_{i=1}^n x_i \frac{\partial \bar{N}_i}{\partial \xi} , \\ \bar{J}_{12} &= \sum_{i=1}^n y_i \frac{\partial \bar{N}_i}{\partial \xi} , \\ \bar{J}_{21} &= \sum_{i=1}^n x_i \frac{\partial \bar{N}_i}{\partial \eta} , \\ \bar{J}_{22} &= \sum_{i=1}^n y_i \frac{\partial \bar{N}_i}{\partial \eta} \end{aligned} \right\} \quad (2.45) \end{aligned}$$

and  $\bar{N}_i$  is the shape function of the transformation.

Similarly, for a flow  $Q$  through arbitrary cross-sections, one has

$$Q = \iint_{S^e} u \, dx dy = \int_{-1}^{+1} \int_{-1}^{+1} u |\bar{J}| \, d\xi d\eta \quad (2.46)$$

where  $u$  is the component of the velocity normal to the cross-section. Expressing the velocity in terms of its nodal values and the shape functions  $\bar{N}_i$  yields

$$u = \sum_{i=1}^n \bar{N}_i u_i \quad (2.47)$$

where  $u_i$  are the known values at the node points of the element. Then, Equation 2.46 becomes

$$Q = \int_{-1}^{+1} \int_{-1}^{+1} \left( \sum_{i=1}^n \bar{N}_i u_i \right) |\bar{J}| \, d\xi d\eta \quad (2.48)$$

Equation 2.48 can be generalized to compute the area times the sum of the squares of the velocity at any cross-section as

$$Q^2 = \int_{-1}^{+1} \int_{-1}^{+1} \left( \sum_{i=1}^n \bar{N}_i u_i \right)^2 |\bar{J}| \, d\xi d\eta \quad (2.49)$$

which is needed by Equation 2.10 for estimation of the drag and lift coefficients. Equations 2.44, 2.48, and 2.49 can be evaluated by means of a Gauss-Legendre quadrature formula in two-dimensions as described in Section 2.2.3.

## 2.4 CHARACTERISTICS OF THE FREE SURFACE

As mentioned in Section 2.1 an iterative procedure is needed for determining the location of, as well as the constant pressure condition on, the free surface. The constant pressure condition is satisfied on each streamline at each step (this is required by the use of Equation 2.39); however, the constant pressure condition does not need to be satisfied across the streamlines (i.e., the pressure on each streamline may be different from that on its neighbor) until the solution has converged. This characteristic is important because as described later, it suggests a stable iterative procedure.

The location of the free surface is assumed at the start of the iterative procedure. Thereafter, the new location of the free surface is approximated by moving the present free surface, based on the streamline conditions (Equation 2.6) along rays of constant  $j$  (Figure 2.5), such that the new free surface is tangential to the velocity vectors computed on the old free surface. Velocities on the free surface at any iteration are known functions of the spatial coordinates ( $x, y, z$  in Cartesian coordinate system) having been determined from differentiation of the velocity potential field which was determined for a given geometry prior to shifting of the free surface.

Generally, any given surface can be described by

$$F(x, y, z) = 0 \quad (2.50)$$

or specifically by

$$F = X(y, z) - x = 0 \quad (2.51)$$

From differentiating Equation 2.51, one obtains

$$dx = X_y dy + X_z dz \quad (2.52)$$

where the subscript denotes partial differentiation with respect to that variable. However, for the free surface which is tangent to the velocity field, one can write (cf., Equation 2.6)

$$\left. \begin{aligned} \frac{dx}{dt} &= u \\ \frac{dy}{dt} &= v \\ \frac{dz}{dt} &= w \end{aligned} \right\} \quad (2.53)$$

From Equations 2.52 and 2.53, one finds

$$vX_y + wX_z = u \quad (2.54)$$

as the equation of the free surface. It can be shown that (Street 1973, Chapter 9) Equation 2.54 is a first-order, quasi-linear partial differential equation which has characteristics given by

$$\frac{dx}{u} = \frac{dy}{v} = \frac{dz}{w} \quad (2.55)$$

and a unique solution determined by the passage of the characteristics through a single noncharacteristic curve on the surface. Equation 2.55 is exactly the same as the streamline conditions given by Equation 2.6. Therefore, the free surface is a characteristic surface. Furthermore, the non-characteristic curve is precisely the separation curve which represents the edge of the foil. Thus, the solution to the problem hinges, first, on an accurate integration of Equations 2.55 or 2.6 and, second, on an accurate representation of the velocity field, in particular, the conditions at the separation curve. As we demonstrate below, the first condition is easy to satisfy; the second is not. If errors creep in at separation the exact characteristic through each node on the separation curve uniquely represents different flow conditions. Accordingly, one can expect progressive divergence of the iterative solution (cf., Larock and Taylor, 1976, where drift of the solution is noted).

Only when the solution has converged, can one say that the computed characteristic surface must feel the same pressure everywhere (i.e., constant pressure and only then need  $q^j$  be the same for all  $j$  in

Figure 2.5). [Note that the magnitude  $q$  of the velocity is related to the pressure by Equation 2.3.] Accordingly, during the course of the iterative procedure, it is possible to adjust the  $q^j$  from streamline to streamline, such that the separation velocity at each node tends toward an average value typical for all nodes on the separation curve. This leads to the development of a weighting scheme described in Section 3 and tends to keep the shifting streamlines on the same characteristic surface.

### 3. ITERATIVE PROCEDURE

The problems which remain to be solved after the formulation in Section 2 are two. First, because the trial-free-boundary method is used, the problem for the velocity potential  $\phi$  is reduced to a well-posed linear problem. Under the finite element method used here, a linear system of algebraic equations is all that must be solved (See Appendix 2).

Second, however, the correct location for the cavity free surface must be obtained. This can be accomplished by an iteration procedure in which sequentially one prescribes a best estimate of the cavity surface and then finds the corresponding  $\phi$  values. From these, velocities are determined and they give the basis for prescribing a new free surface location.

#### 3.1 OVERVIEW OF THE ITERATIVE PROCEDURE

The iterative procedure is needed to determine the correct location of a cavity free surface which is tangent to the flow velocity and on which the constant pressure condition is accurately satisfied. The step by step iterative procedure is described in this sub-section. Detailed descriptions of specific schemes are given in the following two sub-sections.

The procedure consists of seven steps as follows:

##### Step 1: Geometry Setup

With given shapes and sizes of the plate and water tunnel and an assumed initial location of the free surface, the solution domain is well defined. It is then discretized into finite elements of variable sizes. Smaller elements are used in regions where high resolution is required, for example, near separation or zones of rapid changes in flow direction.

From a computational point of view, the actual discretization of the solution domain is done separately. (The mesh generation procedure is described in Appendix 1.) Then the coordinates of all corner nodes together with the corresponding nodal numbers become inputs to the actual flow-computation model. The mid-nodes of all elements are interpolated automatically by the computer program.



### Step 2: Boundary Conditions

An uniform horizontal velocity  $U_\infty$  is imposed upon the upstream cross-section of the water tunnel (cf., Section 2.2). The velocity potential  $\phi$  on the free surface is estimated from the assumed location as described in Section 2.2. At the solid boundaries and the planes of symmetry, the no flux condition is imposed. In the FEM, this natural boundary condition is assumed by the program when neither  $\phi$  nor a flux are prescribed.

### Step 3: Generation of Stiffness Matrices

With the established coordinates of the node points from Step 1, the elemental stiffness matrices,  $K_{ij}^e$  of Equation 2.23, are generated. Because of the great amount of data being generated, these elemental stiffness matrices are usually stored on magnetic disks or tapes.

### Step 4: Solution for the Velocity Potential $\phi_i$

The velocity potential is determined by solving Equation 2.25. However, the global stiffness matrix  $K_{ij}$  is not formed explicitly. Methods for solving this large sparse linear system are reviewed in Appendix 2.

### Step 5: Computation of Velocity Field

The fluid velocities are calculated by differentiating the velocity potential  $\phi_i$  as

$$\frac{\partial \phi_i^e}{\partial x_j} = \sum_{i=1}^n \frac{\partial N_i}{\partial x_j} \phi_i^e, \quad j = 1, 2, 3 \quad (3.1)$$

where the subscript  $i$  denotes values defined for the  $i^{\text{th}}$  node point,  $n$  is the total number of node points for each element and  $N_i$  are the shape functions. Equation 3.1 gives the fluid velocities in three directions at all node points of element  $e$ . For node points that are common to more than one element, the fluid velocities are taken to be the algebraic average of the contributions from all adjacent elements.

### Step 6: Relocation of Free Surface and Test of Convergence

This step is the substantial focus of this work and many details are given in subsequent sections. To avoid the evolution of a divergent solution, the free surface location is actually changed only when the

magnitude of the velocity component normal to the plate at separation is less than a prescribed value. (This leads to a system which always satisfies the Kutta or tangent flow separation condition.) If the separation velocities satisfy this condition as described in Section 3.3, the free surface is relocated such that the new free surface is tangent to the velocity field which existed at corresponding node points on the previous free surface. The details of the relocation procedure are considered in Section 4.1. Next, the criterion for convergence is checked (cf., Section 4.2). If it is satisfied, the iteration is terminated and the solution has been obtained. Otherwise, the mesh in the near vicinity of the free surface is adjusted and the elemental stiffness matrices for those elements which were moved are replaced. Since only those elements which are near the free surface are moved, a relatively small number of elemental stiffness matrices need to be replaced.

#### Step 7: Boundary Conditions for the Free Surface

From the new location of the free surface, the velocity potential  $\phi$  on the free surface can be estimated according to Equation 2.39. However, the separation edge represents a boundary singularity (Crank and Furzeland, 1978) at which two types of boundary conditions meet, namely, the no flux condition and the prescribed velocity potential  $\phi$ . The error in the solution  $\phi$  at this point was shown by Crank and Furzeland (1978) to be a function of nodal placement; a similar relation can be expected for the FEM, i.e., the error decreases as element size decreases (see Section 6).

A significant and supplementary effect may enter in the present case, however. In the true three-dimensional case the curvature of streamlines varies along the separation line and the streamwise rate of change of the potential  $\phi$  will, therefore, be different at different nodes along the separation line. Accordingly, we believe that the boundary-condition-discontinuity error is not constant along the separation surface. To compensate for this we have constructed a special scheme for adjusting the potential  $\phi$  on individual streamlines (also see Section 6).

After the first iteration when the potential  $\phi$  is calculated from the downstream end of the cavity, we alter the separation values of the potential and then prorate that value to other nodes along the surface such

that a constant velocity is obtained on each streamline. However, this produces a different constant velocity on each streamline. As the solution converges (in the sense that the cavity surface does not move significantly), one hopes that the final velocity differences are small. As is shown in Section 3.3, where the weighting scheme is described in detail, there is no guarantee that the hope will be realized.

The iteration Steps 4 through 7 are now repeated until convergence is obtained.

### 3.2 INTERPOLATION AND EXTRAPOLATION SCHEMES

During the course of the iterative procedure, the free surface location is adjusted by satisfying the tangency conditions on the free surface (Equation 2.6). It is necessary, subsequently, to regenerate the segment of the finite element mesh adjacent to the free surface. The mid-side nodes on the free surface are relocated in such a way that the free surface remains smooth. Those nodes lying along a streamline are naturally and smoothly relocated during relocation of a streamline by integration from the separation point. However, an interpolation scheme is needed to relocate nodes between streamlines. Because of the symmetry of the physical problem for the pure drag case, a two-dimensional interpolation scheme is sufficient. However, for the lifting flow case, a three-dimensional scheme is necessary.

#### 3.2.1 For the Pure Drag Case

Referring to Figure 2.4, one sees that, if the movements of the node points on the free surface are restricted such that the corner nodes always lie on planes of constant  $x$ , a two-dimensional interpolation can be used to locate the  $y$  and  $z$  coordinates of mid-side nodes at any cross section of constant  $x$  given that the location of the corner nodes is known. Because of the symmetry of the physical problem with respect to the  $y$  and  $z$  axes as shown in Figure 3.1, a periodic cubic spline interpolation expressed in terms of the circular coordinates  $\theta$  and  $r$  is chosen with the boundary condition  $r|_{\theta=0} = r|_{\theta=2\pi}$ . However, an algorithm for unequally spaced knots (nodes) is required. Since the theory of spline

interpolation is well documented, readers are referred, e.g., to de Boor (1978) for a detailed treatment on the subject. However, the algorithm used in the present study is taken from Spath (1973, Ch. 4).

### 3.2.2 For the Lifting Flow Case

In order that the effect of mid-side node locations at separation as described in Section 2.2.3.3 be the same in the lifting flow at all iterations as in the pure drag case, it is necessary to have the mid-side node #14 (Figure 2.6) at the  $1/4$  distance from the separation point  $S$  in a transformed  $x'$  direction which is perpendicular to the plate as shown in Figure 3.2. Consequently, it is desirable that the movements of all of the node points on the free surface be restricted such that the corner nodes always lie on planes of constant  $x'$  as illustrated in Figure 3.2. However, then the nodes at the "end" of the new (relocated) free surface may fall short of or over the centerline ( $C_L$ ) so that extrapolation or interpolation, respectively, is necessary to align the corner nodes with the centerline. Unlike the pure drag case, a general three dimensional algorithm for unevenly spaced data is needed here.

Interpolation with irregularly spaced data has long been a subject of interest for numerical analysts. Among the methods used, one can find methods based on local bivariate interpolations (e.g. Akima, 1978) as well as methods with multivariate smoothing splines (e.g. Fulker, 1975). These methods in general, are very expensive and relatively difficult to use. Following the concepts inherent in the isoparametric finite elements as used in the present study, a "local", general, three-dimensional interpolation and extrapolation scheme by means of isoparametric mapping has been developed. This new scheme is found to be applicable in two, as well as in three, dimensions.

The two-dimensional result is obtained first. Consider the isoparametric transformation given in Equation 2.26 and the shape functions given in Equation 2.27 (cf., Equation 2.37 for the two dimensional shape functions) and imagine that the  $z$  axis in the physical coordinates is identical with the  $\zeta$  axis in the local coordinates. Then, the transformation degenerates to a two-dimensional problem. Referring to Figure 3.3 and mapping the side

③-⑤-⑧ with  $\xi = 1$ , one has the following

$$\left. \begin{aligned} x &= x_5 + (x_8 - x_3) \frac{\eta}{2} + (x_3 + x_8 - 2x_5) \frac{\eta^2}{2}, \\ y &= y_5 + (y_8 - y_3) \frac{\eta}{2} + (y_3 + y_8 - 2y_5) \frac{\eta^2}{2}, \end{aligned} \right\} \quad (3.1)$$

$$-1 \leq \eta \leq 1$$

where  $x$  and  $y$  are the coordinates in physical space for any point along the side ③-⑤-⑧. Imagine the side ③-⑤-⑧ of the isoparametric finite element is arranged so as to coincide with the data points (i.e., the known node points) as indicated in Figure 3.3(c). Then, one can use Equation 3.1 to interpolate the value of  $y$  (at the point indicated by the cross, for example), say, for a known value of  $x$  between  $x_3$  and  $x_8$ , first, by solving for the value of  $\eta$  as

$$\alpha_1 \eta^2 + \alpha_2 \eta + \alpha_3 = 0 \quad (3.2)$$

where

$$\alpha_1 = (x_3 + x_8 - 2x_5)/2,$$

$$\alpha_2 = (x_8 - x_3)/2, \text{ and}$$

$$\alpha_3 = x_5 - x_1,$$

and second, by evaluating  $y$  from the second equation of Equations 3.1. For interpolation between ⑤-⑧ in Figure 3.3(c), one can do the interpolation from the left (using ③-⑤-⑧) as well as from the right (using ③-⑤-⑧) and a weighted mean value from the two interpolated values can be taken as the final solution. From numerical experiments, it is observed that this weighted interpolation scheme is approximately  $O(S^4)$ , i.e., fourth order accurate with respect to the side length. However, this scheme suffers the restriction that node #5 must lie in the middle half of the side ③-⑤-⑧ (or ③-⑤-⑧) for uniqueness in the solution to be guaranteed.

One can also extrapolate by means of the isoparametric mapping. Specifically, given the coordinates of (3)-(5) and the cross point in Figure 3.3(c), one can obtain  $y_8$  provided that  $x_8$  is known at the extreme point #8. As soon as the value of  $\eta$  is obtained from Equation 3.2,  $y_8$  can be found from the following:

$$y_8 = \frac{y + (\eta^2 - 1) y_5 + \frac{\eta}{2} (1 - \eta) y_3}{\frac{\eta}{2} (1 + \eta)} \quad (3.3)$$

where  $y$  and  $\eta$  are values for the intermediate point  $x$ .

Should the data points not lie on the same  $z$ -plane, one has to add the third equation 3.1 for  $z$ , namely,

$$\left. \begin{aligned} z &= z_5 + (z_8 - z_3) \frac{\eta}{2} + (z_3 + z_8 - 2z_5) \frac{\eta^2}{2}, \\ -1 &\leq \eta \leq 1 \end{aligned} \right\} \quad (3.4)$$

where  $z$  is the  $z$ -coordinate for the intermediate point at  $\eta$ . By means of this scheme, one can do interpolation or extrapolation in three dimensions with little computational effort and any one of the  $x$ ,  $y$  or  $z$  coordinates can be taken as the independent variable. However, this is only a local interpolation scheme such that any changes in data beyond the two points on either side of the interpolated value do not affect the final solution.

### 3.3 WEIGHTING SCHEME AT THE FREE SURFACE

As mentioned in Section 3.1, the separation edge represents a boundary singularity (Crank and Furzeland, 1978) at which two types of boundary conditions meet, namely, the no-flux condition on the solid plate and the prescribed velocity potential  $\phi$  from the free surface. Crank and Furzeland (1978) discuss the nature of this mixed boundary condition singularity. Such singularities are found in a wide variety of problems and various authors have used a variety of ways to combat the difficulties introduced by the

singularity. Of particular value are analytical forms which allow the singular nature of the problem to be analytically represented within the context of the numerical scheme. For two-dimensional problems with regular boundaries (boundaries which are not curved), significant success has been achieved with such analytical patches. On the other hand, the present cavity flow problem has both curved boundaries and irregularly-sized finite elements in three dimensions. It is not clear that an analytical patch of the nature required could be developed for three-dimensional physical space or perhaps in the isoparametric space. In any case, an alternative approach used by many authors is grid refinement near the singularity. In the end, because the error in the solution for velocity potential  $\phi$  at the singularity present here was shown by Crank and Furzeland (1978) to be a function of nodal distance, it was decided to use mesh refinement for the present solution. Although Crank and Furzeland (1978) demonstrated specifically the behavior in the neighborhood of a singularity for a finite difference solution similar behavior occurs for finite elements (e.g., see Strang and Fix, 1973, Sec. 8.4). It was expected, then, that by reduction of the finite element size in the neighborhood of the separation point the error which is manifested in the present problem by failure to satisfy the tangent-separation condition exactly could be systematically reduced.

The separation condition requires that the velocity normal to the surface of a body at separation be zero and that the flow be wholly tangential. With the present error due to the mixed boundary condition singularity, the normal velocity at different points along the separation edge is non-zero and variable. As shown in Section 2.4, the free surface is essentially a characteristic surface. From Section 2.2.3.3 it is known that the streamlines leave the separation surface tangential to the solid surface. If then the separation condition is not satisfied exactly, the governing first-order-partial-differential-equation for the free surface is not uniformly satisfied at the separation points. This occurs because, while the characteristic lines (or streamlines) are tangent to the body, they are not tangent to the velocity vector there, since the normal velocity at the separation point is non-zero. If the separation condition is not uniformly satisfied at each point along the separation edge, the streamlines from the separation edge each represent different physical flows. Accordingly, one might expect progressive divergence

of the iterative solution. Interestingly, Larock and Taylor (1976), who made no effort to impose a tangent-separation condition for their jet flow from an orifice, found that their solution tended to drift and that, under circumstances in which the flow was more highly three dimensional, convergence was either slowed or not obtained at all.

It became necessary, then, to devise a scheme whereby the velocity potential  $\phi_s$  at the separation edge could be adjusted to control satisfaction of the tangent-separation condition. This led to the development of the weighting scheme described below. From the computed velocities normal to the plate at various separation points, one can derive a set of weights, one for each separation point and streamline, which adjust the velocity potential at separation such that the normal velocity at each separation point is zero within a certain limit. The limit was usually set as follows:

$$\text{Max } \left| \begin{array}{l} \text{Velocity normal to the} \\ \text{plate at separation} \end{array} \right| < 10^{-2} \quad (3.5)$$

After the value of the separation velocity potential  $\phi_s$  is determined, values for the new velocity potential along the appropriate streamline are apportioned to the node points of the streamline such that  $\Delta\phi/\Delta s$  constant. Since  $\phi$  equals  $\phi_s$  at separation and  $\phi$  is zero at the center line of the cavity, the free surface velocity on a streamline becomes  $q_s$  which is equal to  $\phi_s$  divided by the length of the streamline in question. Then the new set of free-surface velocity potentials  $\phi_f$  are used as the Dirichlet boundary conditions on the free surface for the next iteration; however, since  $\phi_s$  is determined to make the normal velocities zero,  $q_s$  is not necessarily the same on each streamline. This is the genesis of the main difficulties encountered herein.

This weighting scheme produced an absolutely convergent iterative process. Other schemes which we employed gave unstable or divergent iterative processes except in those cases in which the flow was two-dimensional, i.e., axisymmetric or plane flows. The drifting of the streamlines reported by Larock and Taylor (1976) did not occur. Detailed results are discussed in Sections 4.2, 5 and 6; however, the general procedure in solving problems using the weighting scheme is as follows. To start, the upstream flow is



prescribed and held constant throughout the procedure. With the assumed location of the free surface, the free surface velocity can be estimated from a continuity argument applied to the upstream face of the computation region and the center line of the cavity. Weights are equal to unity in the first iteration; therefore, the velocity potential  $\phi_s$  on the free surface at separation equals the length of a streamline times the estimated constant velocity on the free surface. The problem for  $\phi_s$  is then solved, and the velocities at separation are computed. Based on the magnitude of the velocity normal to the plate, the weights are adjusted such that, when they are multiplied with the original velocity potential  $\phi_s$  at separation, the separation condition should be satisfied. For example, if there is a positive normal velocity in a pure drag flow, such as that depicted in Fig. 2.4, the velocity potential  $\phi_s$  will be increased to reduce this positive normal velocity. These new values of the velocity potential  $\phi_s$  at separation are then prorated to the nodes on each streamline proportional to the distance along the streamline as indicated above. The problem is now solved again. This procedure is repeated until the separation criterion is satisfied, and the free surface is then moved. With the new location of the free surface, the resulting new problem is solved again (as above) until convergence is obtained. Because continuity is satisfied after one or two iterations, the solution is considered to have converged when the stream surface stops moving. This is normally taken to occur when no change occur in the fourth significant figure for the physical location of any free service point on the cavity center line, i.e., at the downstream end of the computational area, over several iterations. During the iteration procedure, it was often found to be more economical to adjust the weights manually between each iteration. This enables the user to lead the iterative process to more rapid convergence and reduce the cost of the computation. In the cases studied here, the circular arc and elliptic pure drag cases were iterated with user intervention until the first move of the free surface. Automatic correction was used thereafter. Lifting flow cases were iterated manually. See Ko and Street (1979).

#### 4. IMPLEMENTATIONS AND TESTS

##### 4.1 SPECIFIC IMPLEMENTATIONS

In Section 2.2.3, the implementation of the boundary conditions was addressed. It was found that the condition that the free surface be tangent to the surface of the foil at the separation point is satisfied by the quarter point location of the first mid-node. This is true asymptotically for the particular set of shape functions chosen. However, another method was considered, namely, patching in an analytic solution for the free surface shape (at the separation point) similar to the one used by Mogel and Street (1974). In two-dimensional flow, the form of the free-surface near the separation point varies with the two-thirds power of the distance away from the point, i.e.,

$$y \propto x^{2/3} \quad (4.1)$$

with equality given by

$$y = Cx^{2/3} \quad (4.2)$$

where  $C$ , the constant of proportionality, is determined solely by the velocity-components at the free surface at a horizontal distance  $x$  from the separation point. Assuming that the flow near the separation point is essentially two-dimensional (locally), the relationship given in Equation 4.1 is used in the three-dimensional case with  $y$  being measured perpendicular to the edge of the foil and in a direction tangent to the foil. This analytic patching algorithm was implemented and tested with the pure drag flow cases. It was found, oftentimes, that analytic patching caused initially a very sharp curvature of the free surface such that a smooth continuation of the rest of the free surface was impossible. When convergence was obtained, the patch had no significant effect on the results compared to cases without the patch. Therefore, the patch technique was dropped from the program as an option for free surface moving routine.

During the iterative procedure, the free surface is relocated based on the tangency of the velocity vector to the free surface. This is achieved by satisfying Equation 2.6 in the form

$$\left. \begin{aligned} \frac{dy}{dx} &= \frac{v}{u} \\ \frac{dz}{dx} &= \frac{w}{u} \end{aligned} \right\} \quad (4.3)$$

Equations 4.3 can be solved by direct integration, with the intermediate values of  $u$ ,  $v$  and  $w$  being interpolated linearly between node points, which is consistent with the quadratic finite element approximation. A fourth-order Runge-Kutta procedure is used. However, at the first element next to the separation edge, the inverse of the Equation 4.3 has to be used to avoid infinite slope at the separation, namely,

$$\left. \begin{aligned} \frac{dx}{dy} &= \frac{u}{v} \\ \frac{dx}{dz} &= \frac{u}{w} \end{aligned} \right\} \quad (4.4)$$

By means of Equations 4.4, one can also specify the zero slope conditions, namely,

$$\frac{dx}{dy} = \frac{dx}{dz} = 0 \quad (4.5)$$

at the separation point. However, this did not seem to be crucial for the iterative procedure to converge.

#### 4.2 VERIFICATION OF ALGORITHMS

In order to test the performance of the selected algorithms the present procedure has been tested against the best data available. Although there is not exact solution for the present three-dimensional cases with which to compare, it is hoped that the individual tests performed give

insight into the overall performance of the procedure. Two types of tests were undertaken. First, two-dimensional flows were tested, viz., a plane cavity flow and an axisymmetric flow were solved by use of the three-dimensional program. Second, the free surface shift algorithm was tested alone for a fully three-dimensional flow.

#### 4.2.1 Two-Dimensional Geometries

Because the flow-field has some basic symmetry, no variations are to be expected with depth (that is across the flow) in the plane flow or in azimuth for the axisymmetric flow. Accordingly, the weighting scheme of Section 3.3 was not employed. The normal velocity at separation approaches zero then only as a consequence of the natural iteration process and is not controlled or otherwise constrained except by the adjustment of the free surface velocity to yield balanced inflow and outflow. The velocity potential on the free surface is prescribed then according to Equation 2.5 for every iteration.

One two-dimensional geometry was selected from among those reported in Mogel and Street (1974) as an example of the behavior of the three-dimensional program for a two-dimensional flow. As shown in Figure 4.1 a flow was constructed which has a typical cavity configuration in the plane of flow and is one element deep. If the program is operating correctly, there are no driving forces to cause the front and back faces of the element with respect to depth to have different values of the unknown potential or velocities. Accordingly, the correct program will lead to a convergent solution in which the values at the corresponding points of the front and back faces of any element are essentially equal and the flow remains two-dimensional. When tested the present procedure yielded a converged solution in 23 iterations. The criterion for convergence was defined as

$$\epsilon < 10^{-2} \quad (4.6)$$

with  $\epsilon$  being the maximum movement of any node-point on the free surface between two consecutive iterations. Figure 4.2 shows the sequence of the movement of the free surface in the present case. Interestingly the three-dimensional, finite element code is found to be no more expensive for this

case than the two-dimensional method used by Mogel and Street (1974) for a solution of similar accuracy. However, in their paper it was possible to prescribe exactly that the x-component of the fluid velocity vector at separation from the plate is identically equal to zero. In the present case the shape function used in the finite element method leads to an x-component of the velocity at separation of the order of  $10^{-2}$  times the maximum velocity on the free surface.

Working in stream function-potential space Brennen (1969) solved the axisymmetric cavity flow past a circular disk in a circular water tunnel. He used a Riabouchinsky image model and a finite difference numerical technique. His numerical results were verified by a series of experiments. It is, therefore, a good test of the present procedure to compare the finite element result with Brennen's results for a typical case. Actually, three cases with different geometric dimensions were chosen for the tests. Converged solutions for all three cases were achieved with no weighting (cf., Section 3.3).

The results of these tests are shown in Figure 4.3 together with the curves presented by Brennen (1969). It is clear that the finite element and Brennen techniques are in precise quantitative agreement. In addition this test shows that if, as a consequence of flow geometry the discretization through the finite element prescription occurs uniformly across the flow, then errors in flow separation velocity likewise occur uniformly and the weighting scheme described in Section 3.3 is not necessary in order for the iteration procedure to be stable; however, it leads to the same results as obtained here.

#### 4.2.2 Three-Dimensional Geometry

The analytic solution for a uniform flow past a three-dimensional Rankine Oval is well-known. In particular, for a particular prescription of the oval geometry, i.e., length and width, one knows the exact surface geometry of the oval and the entire velocity field surrounding it. It is possible then to use this information to test the present algorithm for moving the free surface without being involved with the discretization, truncation or computation errors inherent in solving for the potential and

velocity fields in a given case. We begin by generating a regular, three-dimensional, geometric mesh for a typical cavity flow past a disk in a water tunnel, for example, as shown by the solid lines in Figure 4.4. Then the three-dimensional Rankine Oval is placed in the cavity such that the edge of the disk coincides with the analytic boundary of the oval at some convenient point. At each iteration the velocity field is thus computed from the analytic solution for the Rankine Oval and the free surface is moved from its original position in accordance with the analytic velocities for the Oval and the free surface moving algorithm as shown in Figure 4.4. The moved free surface converges to the analytic shape of the Rankine Oval. The accuracy obtained with a reasonable number of iterations is of the order of four to six significant figures.

From the results of the above tests, it is clear that the finite element method is more efficient than the finite difference method used by Mogel and Street (1974). From the tests of the plane and axisymmetric two-dimensional flows it is clear that the iterative procedure is absolutely convergent in those cases in which the representation of the separation velocity at the start of the free surface is not influenced by true three-dimensional effects. Further, the Rankine Oval test shows that if the velocity field is accurately represented the iterative procedure for moving the free stream surface is rapidly and stably convergent to any desired level of accuracy. We will see, however, in Sections 5.1 and 5.2 that discretization errors and the variations introduced by truly three-dimensional flows (those about strongly elliptic plates and lifting flows) can cause either an unstable iteration or convergence to a solution in which the free stream surface pressure is not constant as one moves across or transverse to the streamlines of the flow.

## 5. CAVITY FLOW RESULTS

One of the objectives in developing the present model is to gain the ability to simulate nonlinear, fully cavitating flows about hydrofoils. As mentioned in Section 1, there is not a fully nonlinear, three-dimensional model that can be used for design purposes. Consequently, design is often based on water tunnel experimental data. However, the data collected from water tunnel experiments is strongly related to the physical configuration of the experimental setup. The present model makes it possible to examine the effects of different physical configurations. Thus, one has direct insight into the interpretation of experimental results.

In this section results are presented for three flow geometries. In Section 5.1 pure drag flows past circular and elliptic plates in rectangular water tunnels are described. A lifting flow consisting of a circular plate at an angle of attack of  $60^\circ$  in a rectangular water tunnel is given in Section 5.2

Before examination of these flows it is crucial to understand the accuracy of presented solutions, which will be discussed in detail in Section 6. Because of the separation edge singularity reviewed in Section 3.3, the ability of the numerical solution to maintain a constant pressure (or velocity) over the entire cavity decreases as the three dimensionality of the free surface increases. The pressure (velocity) is closely constant streamwise or along each streamline; however, as one moves across the flow transverse to the streamlines the pressure (velocity) changes. The causes and potential cures for this effective error in the solution are covered in Section 6.

The effective error is, thus, negligible for all of the circular plate pure drag cases in which the cavity cross section is close to being circular. These solutions are essentially exact. The total difference between free stream velocities in the elliptic plate cases is of the order of five percent (10 percent for the pressure coefficient). However, for the lifting flow, the total free stream velocity difference between the leading and trailing edge streamlines is about 10 percent (21 percent for the pressure) which is unacceptable.

## 5.1 RESULTS FOR THREE-DIMENSIONAL, PURE DRAG CASES

### 5.1.1 Circular Plates in Square Water Tunnels

A circular plate with a two unit radius is used with three different square water tunnels with widths of 10, 15 and 20 units. This configuration was chosen because it is the simplest variation from an axisymmetric flow with a circular plate in a circular water tunnel (as solved by Brennen, 1969; see Figure 4.3). The circular plate is placed at a distance of 10 units from the upstream boundary at which a uniform flow is assumed (i.e.,  $F = 10$ ; cf., Figure 2.4). Due to the symmetry of the setup as mentioned in Section 2.1, only a quarter of the flow field needs to be solved. For the water tunnels with widths of 10, 15 and 20 units, the half width of the square tunnel  $W$  takes on values of 5, 7.5 and 10 respectively. Two different half-lengths  $L$  for the cavity are used, namely, 5 and 10 units. The effect of changing the cavity length will be discussed later in this section. For the case with a water tunnel width of 10 units, the effect of grid refinement was also examined (See Section 6.2). The apparent effect on the results was small, but some conclusions are drawn later in Section 6.2.

The results can be viewed from several perspectives, namely, the cavity's gross shape, the wall effects, the "stability of pressure coefficient" observed by Wu, et al. (1971) and Mogel and Street (1974), and the accuracy of the solution. These are treated in turn in the following paragraphs.

Interestingly, in all cases examined here, the cavity remains relatively circular in spite of the influence of the square water tunnel (cf., Figures 5.1 and 5.2). (For reference the lines are circular arcs in these figures.) However, the wall effect is substantial.

Normally, one views results at constant cavitation number  $\sigma$  and with various tunnel width to plate radius ratios. Then, a decrease in tunnel size produces an increase in cavity length for a given  $\sigma$  as the flow is driven toward choked flow. However, it is more convenient with a physical-space numerical-scheme to hold cavity length  $2L$  constant and let cavitation number  $\sigma$  vary. With cavity length held constant, decreasing the tunnel size tends to increase  $\sigma$ . This results also in a decrease in the B/P ratio



(cf., Figure 2.4). The corresponding increase in the velocity on the free surface is observed in Table 5.1. Figure 5.3 shows two sets of curves for the square water tunnel with two different cavity lengths, namely,  $L = 5$  and 10 units with  $L/P = 2.5$  and 5.0, respectively. When  $W/P$  is small, a large  $\sigma$  is needed to maintain as a short cavity; then the actual cavity length becomes relatively unimportant and the cavitation numbers for the square tunnel should be close together (as shown in Figure 5.3) because the  $L/P$  ratios studied are different only by a ratio of two. This is also true for the ratio  $B/P$ .

From Figures 5.1 and 5.2, one might conclude that the corner of the square water tunnel had little effect on the cavity shape. However, the blockage effect is very different from a similar axisymmetric case. Figure 5.3 demonstrates these trends. For large  $W/P$ , the wall effects are insignificant and the blockage effect of a circular tunnel is no different than that of the square tunnel. Therefore, the cavitation number  $\sigma$  from the square tunnel coincides with the similar axisymmetric case for both values of  $L/P$  tested here. However, when the width of the square tunnel (the radius in the circular case) decreases, the axisymmetric flows feel the wall effect much faster than the similar square tunnel flows. For the axisymmetric flows, the cavitation numbers  $\sigma$  converge for the two  $L/P$  ratios when  $W/P$  decreases, as observed for the square tunnel flows.

Wu et al. (1971) and Mogel and Street (1974) observed that the coefficient  $C_D^* = C_D(1 + \sigma)^{-1}$  is nearly constant for many flow configurations in which  $W/P$  is varied. Table 5.1 shows that  $C_D^*$  is close to constant in this three dimensional flow as well. However, while  $C_D^*$  appears virtually independent of  $\sigma$ ,  $C_D^*$  does increase by about 5% when  $W/P$  is reduced by 50%.

Table 5.1 summarizes the results for a particular set of circular-plate-in-square-tunnel cases. For each case, convergence was certainly achieved in 25 iterations; actually no significant changes are observed after 15-20 iterations. Convergence means that the velocity components normal to the plate at separation were less than about  $10^{-2}$  times the free stream velocity and no changes were observed in the fourth significant figure of the cavity streamline end points over several iterations. Contrary to the experience of Larock and Taylor (1976), no accumulated drift in the streamlines is observed in the present study.

### 5.1.2 Elliptic Plates in Rectangular Water Tunnels

The elliptic plate used by Jiang and Leehey (1977) in their lifting flow study was chosen for this pure drag flow study. The basic configuration consisted of an elliptic plate with 2.35 unit by 7.75 unit semiaxes and a 40 unit by 20 unit rectangular water tunnel. With reference to Figure 2.4, the plate is placed at a distance of 20 units from the upstream boundary at which a uniform flow is assumed, e.g.,  $F = 20$  units. In order to examine the wall effect, a water tunnel with 80 unit by 40 unit was also used. Two different cavity half-lengths, namely, 10 units and 20 units, were used to examine the change of the cavitation number with respect to the tunnel geometry. The parameters of the studied geometry and the gross results are given in Table 5.2.

In spite of the influence of the rectangular water tunnel shape, the cavity remains essentially elliptic (Figure 5.4). Again, the wall effect is substantial. As indicated in Figure 5.4, as the ratio of the tunnel half width to the short semiaxis of the plate  $W/P$  decreases from 6.15 to 3.08, the cavity is pushed in toward the center line, and there is an increase in the velocity on the free surface, i.e.,  $\sigma$  increases (cases E1 and E3, Table 5.2). However, the wall effect on the cavity size due to the decrease in the ratio of  $D/Q$  from 5.16 to 2.58 is very small.

In the elliptic cases tested here, the coefficient  $C_D^*$  showed a slight dependence on tunnel size, but not on  $\sigma$ , the difference being approximately 5% between the two tunnel configurations. However, this difference may be due to the error in the constant pressure condition on free surface (see Section 6).

## 5.2 RESULTS FOR A THREE-DIMENSIONAL LIFTING FLOW

The final step of the present study was simulation of a lifting supercavitating flow in a water tunnel. The geometric configuration is essentially the same as the pure drag flow with a circular plate of 2 unit radius in a square water tunnel of 15 by 15 units (Section 5.1.1). The center of the plate is placed 10 units downstream from the upstream boundary where an uniform velocity  $U_\infty$  is prescribed. The plate is at an angle of attack  $\bar{\alpha}$

of  $60^\circ$ . The cavity half-length is 5 units from the center of the plate. Figure 5.5 shows the FE mesh in three dimensions. Figure 5.6 shows the final centerline cavity shape after 5 shifts of the free surface. The cross-section of the cavity is found to be only a slight variation from circular (cf., the dashed line in Fig. 5.6). The stagnation point (where the pressure attained its maximum) is approximately 1/8th of the diameter of the plate from the leading edge. Figure 5.7 shows the pressure distribution along the centerline of the plate. Both because the separation edge represents a boundary singularity and because the normal method of computing the flow velocity breaks down at the separation edge (see Section 6), the pressure coefficient on the plate does not drop off to zero at separation as it should. The effect of the velocity calculation is not large and can be corrected for if the boundary singularity effects were minimized.

Figure 5.8 shows a contour plot of the pressure distribution on the plate for the lifting flow. Because in the plot straight lines are used to join the node points the circular edge of the plate appears to have corners. The intermediate values of the contours are interpolated from those at the nearby node points. This when coupled with the behavior of the element interpolation functions and the contour routine interpolation functions introduce slight wavy variations on the contours. These variations would be eliminated if more node points were used on the plate. The cavitation number  $\sigma$  for this lifting flow is 0.53. The corresponding drag and lift coefficients  $C_D^*$  and  $C_L^*$  are 0.63 and 0.37 respectively.

The lifting flow tested here converged to the final solution after 5 free surface relocations. However, it took approximately 30 iterations to achieve this result. It was clear that it is more economical to manually adjust the "weights" (cf. Section 3.3) between iterations. By this, human experience can be employed with judgment to make the rate of convergence faster. The test problem has 303 elements with 3137 node points. Each iteration, including setting up the elemental stiffness matrices for all elements, took approximately 5-1/2 minutes CPU time on the IBM 370/168 computer. The core requirement was 1152 K with approximately 1500 tracks of disk space on IBM 3300 disks for temporary storage.

## 6. PERFORMANCE OF THE SOLUTION AND ALTERNATIVE FORMULATIONS

The computation procedure outlined in Sections 2 and 3 is a relatively straightforward one. The program structure and basic finite element computational algorithms were adapted from an existing three-dimensional groundwater flow code for free surface flows developed by Dr. C. Taylor at the University of Wales, Swansea. The crucial choices and developments focused on the iterative method used herein and the means of prescribing and dealing with the high speed free surface, which has a different boundary condition than that found in groundwater flow.

Tests to verify the performance of the computational algorithms and to demonstrate that the computational method reproduced, exactly, existing axisymmetric flow calculations were presented in Section 4.2. The capacity of the method to solve fully three-dimensional cavity flows was demonstrated in Sections 5.1 and 5.2.

It is now appropriate to examine the nature of the iterative process that was used in this work, to discuss in detail the accuracy of the three-dimensional solutions presented in Section 5, and to explore alternative formulations which might remove some of the difficulties encountered with the present techniques. These three areas are explored in Sections 6.1 through 6.3.

### 6.1 THE NATURE OF THE ITERATIVE PROCESS

In order to separate the nonlinear cavity problem into linear pieces it is necessary, first, to establish a trial location of the cavity free surface, and second, to prescribe on that surface the velocity potential  $\phi$ . When the solution is complete, a correct and exact solution must have a constant velocity along each streamline of the free surface, and the velocity on each streamline must be the same as the velocity on adjacent streamlines. That is, there will be a single constant velocity over the entire free surface. In addition, the actual free surface must be tangent to the solid plate at the separation edge. While this can be mechanically guaranteed, i.e., the finite element method forces the physical surface to be tangent at the body at separation (see Section 2.2.3.3) it is difficult with the present

method to obtain the condition on the velocity that it be tangent to the solid body at separation. Both conditions must be met on an actual free surface. Accordingly, in formulating the problem one is faced with two requirements: first, create a solution in which the velocity is constant over the entire cavity; second, create a solution in which the velocity is tangent, not only to the free surface of the cavity, but also to the solid body at separation.

While it is obvious that the velocity along a given streamline should be constant and, hence, that the potential along the streamline should be specified so that the derivative of the potential with regard to distance along the streamline is a constant, it is not clear that one can simultaneously require the velocity on each streamline to be equal to the same constant value. Thus, in this work two alternative procedures for specifying the velocity potential were examined. Only one has been described previously because the alternative procedure, namely, that used by Mogel and Street (1974) and (in a three-dimensional flow similar to the present one) by Larock and Taylor (1976), led to unstable solutions for the present cavity flow problems. This unstable method consisted of adjusting the potential on the free surface such that the velocity was constant everywhere on the free surface. The velocity was adjusted so as to promote conservation of mass between the upstream and downstream cross-sections of the cavity flow. No attempt was made to control the tangent separation condition or to force the velocity normal to the plate at separation to be zero. The alternative iteration procedure, which was the one adopted here, is described in detail in Section 3.3. There, while the velocity was kept constant on each individual streamline, it was allowed to vary from streamline to streamline because the requirement was imposed on the calculation that the tangent separation condition be satisfied. This led to an exceedingly stable iteration. However, in cases of highly three-dimensional flow, that is, when the cavity shape was three-dimensional, the converged solution had different velocities on adjacent streamlines. The size of this error is discussed in the next section.

The question arises: Why is the ostensibly more logical iterative procedure unstable? An examination of the detailed print-out for a typical

convergent simulation by Larock and Taylor (1976) [kindly provided by Professor Larock] shows that their solution does not satisfy the tangent separation condition; the velocity normal to the orifice of their jet flow is of the order of 0.2 to 0.5 times the actual velocity at separation, and the velocity normal to the plate is different at the top and bottom of their orifice. For slightly three-dimensional flows such as theirs (and indeed our circular-plate pure-drag cases) this appears to be of no consequence; however, we conjecture that failure to satisfy the tangent separation condition uniformly may be a root cause of the failure of the lower Froude-number cases of Larock and Taylor (1976) to converge. These flows are more highly three-dimensional and would appear to suffer from the same errors encountered in the present work. In the iteration used in the present work the tangent separation condition is satisfied essentially exactly in the iteration process and the velocity normal to a solid boundary is always at least two orders of magnitude smaller than the average velocity at separation.

Larock and Taylor (1976) noted that, if they continued to iterate their solution and shift their free surface as indicated by their iterative procedure, a number of small shifts tended to accumulate to a non-negligible effect. Thus, their solution tended to drift. If one uses the iterative procedure developed here and applies it to a flow from an orifice without the effect of gravity (a problem somewhat similar to that considered by Larock and Taylor at high Froude numbers), no drift of the solution occurs. Indeed, for the pure drag slightly three-dimensional cases examined here the iterative procedure described in Section 3.3 works exceedingly well and gives solutions that are quantitatively accurate. The present method, then, may be considered perfectly adequate for slightly three-dimensional flows. However, the problem remains, namely, what is the appropriate formulation for more highly three-dimensional flows in which the competing free surface and separation boundary conditions really must be satisfied simultaneously? The simple iterative procedure in which the separation boundary condition is not considered failed in the present case because, whenever the free streamline was shifted, its length changed and a new velocity was predicted in order to satisfy continuity. The resulting potential on the new free surface tended to vary irrationally at the separation point leading to great

difficulty in generating a reasonable flow field as a basis for the next trial-free boundary. However, the iteration procedure which guarantees satisfaction of the tangent separation condition does not guarantee that the velocity on all streamlines will be the same because, as the length of the streamline changes, the average velocity on the streamline also changes, and that change is different for each and every streamline. If the flow is close to axisymmetric, that is, if the cavity shape remains essentially circular, then all of the streamlines tend to change length in about the same amount and the separation tangency condition imposes approximately the same constraints. Accordingly, the solution converges very nicely in that the velocity is essentially constant over the entire free surface (as was found with the circular-plane and some of the elliptic-plate pure-drag cases). In the next section the detailed results of these calculations are examined and hypotheses are developed to explain the behavior and potential solutions for the problem. Finally, in Section 6.3 examination is made of alternative formulations which might also solve the difficulty encountered here.

## 6.2 ACCURACY OF THE SOLUTIONS

### 6.2.1 Review of Tests and Relevant Results

As indicated in the introduction to Section 5, the separation edge singularity apparently plays a crucial role in the accuracy of the solutions for various three-dimensional fully cavitating flows. To test the effect of grid refinement near the separation edge four additional cases were examined for the circular plate pure drag flows (cases 7-10 in Table 5.1). The grid refinement was achieved by twice halving the elements adjacent to the separation edge. In the unrefined cases (4 and 5 in Table 5.1) the first corner node from separation and on the free streamline was 0.15 units downstream of the circular plate ( $\Delta x_1 = 0.15$ ). First-level refinement (see Figure 6.1) used  $\Delta x_1 = 0.05$ ; second-level refinement used  $\Delta x_1 = 0.02$ . Both long ( $L = 10$ ) and short ( $L = 5$ ) cavities were studied. Gross changes in  $\sigma$ ,  $B/P$ ,  $C_D^*$  and cavity cross-section were less than one percent as a result of refinement. However, significant changes were observed in the

velocity at separation and the consequent variation in the velocity along a given streamline.

Before examining these results a brief note is needed. Larock and Taylor (1976) point out that with the finite elements used in their paper (and herein) uniqueness of flow velocities is obtained by averaging all the velocity values contributed by elements which contain a given node. As an exception, nodes at the junction of a solid and free surface can be considered to have in common only the solid boundary and those contributed by elements which have in common the free surface boundary. Larock and Taylor say their experience suggests that one should average only the velocities from elements having a free surface face. Because of the placement of mid-side nodes near separation at the quarterpoint of an element's side (see Section 2.2.3.3 or Figure (2.6), the x- or normal-components of the velocity contributed by the elements with solid faces and contributed by elements with free surface faces are exactly equal. However, the y- and z- (or tangential-) components are influenced by whether or not the element has a free surface or solid boundary. The present tests are in complete agreement with the Larock and Taylor conjecture. To illustrate these points the following notation is used in subsequent discussions: the velocity at separation contributed by elements which have a free surface face is denoted by  $V_F$ ; the velocity contributed by elements with a solid face is denoted by  $V_S$ ; and the average velocity contributed by all elements at a node is denoted as the computed velocity  $V_C$ . The velocity denoted by  $V$  is the free-stream average velocity computed by summing the velocities obtained at the cavity centerline on each streamline and dividing by the number of streamlines (by the number of corner nodes in the  $\gamma$ -direction; see App. 1).

Figure 6.2 shows the effect of grid refinement near separation for the circular-plate pure-drag cases. Clearly, the accuracy of the  $V_F$  representation increases dramatically as the element is refined. However,  $V_C$ , the usual average velocity at a node, remains a constant fraction of  $V_F$ . Therefore, the pressure calculation at separation will remain in error if  $V_C$  is used to calculate the pressure there. However, with refined elements near separation both on the solid plate and on the free surface, the error in the pressure or drag calculations is negligible. If the finite element



solution were exact at the separation point, then  $V_S$  would equal  $V_F$  and both would equal  $V_C$ . That is clearly not the case. Some insight can be drawn from Figure 6.3 for relatively long ( $L/P = 5$ ) and short ( $L/P = 2.5$ ) cavities in these circular-plate pure-drag cases. It appears that as  $W/P$  increases,  $B/P$ , i.e., the width of the cavity, increases as well. Hence, the curvature of a streamline near separation apparently decreases. One can infer that the "stress at separation" should decrease as  $W/P$  increases. This behavior is clearly shown in Figure 6.3 where both  $V_S$  and  $V_C$  increase relative to  $V_F$  as  $W/P$  increases. Therefore, all other things being equal, the separation behavior of the finite element method becomes less critical as the wall effects decrease.

Figures 6.4 and 6.5 illustrate that the present technique is a very accurate solution along each individual streamline and, further, that grid refinement makes a significant improvement in the solution behavior. Figure 6.4 shows the variation of the free stream velocity denoted by  $V_{FS}$  with distance along the streamline. This variation is presented as a percentage according to the formula  $\Delta V/V(\%) = [(V_{FS} - V)/V] \times 100$ . The importance of using  $V_F$  at separation point is also indicated. For example, if the averaged velocity at the separation point is used in an unrefined calculation, the apparent velocity error at separation is almost 22%. However, if  $V_F$  is used, the error is only 8%. Similarly the maximum error away from separation for the refined circular plate case is less than 1%. For the unrefined case, the value reaches 2-1/2%. However, for most of the streamline the unrefined and refined errors are essentially indistinguishable. A similar plot has been made for the elliptic plate case E2 and is given in Figure 6.5. This figure has been plotted on a semi-log scale to expand the region near the separation point. The horizontal axis is the distance downstream from the separation point plus 0.01 non-dimensional units so that it will plot on a log scale. It is important to notice here that although no specific grid refinement was undertaken for the elliptic case, the velocity error is less than 2% over 99% of the streamline. It is clear then that the particular method used here is a highly accurate solution along each streamline.

One additional experiment was also performed with the circular-plate pure-drag case. To test the effect of increasing the number of elements in

the transverse direction in the plane of section A-A (Figure 2.4), the number of elements in the transverse or  $\gamma$ -direction (see Appendix 1) was doubled for one pure-drag circular-plate case. In most cases, four transverse elements were used in the quarter flow for this kind of computation. The test case employed 8 elements. No gross parameter or shape changes occurred; however, the accuracy with which the no flux boundary conditions were satisfied on the  $y = 0$  and  $z = 10$  planes of the flow was increased by one order of magnitude. This result, together with the refinement tests, indicates that substantial improvement of flow detail can be achieved by adding elements, but little gross behavior change appears to occur, at least in these pure-drag, slightly three-dimensional cases. The information gained by this test of increasing number of elements in the transverse direction was put to use in the computation for the elliptic plate pure drag cases. In case E1 of Table 5.2, eight elements were used in the transverse or  $\gamma$ -direction. However, the elements nodal points were more or less uniformly distributed in the transverse direction as can be seen from Figure 5.4. This produced, in general a maximum velocity normal to the vertical boundary on the left of Figure 5.4 which was one-half of the vertical velocity through the upper boundary of Figure 5.4. In addition, the computation converged rather raggedly. In both cases, E2 and E3, a new geometry was used for the elliptic cases. The element nodal points were distributed such that in each element the included angle between lines drawn from the element corner nodes to the center of curvature of the free surface of that element was constant for all elements. As can be seen from Figure 5.4, this tends to bunch the elements near the sharp end of the ellipse and leave rather large spaces on the flatter, lower end of the ellipse. Interestingly, the rearrangement of the geometry inverted the relationships between the velocities through the vertical and horizontal faces of the flow, the maximum velocity through the vertical face now being twice the maximum velocity through the horizontal face. This is a strong indication that grid refinement in the streamwise direction and transverse grid refinement and geometry are important in fully three-dimensional calculations.

As indicated in Section 3.3, the present iteration procedure cannot guarantee that the pressure will be the same on all streamlines. However, the procedure does guarantee that the tangent separation condition is

satisfied to a high degree of accuracy. Figure 6.6 is the variation of free stream velocity  $V_{FS}$  across the end of the cavity for a typical circular plate and the three elliptical plate pure drag cases. A plot is made here in terms of node points in the transverse direction. Thus, the actual location of the individual streamlines must be deduced by referring to the diagrams for the various flows. In any case, the plot moves from left to right in the same manner as the diagrams for the various flows. For the circular-plate cases, case No. 5 which is plotted here contains the maximum error of any. That error does not exceed 0.7 percent. Thus, in view of the previous results, the circular plate cases can be considered to be exact numerical solutions of the three-dimensional fully cavitating flow. The error in the transverse direction for the free stream velocity was not significantly influenced by the streamwise grid refinement that was used in some of the circular-plate cases.

The elliptic plate pure drag cases are much more instructive in regards to the behavior of the solution because the streamlines at the pointed end of the ellipse tend to be much more highly curved than those at the flat or middle edge of the ellipse. The response of the computation to this "stress at separation" condition is that the free surface velocity is much lower at the highly curved edge where the computation is unable to maintain the tangent separation condition at a higher velocity. Interestingly, case E1 which uses the old or uniformly distributed geometry for the elliptic flow, behaves relatively more uniformly than cases E2 and E3 where the method tends to break down on the smooth edge of the flow where there is very little transverse resolution. This is consistent with our earlier observations about the flow velocity through the horizontal and vertical no-flux boundaries of the flow in the elliptic case.

The error between the maximum and minimum free stream velocities on individual streamlines is now more significant in the elliptic plate cases ranging up to a maximum value of about 7% for case E2. This corresponds approximately to a 14% error in the constant pressure condition if one makes the computation through the Bernoulli equation 2.3.

The lifting flow with a circular plate set at an angle of attack of  $60^\circ$  in a rectangular water tunnel has more extreme conditions as far as the curvature of the free streamlines than either of the pure drag cases studied.

From Figure 5.6 it can be seen that the upper or leading edge streamline has an extremely small radius of curvature near separation, while the lower or trailing edge streamline has a very gentle curve. Thus, the free stream velocity computed by the present technique is much higher along the streamline from the trailing edge where the velocity gradient and rate of curvature is smaller so that the tangent separation condition can be more easily satisfied. If streamwise grid refinement were the essential cure for the present difficulties, then making the elements near the leading edge separation should decrease the relative error between the two zones. Thus, one would expect to more equally satisfy the tangent separation condition and achieve more nearly the same velocity on each streamline. To pursue this idea, the first column of elements of separation edge were made smaller at the leading edge and gradually increased as one moved around the flow toward the trailing edge as shown in Figure 6.7. Though this refinement improved the convergence characteristics of the solution and produced more rapidly a more stable solution, no substantial improvement was observed in the error which was approximately 10% in the free stream velocity on the lower versus the upper streamline. In view of the results obtained for the circular plate and elliptic plate pure drag cases and the result obtained here, it would appear that grid refinement should be made in the transverse direction and that this would lead along with grid refinement in the streamwise direction to a better ability for the computational technique to meet both tangent separation and constant velocity (or constant pressure) conditions on the free surface. No attempt was made to use transverse grid refinement in the present case because of the cost of the computation.

It is worth noting in passing that during the course of the iteration for the lifting flow, the flow rate from the downstream end of the cavity generally converges to its final value which is very close to the inflow value upstream after two or three moves of the free surface. The flow rate again appears not to be a good criterion for measuring convergence because the stream surface continues to move significantly until the fifth or sixth move. Good values for the lift and drag coefficient are also obtained after just three moves indicating that for gross values and general results is not necessary to iterate to a final solution.

One final test was made with a lifting flow. The tangent separation condition was required to be satisfied only at the leading edge of the circular plate. The separation velocity potential was then adjusted at all other streamline in an attempt to create a free surface with a single constant velocity. The solution was carried through six free surface shifts. The results were not satisfactory because the separation velocity at the trailing edge exceeded the free stream velocity and the cavity surface showed the signs of drifting experienced by Larock and Taylor (1976).

#### 6.2.2 Potential Means to Reduce Solution Errors

The above review makes it clear that the present technique is satisfactory only in cases in which the curvature of individual streamlines as they separate from the solid body is essentially the same over the entire separation edge. In conditions when this is not true (for example, in the lifting flow studied here), the mixed boundary-condition singularity at the separation point causes the solution to be inaccurate and to make it difficult to satisfy both the constant pressure (or constant velocity) condition on the free surface and the tangent separation condition. Also, mesh refinement both in the streamwise and transverse directions tends to reduce the computational error. There appear to be three specific things that could be done to tackle this problem.

The first and most direct is simply to increase the number of elements used in the computation. At the present time the lifting flow utilizes 303 elements with 3,137 node points. Each iteration takes 5-1/2 minutes of CPU time on an IBM 370/168 computer. Since approximately thirty iterations are necessary to achieve convergence in the present computation, CPU time alone runs in excess of two hours per computation. On the other hand, Larock and Taylor (1976) were unable to examine the convergence behavior with a finer mesh because they pointed out the refinement must proceed concurrently in all three directions or else some elements could become highly distorted. In fact, in the present case the elements are already highly distorted. In particular, because of the relative small number of elements in the transverse direction, the elements near separation could be viewed as long curved pencils. It is not illogical to conclude that this may be significant cause of the difficulties in the present case. Thus, a refined mesh seems

like an important next step in any computations for lifting flows with the present method.

In order to accomplish the generation of a refined mesh one must examine the present procedure and see if a better mesh generator can be found. In the present mesh generation procedure for the lifting flow, the plate is first established in the rectangular tunnel as a pure drag flow and a mesh is generated. The plate is then tilted to the desired angle of attack and the elements near separation are carried with it. The elements at separation, particularly around the leading edge, can be very distorted in the streamwise as well as the normal direction, although they are not distorted in the transverse or  $y$  direction particularly. This distortion may lead to difficulties in the algebraic equation set which is generated to solve the potential flow problem or may produce close to singular Jacobians for the isoparametric transformations.

For further studies and as a second step, it would be appropriate to implement a mesh generation scheme based, for example, on the ideas of Thompson, et al. (1974). They demonstrated a method for automatic numerical generation of a general curvilinear coordinate system with coordinate lines coincident with all boundaries of a general multiconnected region containing any number of arbitrarily shaped bodies. They stated that no restrictions are placed on the shape of the boundaries and the method is not restricted to two dimensions. However, it is not known if the method has actually been implemented for a three dimensional flow. While the generation of a numerical mesh would in itself be expensive, the smooth shape and regular coordinate system produced by such an automatic generation scheme for curvilinear coordinates would allow the user to obtain a very accurate and well formed finite element net by using various points on the curvilinear coordinates, translating them back to Cartesian coordinates and establishing those as the corner and mid nodes of the finite elements. With such a system and consistent with the available computation funding and raw power, one could accomplish the generation of an adequate, refined and well-formed finite element mesh. Under these conditions it would be appropriate to use the variant on the present iterative technique which is applied in the final example for the lifting flow. Namely, control the tangent separation condition at a single point on the separation edge and

otherwise adjust the separation velocity potential to produce a single constant velocity on all streamlines.

A third and final alternative would be to follow on the discussion in Section 3.3 and to attempt to develop a formal analytic solution for the velocity potential in the zone near the separation edge. This would have to be an analytic three-dimensional solution in either physical or isoparametric space. If it could be found, it could be used to remove singular behavior from the finite element portion of the problem and thereby allow the finite element solution to accurately reproduce the regular part of the flow. The development of such an analytical patch appears to be a formidable task and has not been attempted in the present investigation (see, however, Strang and Fix, 1973, for an outline of the general approach for two-dimensions).

### 6.3 ALTERNATIVE FORMULATIONS

The method outlined in this work employs three-dimensional, 20 node quadratic finite elements and a trial-free-boundary technique to solve high speed free surface flows. As noted in Section 4.2.1, the present finite element formulation when applied to a two-dimensional plane flow is considerably more efficient than the finite difference calculations procedure outlined by Mogel and Street (1974). In addition, the finite element formulation meets the crucial requirement of being able to adjust the node points of the element grid to coincide with the curved and irregular boundaries of the free surface. It has been made clear above, however, that considerable grid refinement will be needed to make the present method an efficient and satisfactory one for highly three-dimensional flows. The question arises then as to whether or not there is a better alternative formulation which would lead to a successful solution of nonlinear fully-cavitating flows. Two alternative formulations come easily to mind and are discussed below. The first is the use of  $C^1$  continuous finite elements with the hope that these elements would provide higher accuracy at the separation edge. The second method is the boundary integral equation method in which it is necessary to solve for nodal unknowns only on the surface and not in the interior of the flow.

### 6.3.1 Other Finite Elements

The elements used in the present computations are  $C^0$  elements, that is, they insure the continuity of the solution function  $\phi$  across boundaries of elements. However, the first derivatives are not necessarily continuous. The present elements utilize quadratic interpolation functions. One can define  $C^0$  finite elements with cubic interpolation functions. However, there is no inherent gain by using cubic interpolation functions over simply reducing the size of the quadratic interpolation function elements. Accordingly, it does not seem profitable to define and use new  $C^0$  elements.

On the other hand, one is tempted to define  $C^1$  cubic elements using Hermite polynomials as described, for example, in Pinder and Gray (1977). Hermite polynomials with an isoparametric approach have been applied in two-dimensions. However, the process is inherently much more difficult than that used here and it is not clear that the cost of using the Hermite elements will not be considerably greater than using the present  $C^0$  quadratic elements. The major advantage of the Hermitian elements is that the unknowns now involved include the unknown velocity potential  $\phi$  and its first derivatives (i.e., the flow velocities) at the corner node-points of the element. This means, for example, that it would be possible to specify both the velocity potential and the normal derivative of the velocity potential at the separation point so as to satisfy both the constant pressure boundary condition and the tangent separation condition simultaneously. Thus, Hermitian elements would appear to be attractive. However, Strang and Fix (1973) have conducted a numerical experiment on the behavior of various elements in the neighborhood of a mixed boundary condition singularity of the type encountered at separation in a free surface flow. Their test indicate that the best accuracy can be obtained by using analytic patches in the neighborhood of the singularity to remove the singularity so that the finite element does not have to cope with it. On the other hand, a startling result is that the standard Hermite cubics come out worse than the simplest of linear elements with regard to error in the neighborhood of the singularity. Strang and Fix point out that the cubics are too smooth to cope with the singularity. It would appear then that the Hermitian elements do not offer, at least at this time, an attractive alternative to the solution method used so far.



### 6.3.2 The Boundary Integral Equation Method (BIEM)

Brebbia and Wrobel (1979) and Larock (1977) have discussed the application of the boundary integral equation method to fluid flows. In the BIEM, all computations deal directly with the domain boundaries, in this case the tunnel walls, solid bodies and cavity surfaces, rather than requiring a solution throughout the entire flow domain. If the BIEM is combined with surface finite elements then one can utilize finite elements in much the same way as they are used in the normal finite element method. That is, the body, cavity, and tunnel wall surfaces are represented by a set of finite elements, e.g., quadratic isoparametric elements, and formulation of the problem produces a series of nodal unknowns on these surfaces only which may be solved in the standard manner. One obvious advantage of the BIEM with finite elements is a potential substantial reduction in the number of nodal unknowns.

Larock (1977) focused his attention on jet and cavity flows and outlined the procedure that could be used for a simple two-dimensional jet flow. The procedure does not differ in the large from the one used here, in that a trial-free-boundary technique is used, a potential flow problem is solved and the resulting velocity field is used to move the free surface to a new trial location. The only difference lies in the method used solved for the velocity potential and velocity used. BIEM does offer potential savings in computer time. However, the problems which cause difficulties in the present computation apparently still exist in the boundary integral equation method.

Larock (1977) indicates that his formulation of the BIEM allows the tangent separation boundary condition to be violated and it was only by adjusting the velocity on the free streamline that he was able to drive the normal velocity at separation to zero. This, unfortunately, is precisely the same process that has been used in the present computation. Therefore, it would appear that at the present stage the boundary integral equation technique has the same failing as the finite element technique which is implemented above. Accordingly, it is probable the BIEM can be used only when the flow field is essentially axisymmetric as in the present finite element case or when sufficient grid refinement is made in the neighborhood of separation. Thus, while the boundary integral equation technique should

probably be further investigated for three-dimensional fully cavitating flow, one must not expect it at the moment to yeild more than a slightly more efficient computational technique and the difficulties encountered in the present investigation will not be instantly overcome by shifting to this new technique.

## 7. SUMMARY AND FUTURE WORK

Based on potential flow theory, a finite element model was developed for simulation of three-dimensional, fully-cavitating flows. A Riabouchinsky image model of the flow was used. The trial-free-boundary approach was used and effectively reduced the nonlinear potential flow problem to a linear one. However, because the free surface shape, as well as the velocity potential, is unknown, iterative solution of the linear problem is required.

Larock and Taylor (1976) solved a three-dimensional jet flow under the influence of gravity by use of a method and computer program similar to those employed herein. However, the present study is the first to deal with a cavity flow and the first to conduct a detailed examination of the ability of the finite element method to accurately represent separated flows. This study has established the bases for evaluating the FEM and the separation edge problems. The explicit role of the free surface as a characteristic surface of a quasi-linear partial differential equation was demonstrated. While this result is of no interest in analytic solution approaches, it is crucial for numerical approaches and is at the core of the separation edge problems.

A unique weighting scheme for adjusting the free surface velocity potential to meet the required tangent separation condition was devised. The scheme works exceedingly well for slightly three-dimensional flows. However, in highly three-dimensional flows it is probable that both a very refined grid and a different weighting scheme will need to be used.

Both pure drag and lifting flow computations were made. For pure drag, circular and elliptic plates in a water tunnel were studied. The iterative procedure was stable and convergent. The solution accuracy was excellent for the circular plate cases and acceptable for the elliptic plate cases. One lifting flow configuration with a circular plate in a water tunnel was computed. While a stable and convergent solution was again obtained, the constant pressure condition on the free surface was not accurately satisfied.

An extensive review of the performance of the solution was conducted. Several conclusions were drawn. First, the present iterative scheme does not guarantee satisfaction of the constant pressure condition transversely

across the free surface. However, this is of concern only in highly three-dimensional flows; e.g., the pure drag solutions studied gave quite accurate answers, but the lifting flow solution did not. Second, grid refinement (reduction of element size) in the streamwise direction and near separation markedly improves the local quality of the solution, but has little effect on global results, i.e.,  $\sigma$ ,  $C_D^*$ , etc. Third, grid refinement in the transverse direction (perpendicular to the free surface streamlines, but in the free surface) will be necessary to achieve accurate results in highly three-dimensional flows. (A relatively coarse grid has been used so far because of cost.)

Among the alternative strategies for remedying the present problems, only grid refinement or analytic patches to remove the singular nature of  $\phi$  in the neighborhood of the separation edge offer direct solution of the difficulties. While the boundary integral equation method (BIEM) may reduce computation cost and the difficulties associated with generating a "good" finite element net, the BIEM appears to suffer the same weaknesses at separation as the present method.

The simplest strategy for future study appears to be to generate a highly refined FE mesh and then to solve again the present lifting flow case. Use of the BIEM and grid refinement is the next most difficult strategy. Finally, development of analytic solutions for the three-dimensional flow in the neighborhood of separation and the use of such solutions with isoparametric elements are possible in principle, but are well beyond the present state-of-the-art.

## REFERENCES

- Akima, H. (1978). "A Method of Bivariate Interpolation and Smooth Surface Fitting for Irregularly Distributed Data Points", ACM Trans. Math. Software, Vol. 4, No. 2, pp. 148-159.
- Armstrong, A. H. and Dunham, J. H. (1953). "Axisymmetric Cavity Flow", Kent England, Army Res. Estab., Report 12/53.
- Barsoum, R. S. (1976). "On the Use of Isoparametric Finite Elements in Linear Fracture Mechanics", Int. J. Num. Meth. Eng., Vol. 10, pp. 25-37.
- Brebbia, C. A. and Wrobel, L. C. (1979). "Boundary Element Method for Fluid Flow", Advances in Water Resources, Vol. 2, p. 83-89.
- Brennen, C. (1969). "A Numerical Solution of Axisymmetric Cavity Flows", J. Fluid Mech., Vol. 37, Pt. 4, pp. 671-688.
- Chan, S.T.K. and Larock, B. E. (1973a). "Fluid Flows from Axisymmetric Orifices and Valves", J. Hydr. Division, ASCE 99:HY1, pp. 81-97.
- Chan, S.T.K., Larock, B. E. and Herrmann, L. R. (1973b). "Free-Surface Ideal Fluid Flows by Finite Elements", J. Hydr. Division, ASCE 99:HY6, pp. 959-974.
- Concus, P., Golub, G. H. and O'Leary, D. P. (1975). "A Generalized Conjugate Gradient Method for the Numerical Solution of Elliptic Partial Differential Equations", Report No. LBL-4604, Lawrence Berkeley Laboratory, University of California, Berkeley, September.
- Crank, J. and Furzeland, R. M. (1978). "The Numerical Solution of Elliptic and Parabolic Partial Differential Equations with Boundary Singularity", J. Comp. Physics, Vol. 26, pp. 285-296.
- de Boor, C. (1978). A Practical Guide to Splines. Springer.
- Ergatoudis, J. G., Irons, B. M. and Zienkiewicz, O. C. (1968). "Curved Isoparametric Quadrilateral Elements for Finite Element Analysis", Int. J. Solids Struct., Vol. 4, pp. 31-42.
- Fulker, D. (1978). Private Communication. National Center for Atmospheric Research, Boulder, Colorado.
- Furuya, O. (1975). "Three-Dimensional Theory on Supercavitating Hydrofoils near a Free Surface", J. Fluid Mech., 71, pp. 339-359.
- Henshell, R. D. and Shaw, K. G. (1975). "Crack Tip Finite Elements are Unnecessary", Int. J. Num. Meth. Eng., Vol. 9, pp. 495-507.
- Hibbitt, H. D. (1977). "Some Properties of Singular Isoparametric Elements", Int. J. Num. Meth. Eng., Vol. 11, pp. 180-184.

- Huebner, K. H. (1975). The Finite Element Method for Engineers. New York Wiley-Interscience.
- Irons, B. M. (1966). "Engineering Application of Numerical Integration in Stiffness Method", AIAA J., Vol. 4, pp. 2035-2037.
- Irons, M. B. (1970). "A Frontal Solution Program for Finite Element Analysis", Int. J. Num. Meth. Eng., Vol. 2, pp. 5-32.
- Jeppson, R. W. (1972) "Inverse Solution to Three-Dimensional Potential Flows", J. Engin. Mech. Div., ASCE 98:EM4, pp. 789-812.
- Jiang, C. W. and Leehey, P. (1977). "A Numerical Method for Determining Forces and Moments on Supercavitating Hydrofoils of Finite Span", Second Intl. Conf. Ship Hydrodyn., Berkeley, California. Sept. 19-21.
- Ko, P. Y. and Street, R. L. (1979). "Program Documentation for Cavity Flow Simulation," Department of Civil Engineering, Stanford University. Tech. Rept. No. 243. November.
- Larock, B. E. and Taylor, C. (1976). "Computing Three-Dimensional Free Surface Flows", Int. J. Num. Meth. Eng., Vol. 10, pp. 1143-1152.
- Larock B. E. (1977). "An Application of the Boundary Integral Equation Method to Cavity and Jet Flows", Proc. Second International Conf. on Ship Hydrodynamics, Berkeley, California. Setp. 19-21.
- Leehey, P. and Stellingner, T. S. (1975). "Force and Moment Measurements of Supercavitating Hydrofoils of Finite Span with Comparison to Theory", J. Fluids Engrg., Transact. ASME, 97, pp. 453-464.
- Mogel, T. R. and Street, R. L. (1974). "A Numerical Method for Steady-State Cavity Flows", J. Ship Res., Vol. 18, No. 1, pp. 22-31.
- Nishiyama, T. (1970). "Lifting-Line Theory of Supercavitating Hydrofoil of Finite Span", ZAMM, Vol. 50, pp. 645-653.
- Pinder, G. E. and Gray, W. G. (1977). Finite Element Simulation in Surface and Subsurface Hydrology, Academic Press.
- Prenter, P. M. (1975). Splines and Variational Methods, Wiley-Interscience.
- Sarpkaya, T. and Hiriart, G. (1975). "Finite Element Analysis of Jet Impingement on Axisymmetric Curved Deflectors", Finite Elements in Fluids, Vol. 1, Wiley. Gallaher, Oden, Taylor and Zienkiewicz, editors.
- Spath, H. (1973). Spline-Algorithmen zur Konstruktion glatter Kurven und Flächen, R. Oldenbourg Verlag, Munchen, Wien.
- Strang, G. and Fix, G. J. (1973). An Analysis of the Finite Element Method, Prentice-Hall, N. J.

- Street, R. L. and Larock, B. E. (1968). "Cambered Bodies in Cavitating Flow-- A Nonlinear Analysis and Design Procedure", J. Ship Res., Vol. 12, pp. 1-13.
- Street, R. L. (1977). "Review of Numerical Methods for Solution of Three Dimensional Cavity Flow Problem", Proc. Second International Conf. on Numerical Ship Hydrodynamics, Setp. 19-21, 1977, U. of California, Berkeley, California.
- Taig, I. C. (1961). "Structural Analysis by the Matrix-Displacement Method", Engl. Elect. Aviat. Report No. S017.
- Thompson, J. F., Thames, F. C. and Mastin, C. W. (1974). "Automatic Numerical Generation of Body-Fitted Curvilinear Coordinate System for Field Containing Any Number of Arbitrary Two-Dimensional Bodies", Journal of Computational Physics, Vol. 15, p- 299-319.
- Tsen, L. F. and Guilbaud, M. (1974). "A Theoretical and Experimental Study on The Planform of Superventilated Wings", J. Ship Res., 18, pp. 169-184.
- Tulin, M. P. (1963). "Supercavitating Flows - Small Perturbation Theory", TR 121-3, Hydronautics, Inc.
- White, J. W. and Kline, S. J. (1975). "A Calculation Method for Incompressible Axisymmetric Flows, Including Unseparated, Fully Separated, and Free Surface Flows", Dept. of Mech. Engrg., Thermosci. Div., Stanford University, Rept. MD-35, Stanford, California.
- Widnall, S. E. (1966). "Unsteady Loads on Supercavitating Hydrofoils" J. Ship Res., 9, pp. 107-118.
- Wu, T. Y. (1968). "Inviscid Cavity and Wake Flows", Basic Developments in Fluid Dynamics, M. Holt, Editor, Vol. 2, pp. 1-76.
- Wu, T. Y. (1972). "Cavity and Wake Flows", Annual Review of Fluid Mechanics, Vol. 4, pp. 243-283.
- Zienkiewicz, O. C. (1971). The Finite Element Method in Engineering Science. London, McGraw-Hill.

## APPENDIX 1

### MESH GENERATION AND ELEMENT ORGANIZATION

One of the most time consuming tasks in the FEM is setting up the geometric input for a not-so-regular domain, especially in three dimensions. However, by use of a semi-automatic method, the geometric input for this three dimensional cavitation flow (i.e., plates in a rectangular water tunnel) can be set up relatively painlessly. The flow domain is divided into two parts, namely, a rod and the main flow section (see Figure A.1.1). The tracking of the node numbers is accomplished by means of two three-dimensional arrays, namely, MP ( $\alpha, \beta, \gamma$ ) for the main flow and MPR ( $\alpha_R, \beta_R, \gamma_R$ ) for the rod. Here,  $\alpha$ ,  $\beta$  and  $\gamma$  are the three curvilinear "axes" for the main flow as shown in Figure A.1.1(a) with maximum values of NROWS, NCOLS and NDEEP respectively, while  $\alpha_R$ ,  $\beta_R$  and  $\gamma_R$  are their counterparts for the rod section as shown in Figure A.1.1(b) with maximum values of NROWR, NCOLR and NDEEPR respectively. Note that NDEEPR is function of the value of  $\alpha_R$  (counting the "0" nodes). Therefore, with a given set of values of  $\alpha$ ,  $\beta$  and  $\gamma$ , one can pinpoint the node number. By means of this curvilinear axes system, the free surface can be identified straight-forwardly, namely,  $\alpha = 1$  and  $\beta > \text{NFREE}$  (Counting from separation where  $\beta$  equals NFREE). In the present configuration,  $\beta$  and  $\beta_R$  coincide with the x-axis.

#### A.1.1 Pure Drag Case

Because of the symmetry in the flow field, only  $\frac{1}{2}$  of the flow field need be considered (refer to Figure A.1.2). The schematic grid is first sketched by hand such that elements around the separation are smaller. The size of the rod is set arbitrarily. Then, for each section of the main flow in  $\beta$ -direction, the height  $h$  is measured together with  $h_1$ ,  $h_2$  and  $h_3$  (only three layers are shown in this example).

The ratios

$$\left. \begin{aligned} r_1 &= \frac{h_1}{h} \\ r_2 &= \frac{h_2}{h} \end{aligned} \right\} \quad (\text{A.1.1})$$



and

$$r_3 = \frac{h_3}{h} \left. \vphantom{\frac{h_3}{h}} \right\}$$

are computed. This represents the distance between layers in the  $\alpha$  direction. Using ratios  $r_1$ ,  $r_2$  and  $r_3$ , planes for each  $\gamma$  (at a discrete value of  $\theta$ ) are discretized accordingly. The sum of all  $r$  ratios equals unity, i.e.,  $\sum_{i=1}^3 r_i = 1$ .

#### A.1.2 Lifting Flow Case

Following the general procedure used in the pure drag case, one first generates a pure-drag half-flow by imaging the quarter flow as shown in Figure A.1.3. Then the plate is tilted to the desired angle of attack  $\bar{\alpha}$ . The grid points are next moved proportionally to their locations with respect to the separation edge and the fixed tunnel boundary as indicated by the dotted lines in Figure A.1.3. Figure A.1.4 shows a typical arrangement of the grid at an angle of attack of 60 degrees.

By means of this procedure, one can generate a three dimensional, lifting-flow grid relatively painlessly. However, elements around the leading edge might have shapes which are not "nice" in the context of the FEM. It is, therefore, necessary to have the grid plotted and examined. If the situation arises in which badly distorted elements occur, the grid is adjusted semi-manually. As seen in Figure A.1.5, it is desirable to have the internal angle  $\theta_1$  smaller. It is done by pivoting the imaginary line A-A joining points T and B at some point and rotating the line to position A'-A'. Then the intermediate nodes are moved proportionally on the line A'-A'. The position of the pivot governs the relative movement of the points T and B. For instance, if point B were to be fixed, the pivot is set at that point.

The input sequences and the program listings are given in a separate Program Manual (Ko and Street, 1979). Therefore, they are not repeated here.

## APPENDIX 2

### LARGE MATRIX EQUATION SOLVING ALGORITHM

As mentioned in Section 2, it is necessary to solve a large, sparse system of algebraic equations. Due to the fact that the global stiffness matrix,  $K_{ij}$  in Equation 2.25 is positive definite and symmetric, one has the liberty of choosing a direct method over an iterative method or vice versa. The choice of one method over the other, generally, depends on the availability of core storage and one's willingness to spend computing time. For the direct method, the storage requirement depends on the bandwidth of the coefficient matrix of the system and on a clever numbering scheme of elements and nodes in the FEM formulation. In the present study, a direct method using a frontal technique with Gaussian Elimination and an iterative technique with Conjugate Gradient method were tested. The iterative Conjugate Gradient method (ICGM) as implemented here enjoys one significant advantage, namely, the core storage is only a fixed multiple of the number of unknowns and is independent of the numbering scheme. This resulted in substantial savings in core storage compared to the direct method. However, the overall computing time is longer in the problem tested here for the ICGM.

In the FEM, the global stiffness matrix  $K_{ij}$  in Equation 2.25 is usually banded, but the band width depends on the type of elements used and the numbering scheme. Often it is this global matrix together with fill-ins which occur during application of direct methods, which require more core storage than is available economically or, often, actually. However,  $K_{ij}$  need not be stored. It is the elemental stiffness matrices  $K_{ij}^{(e)}$  in Equation 2.22 which must be saved along with the nodal connection matrix  $v$ . Both the direct and the iterative methods operate from this same data base.

#### A.2.1 The Direct Method by Gaussian Elimination

The solution of the FEM formulation equation set by Gaussian Elimination is well known (Irons, 1970 and Zienkiewicz, 1971). The method described here appears in a program supplied by C. Taylor, University of Swansea, U.K. (see, e.g., Larock and Taylor, 1976). A modified version of this program was used for the present flow problems.

The elemental stiffness matrices are generated and stored on disk. They are read into core one at a time filling the coefficient matrix in a wedge area until the matrix just read in does not affect the first row (or equation) in the "wedge" (see Fig. A.2.1), which moves along the diagonal and covers the upper half of the coefficients present in the global stiffness matrix, then Gaussian Elimination is performed on the first row. The resulting first row is saved on another disk file and the "wedge" is moved down one row. More elemental matrices are then read in. This procedure is repeated  $n$  times, where  $n$  is the total number of nodes in the problem. Next, back substitution can be performed by recalling the rows stored on the second disk file one at a time in inverse order of storage (last in, first out). The core storage requirement of the "wedge" depends on the bandwidth which in turn depends on the element and nodal numbering schemes. No pivoting is performed. This may lead to loss of accuracy in some problems, but no difficulties were encountered in the present cases with up to 3137 node points.

#### A.2.2 Iterative Conjugate Gradient Method

According to Concus, et al. (1975), the Conjugate Gradient method was proposed by Hestenes and Stiefel in 1952. It was not until the early 1970's that it was found to be highly effective as an iterative procedure for solving large sparse systems of linear equations. The method is based on splitting off from the original coefficient matrix a symmetric, positive-definite matrix that is more easily solved, and then accelerating the iteration using conjugate gradients. The convergence of the CG method is assured for matrices of the type generated by the FEM formulation described above (cf., Concus, et al. 1975). The CG method is described briefly below.

Consider the system of equations

$$Ax = c \quad (A.2.1)$$

where  $A$  is an  $l \times l$ , symmetric, positive-definite matrix. It is split such that

$$A = M - N \quad (A.2.2)$$

where  $M$  is positive-definite and symmetric and  $N$  is symmetric. Thus, from (A.2.1)  $Mx = Nx + c$ . It is assumed that

$$Mx = d$$

can be solved more easily than (A.2.1).

Following Concus, et al. (1975), the CG algorithm can be stated as follows:

Let  $x^{(0)}$  and  $p^{(-1)}$  be any arbitrary vectors. For  $k = 0, 1, 2, \dots$

(1) Solve

$$Mz^{(k)} = c - Ax^{(k)}$$

(2) Compute

$$b_k = \frac{z^{(k)T} Mz^{(k)}}{z^{(k-1)T} Mz^{(k-1)}}, \quad k \geq 1$$

$$b_0 = 0$$

$$p^{(k)} = z^{(k)} + b_k p^{(k-1)}$$

(3) Compute

$$a_k = \frac{z^{(k)T} Mz^{(k)}}{p^{(k)T} Ap^{(k)}},$$

and

$$x^{(k+1)} = x^{(k)} + a_k p^{(k)}$$

The above algorithm is very simple and very easily programmed. The maximum value of  $a_k p^{(k)}$  in step 3 above is used as the maximum error between iterations. Instead of computing the right-hand side of step 1 explicitly, one could use the following recursive form

$$\begin{bmatrix} c - Ax^{(k+1)} \end{bmatrix} = \begin{bmatrix} c - Ax^{(k)} \end{bmatrix} - a_k Ap^{(k)} \quad (\text{A.2.3})$$

The greatest advantage for the CG method is that one has complete liberty in choosing the matrix  $M$  in (A.2.2). If

$$M = \text{Diag} (A) , \quad (\text{A.2.4})$$

the vector  $z$  can be very easily found. The matrix  $A$  is used only once every iteration except for the starting iteration. If  $A$  is the coefficient (global stiffness) matrix  $K$  in (2.25)

$$M = \text{Diag} (K) , \quad (\text{A.2.5})$$

$c \in R$ , and the final  $x$  is the solution function  $\phi$  in (2.25). In computing  $Ap^{(k)}$  in step 3 above, one need only use the elemental stiffness matrices  $K^{(e)}$  from (2.22) as follows. For each element, let  $S^{(e)}$  be defined as the selection matrix of dimension  $n \times \ell$  with

$$i^{\text{th}} \text{ row of } S^{(e)} = \mu_{i(j)} \quad (\text{A.2.6})$$

where

$$\left\{ \mu_{i(j)} \right\} = \begin{cases} 1 & \text{if } j = v_i \\ 0 & \text{otherwise} \end{cases} \quad (\text{A.2.7})$$

and  $i(j)$  are all distinct for  $i = 1, \dots, n$ ; then it can be easily seen that

$$Ap^{(k)} \equiv Kp^{(k)} = \sum_{(e)} K^{(e)} S^{(e)} p^{(k)} \quad (\text{A.2.8})$$

However, the elemental stiffness matrices need to be preprocessed to incorporate the Dirichlet boundary conditions in (2.18) before the start of the CG iterations.

Let  $s$  be the set of nodes on  $S_1$  with  $\phi$  the corresponding boundary values. Before the CG method can be applied directly, the elemental matrices (2.22) have to be preprocessed as follows:

$$(i) \text{ Set } R_{v_i} = K_{ii}^{(e)} \phi(v_i) \text{ for all } i = 1, \dots, n$$

$$\text{such that } v_i \in s \quad (A.2.9)$$

$$(ii) \text{ For } i = 1, 2, \dots, n, \text{ such that } v_i \in s$$

$$\text{set } R_{v_j} = R_{v_j} - K_{ji}^{(e)} \phi(v_i) \text{ for all } j = 1, \dots, n$$

$$\text{such that } (v_j \in s \text{ and } v_j \neq v_i) \quad (A.2.10)$$

$$(iii) \text{ Set } K_{ij}^{(e)} = 0 \text{ for all } i, j = 1, 2, \dots, n$$

$$\text{such that } i \neq j \text{ and } (v_i \in s \text{ or } v_j \in s) \quad (A.2.11)$$

Then the processed elemental and the global matrix equations become

$$\bar{K}^{(e)} \bar{\phi}^{(e)} = \bar{R}^{(e)} \quad (A.2.12)$$

$$\bar{K} \bar{\phi} = \bar{R} \quad (A.2.13)$$

respectively.

It can be easily shown that the submatrix of  $\bar{K}$  (with the known values deleted) is essentially a principal submatrix of  $K$  and is therefore symmetric and positive-definite. Accordingly, the CG algorithm can be applied to solve (A.2.13). The starting vector  $x$ , of course, has some known values, such that

$$x_i = \begin{cases} \phi_i & \text{for all } i \in S_1 \\ \text{best estimates} & \text{otherwise} \\ \text{or simply, 0} & \end{cases} \quad (A.2.14)$$

### A.2.3 Numerical Test

The CG algorithm and the direct solution method were tested on the IBM 370/168 of the Stanford Linear Accelerator Center Triplex System. For a problem with 1713 nodes, 304 elements and 163 Dirichlet boundary nodes, the estimated bandwidth of  $\bar{K}$  was 160. The CG algorithm took approximately 0.5 sec per iteration. Approximately 40 percent of this time was used in the IBM I/O handling routine, 30 percent in the main program, and 30 percent in the system routines other than I/O. In the case of double precision arithmetic (56 binary bits), the solution converged to machine precision in about 300 iterations. Figure A.2.2 shows the sequence of convergence.

For the present CG algorithm, one must save five vectors of the size of the total number of nodes in the FEM formulation. In this test case, the CG savings in core storage as compared to the direct method outlined in Section A.2.1 was 40 percent. However, the total computing time for CG as compared to that for the direct method was approximately 1.5:1. For another larger problem with 2647 nodes, 496 elements, 303 Dirichlet boundary nodes, and an estimated bandwidth of 260 for  $\bar{K}$ , the CG savings in core storage is approximately 60 percent.

Table 5.1 Summary of Results for Circular Plates in Square Water Tunnels

Case	F	L	W	P	W/P	B (MID.)	B/P	U	q <sub>c</sub>	σ	C <sub>D</sub> <sup>*</sup>
2	10	10	10	2	5	4.087	2.044	0.97297	1.1622	0.4268	0.8300
1	10	5	10	2	5	3.428	1.714	0.97297	1.2097	0.5458	0.8336
3	10	10	7.5	2	3.75	3.898	1.949	0.97297	1.2412	0.5274	0.8471
12	10	5	7.5	2	3.75	3.414	1.707	0.97297	1.2639	0.6876	0.8471
5	10	10	5	2	2.5	3.382	1.691	0.97297	1.4578	1.2449	0.8690
4	10	5	5	2	2.5	3.223	1.612	0.97297	1.4599	1.2514.	0.8690
7†	10	10	5	2	2.5	3.374	1.687	0.97297	1.4546	1.2351	0.8683
8†	10	5	5	2	2.5	3.213	1.607	0.97297	1.4570	1.2424	0.8687
9‡	10	10	5	2	2.5	3.374	1.687	0.97297	1.4546	1.2349	0.8689
10‡	10	5	5	2	2.5	3.213	1.607	0.97297	1.4570	1.2426	0.8695

† 1st level refinement.

‡ 2nd level refinement.



Table 5.2 Summary of Results for Elliptic Plates in Rectangular Water Tunnels

Case	F	L	W	D	P	Q	$U_{\infty}$	$q_c$	L/P	W/P	D/Q	$\sigma$	$C_D^*$	(Transverse) Freestream Velocity Error (Percent)	Remarks
E1	20	20	20	40	3.25	7.75	0.97297	1.1471	6.15	6.15	5.16	0.3899	0.787	3.3	Large tunnel
E2	20	10	10	20	3.25	7.75	0.97297	1.3576	3.08	3.08	2.58	0.9470	0.829	6.5	Short cavity
E3	20	20	10	20	3.25	7.75	0.97297	1.3453	6.15	3.08	2.58	0.9117	0.831	3.6	Standard case

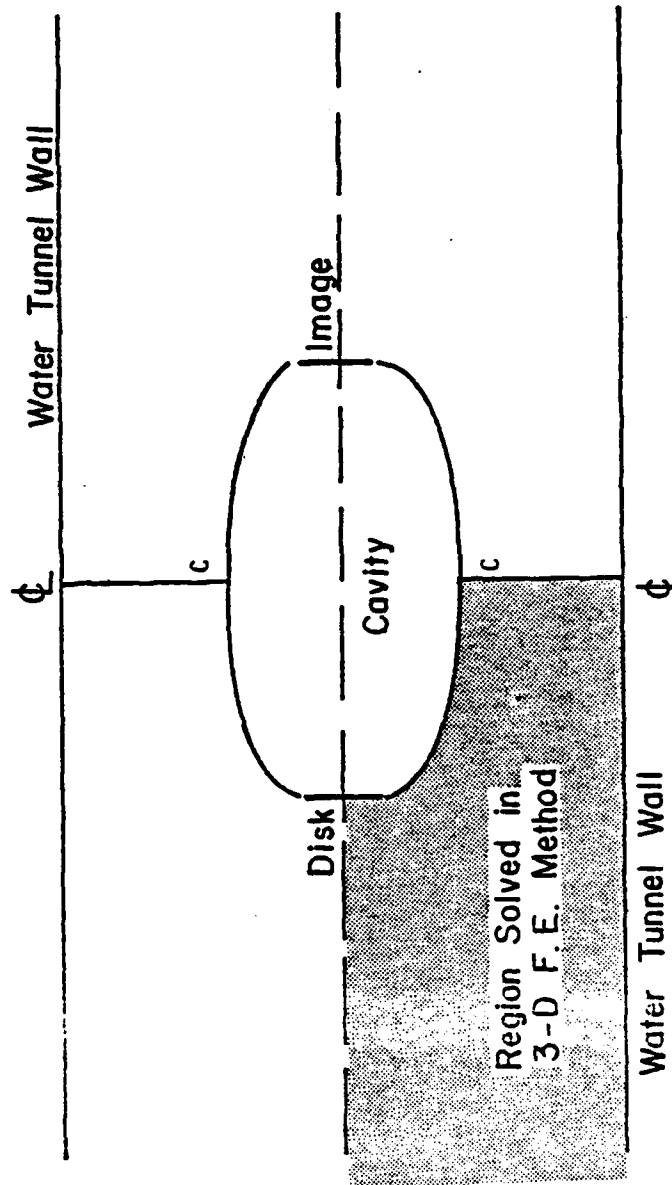


Figure 2.1 Risbouchinsky cavity flow model

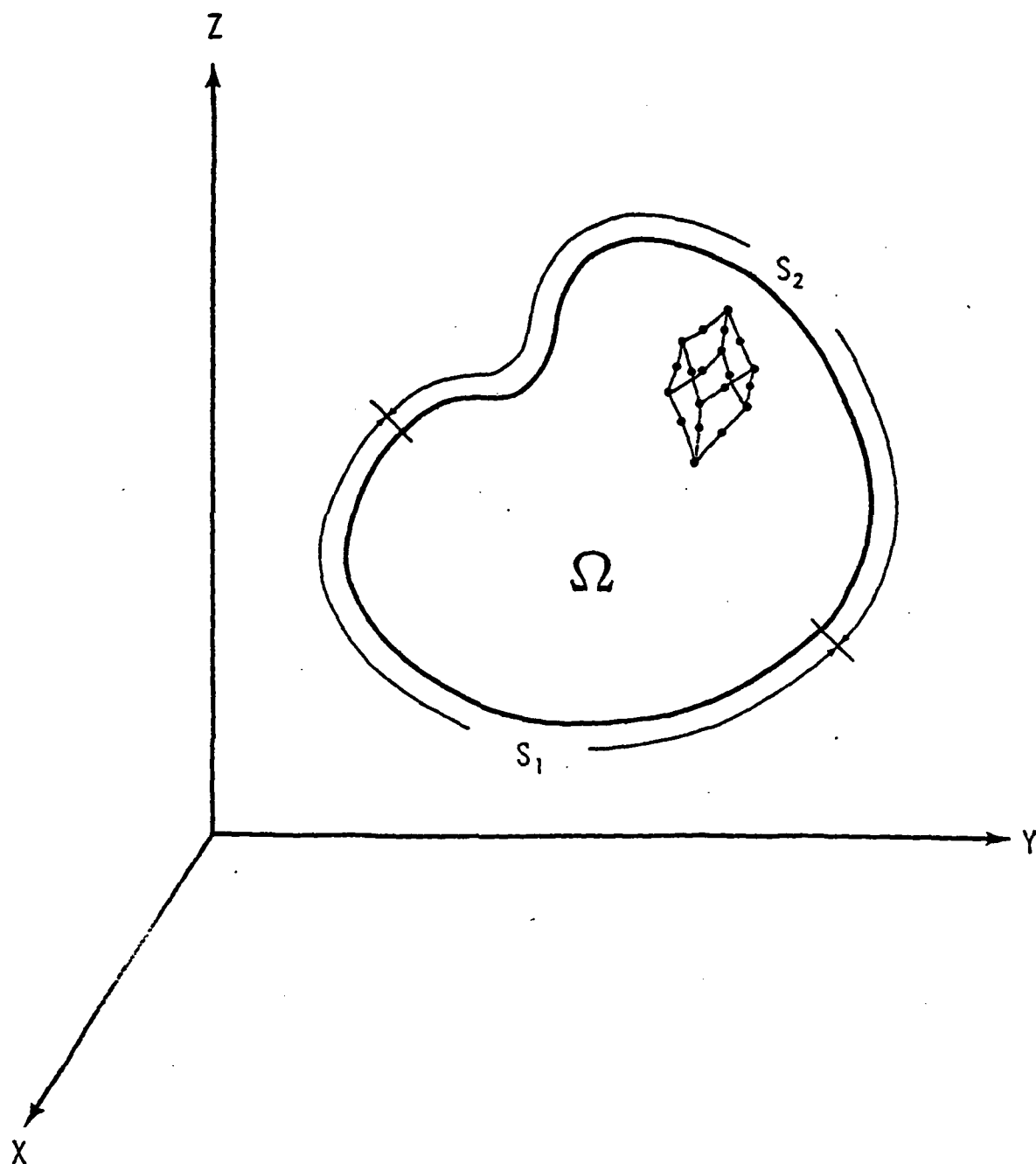


Figure 2.2 Schematic of finite element solution domain

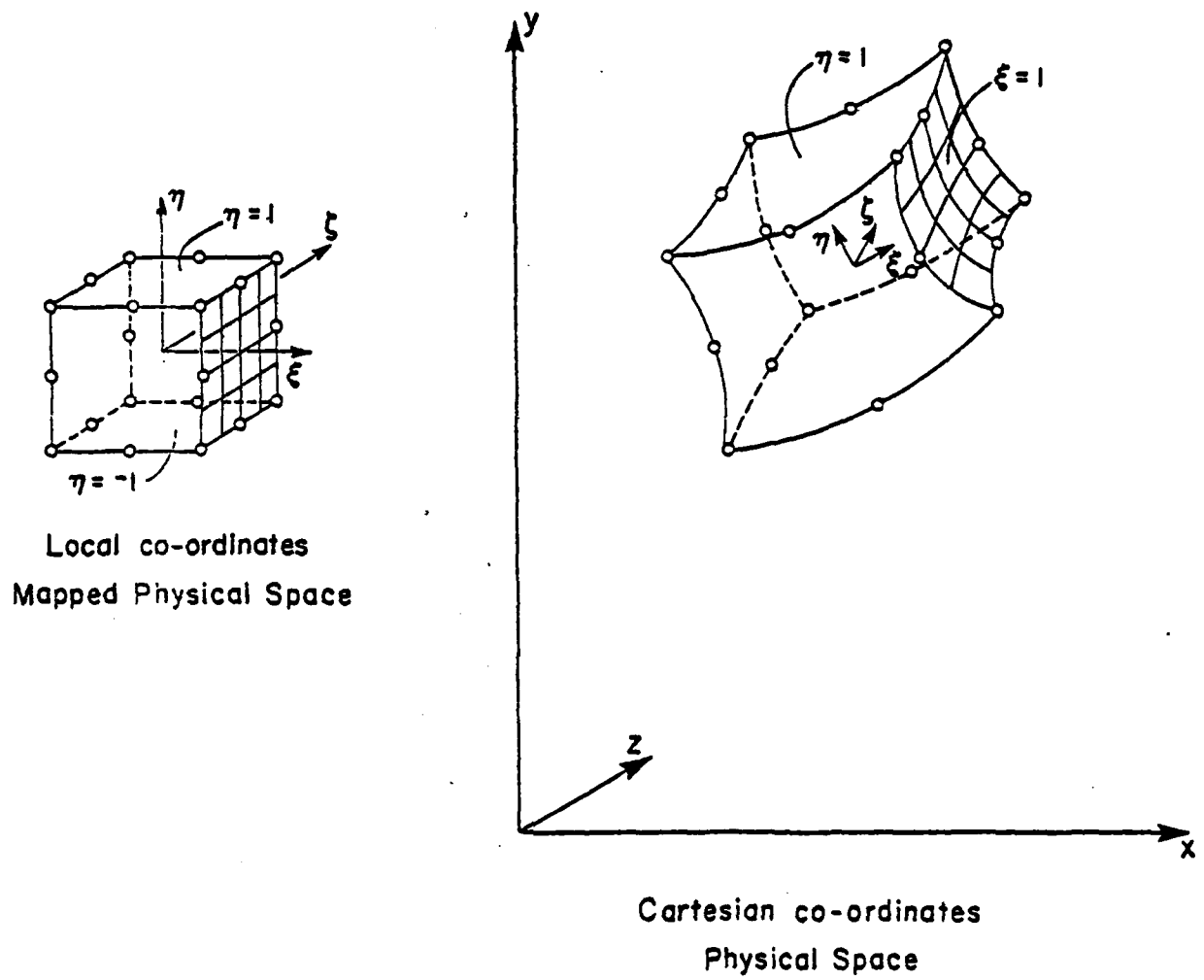


Figure 2.3 The isoparametric finite element



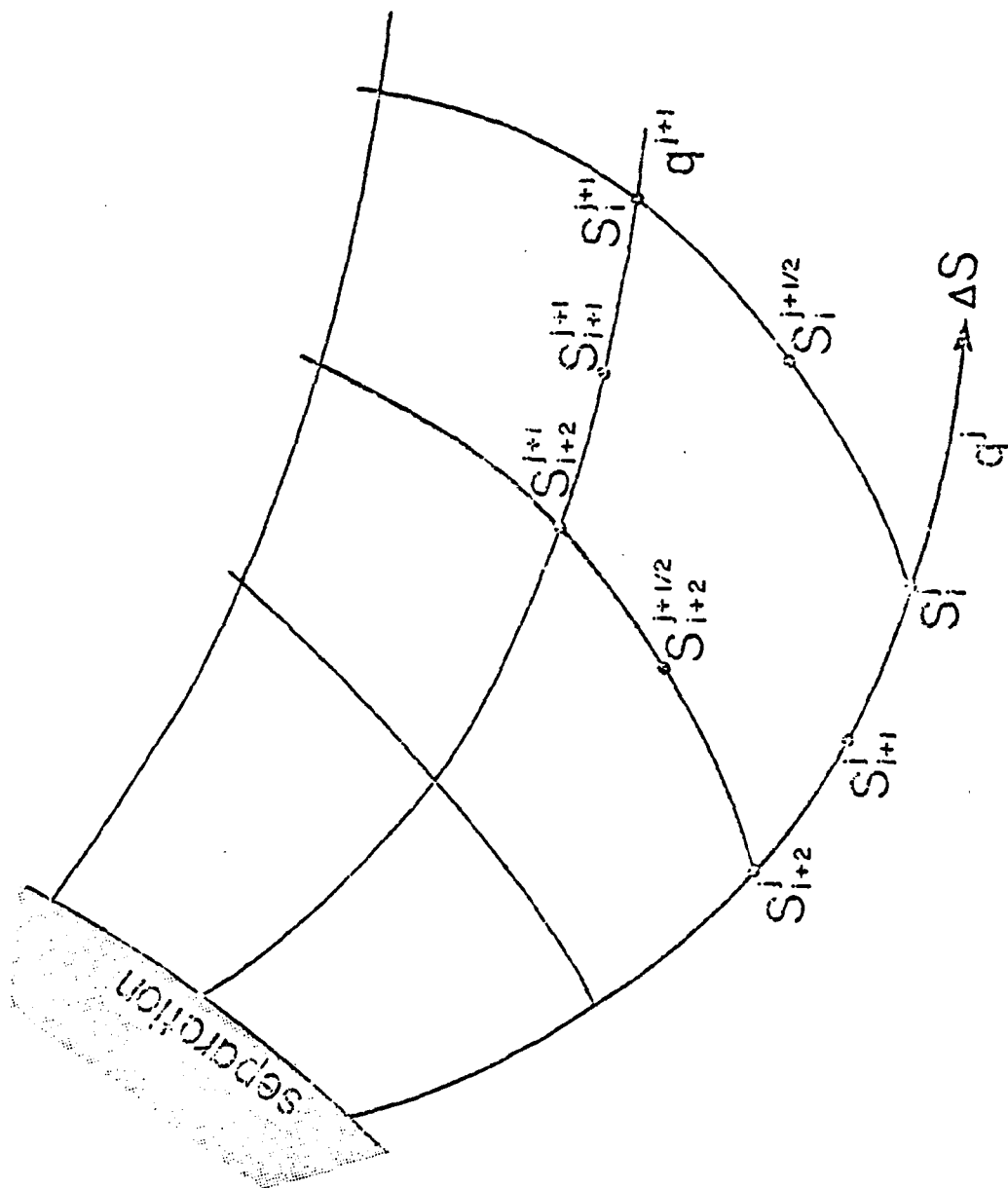


Figure 2.5 Schematic of streamline integration of velocity potential  $\phi$

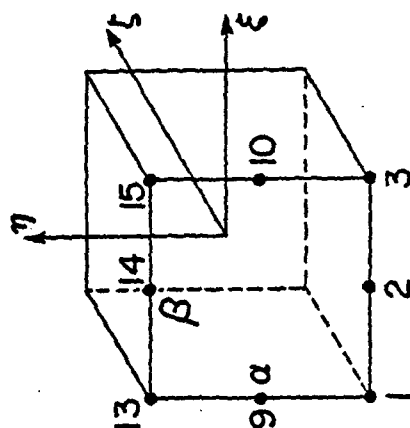
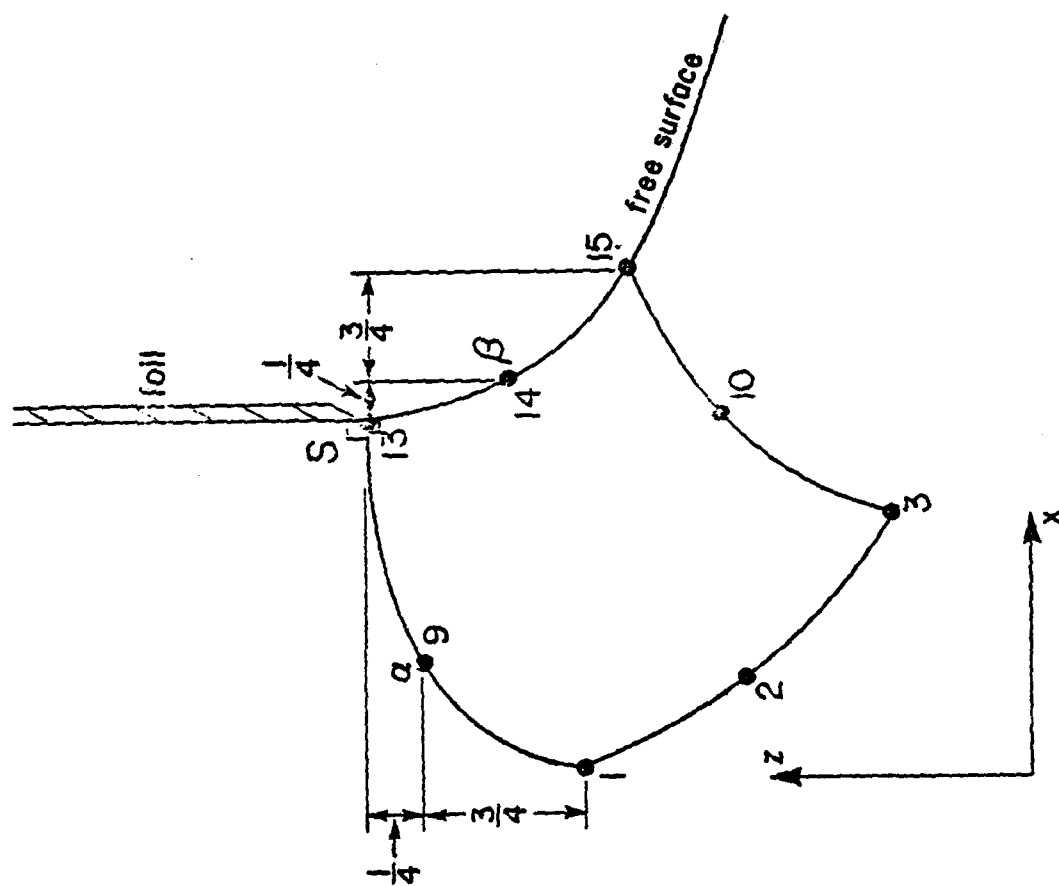


Figure 2.6 Element at separation showing quarter point location

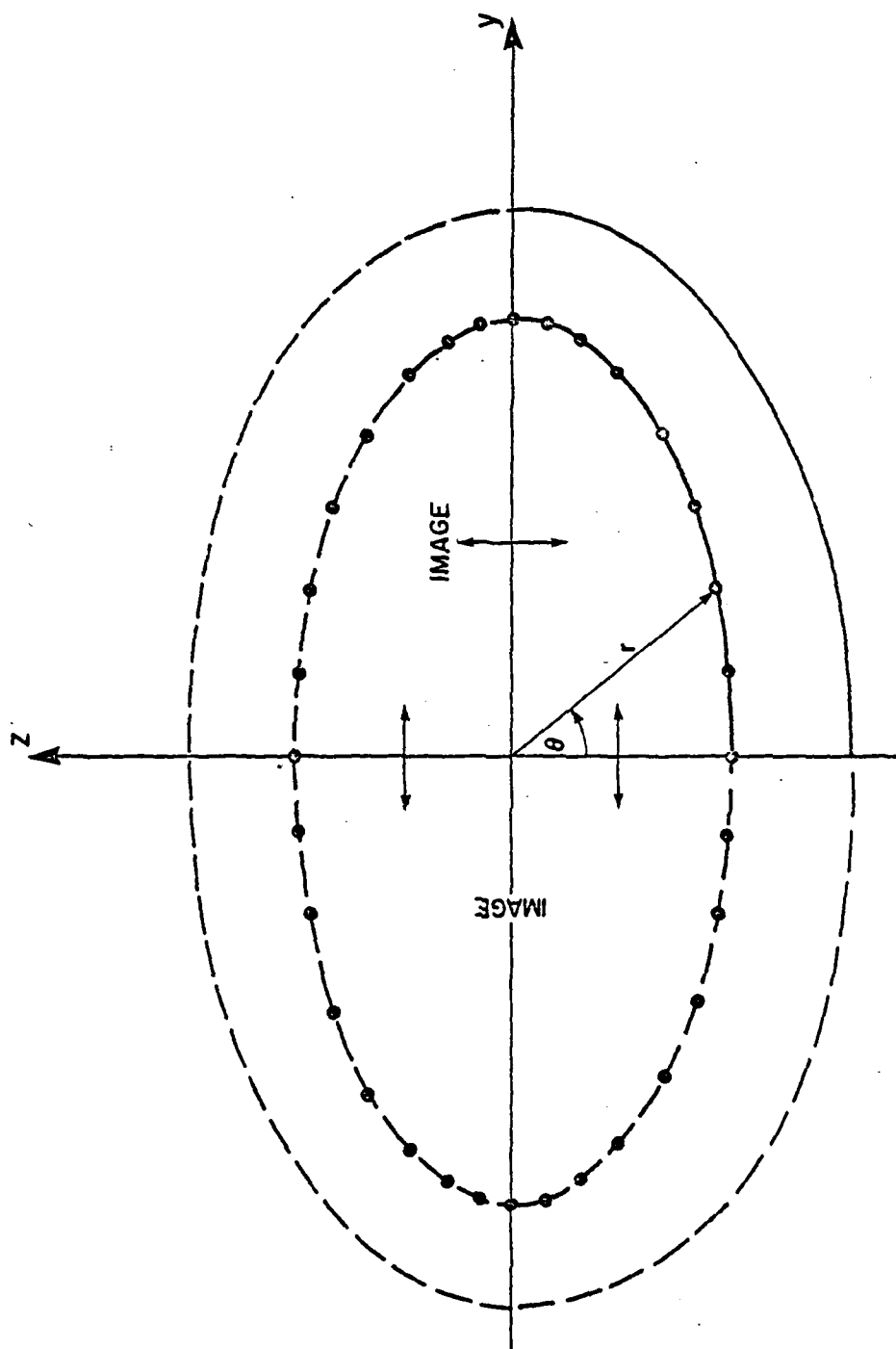


Figure 3.1 Definition of node point locations for periodic cubic spline interpolation



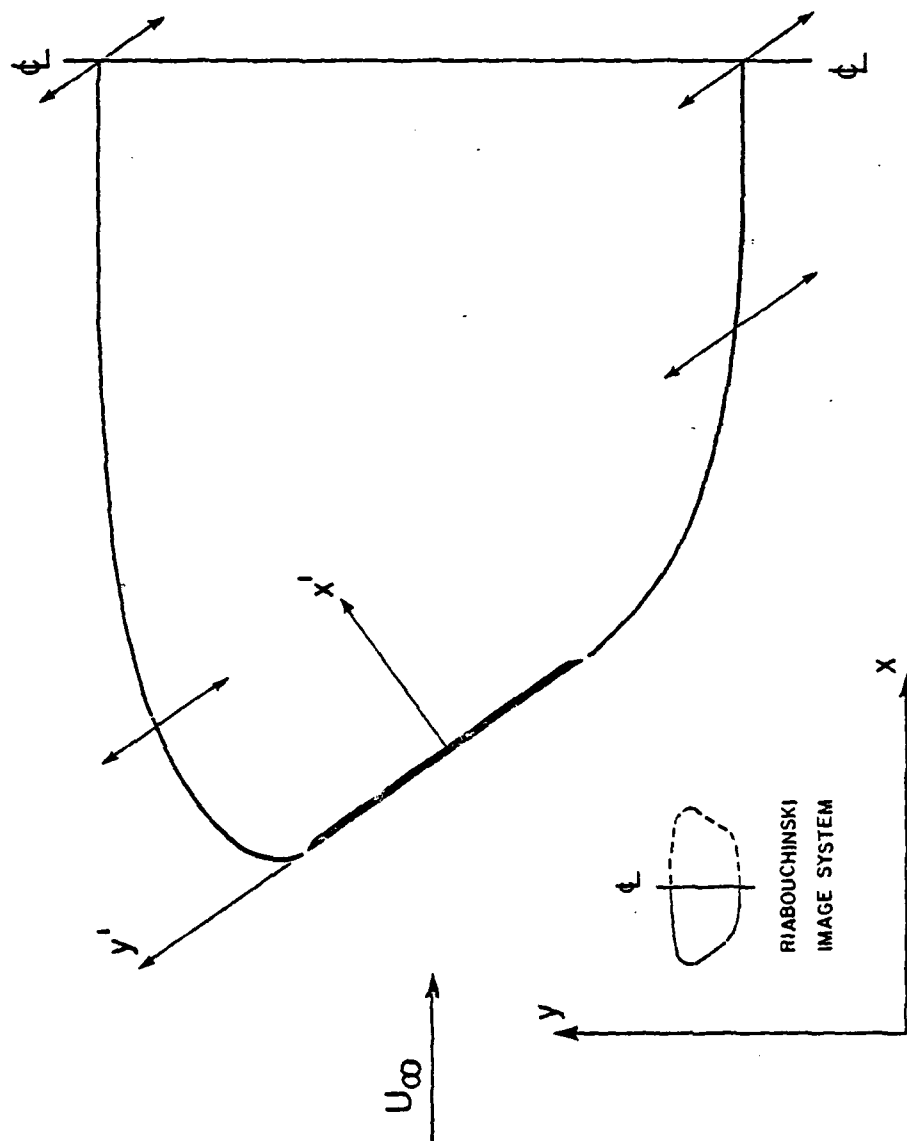


Figure 3.2 Schematic of node point movement for lifting flow

AD-A082 823

STANFORD UNIV CALIF DEPT OF CIVIL ENGINEERING

F/8 20/4

FINITE ELEMENT SIMULATION OF SIMPLE THREE-DIMENSIONAL FULLY CAV--ETC(U)

NOV 79 P Y KO, R L STREET

N00014-75-C-0277

UNCLASSIFIED

TR-241

NL

2 of 2

41 4  
100 100



END

DATE

FILMED

5-80

DTIC

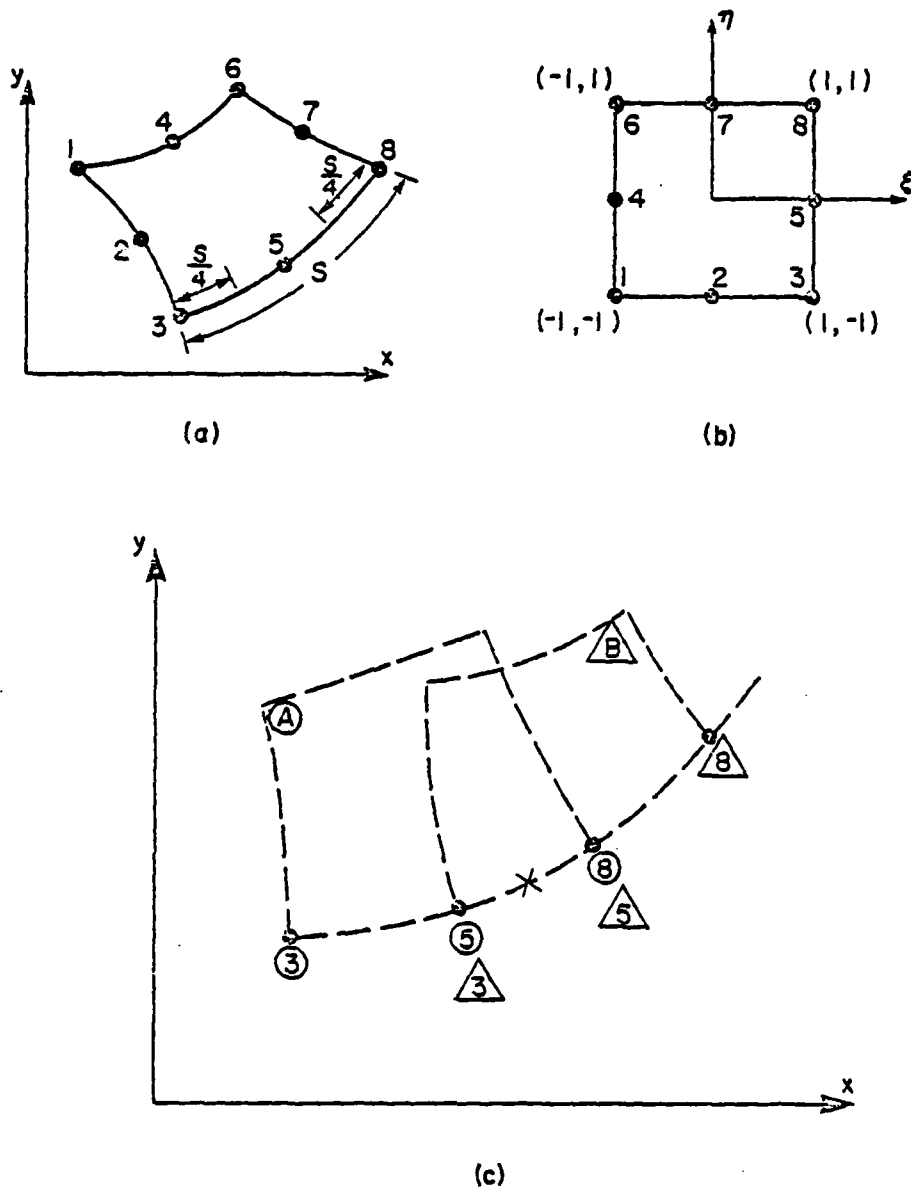


Figure 3.3 The three-dimensional isoparametric interpolation

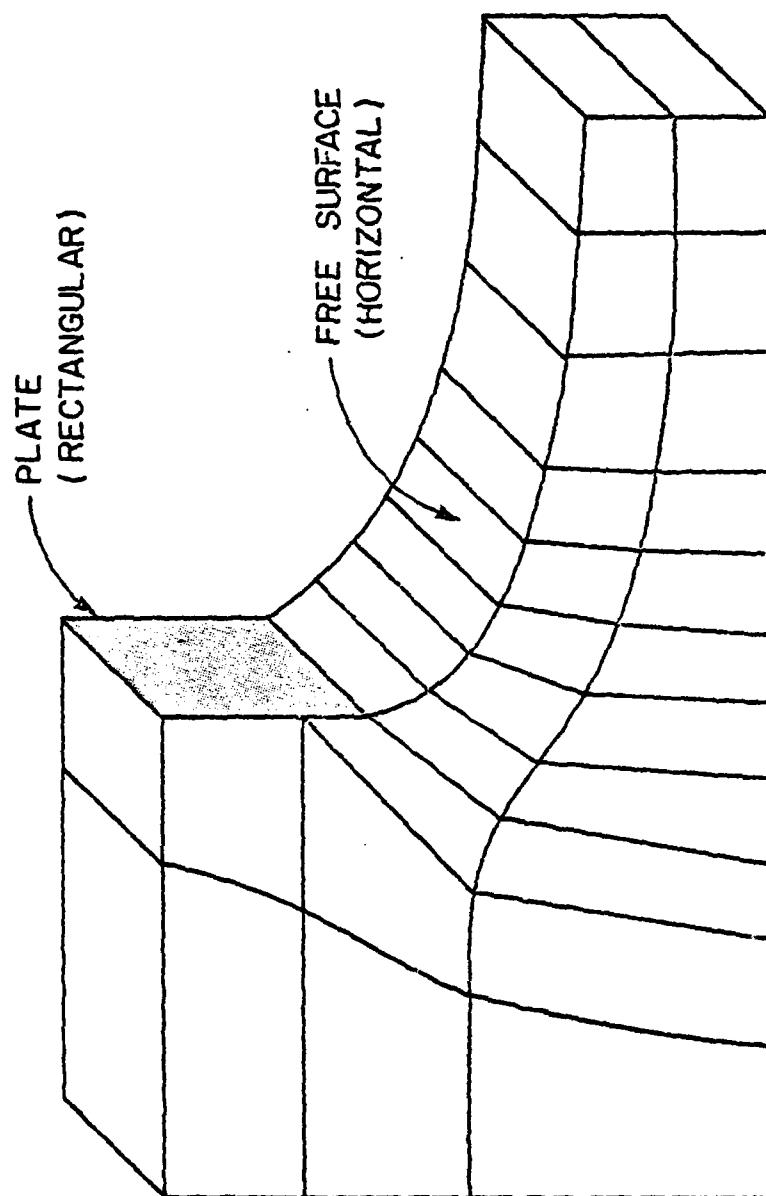


Figure 4.1 Two-dimensional cavity flow configuration

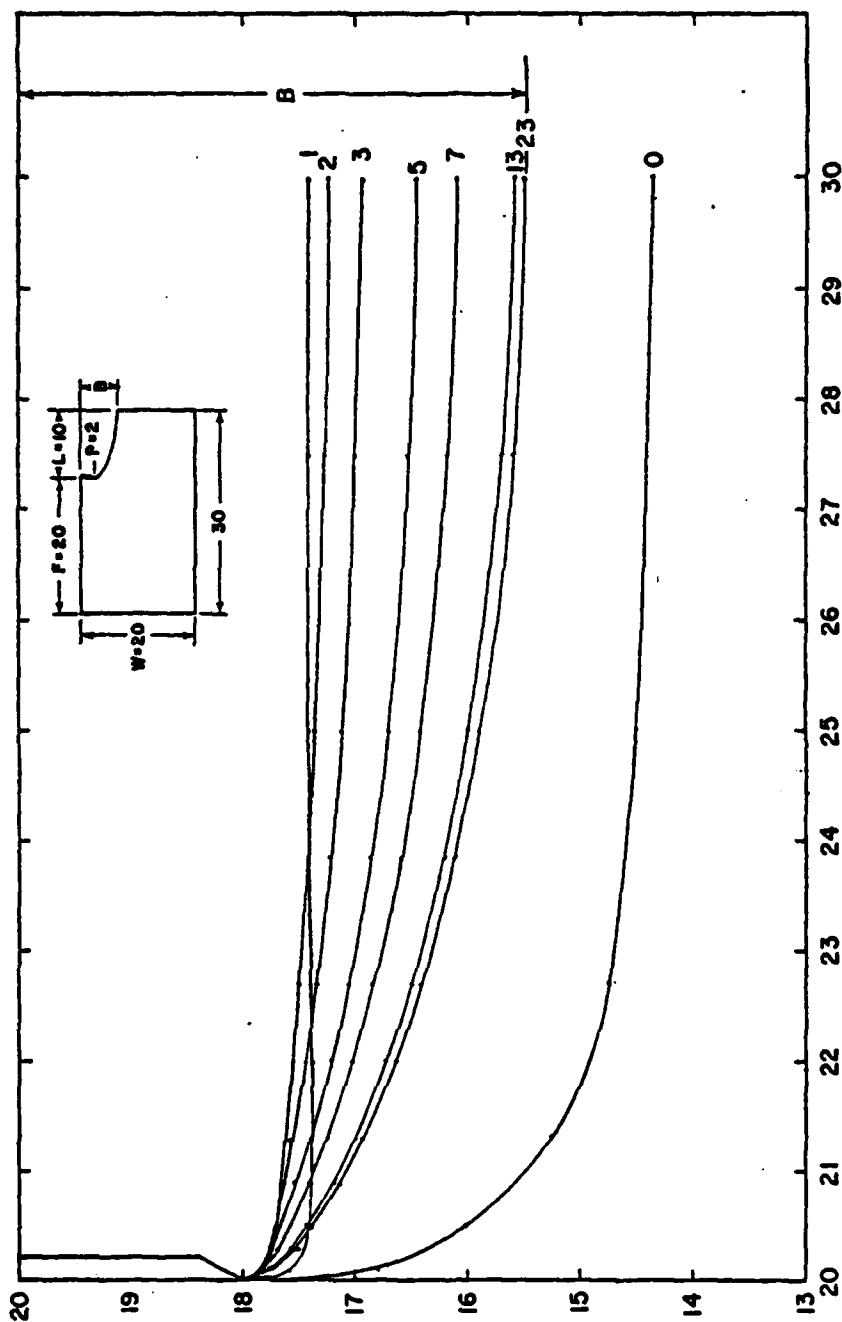


Figure 4.2 Sequence of convergence of free surface for the two-dimensional cavity flow

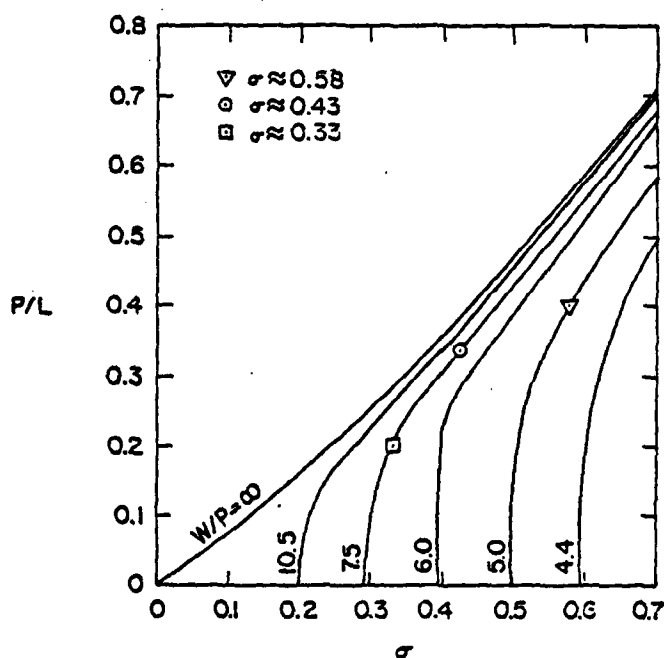
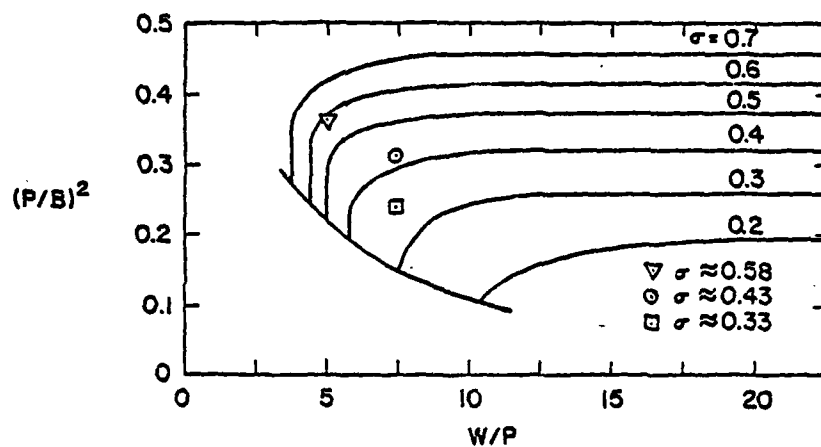


Figure 4.3 Comparison of simulation of axisymmetric cavity flow by three-dimensional model and Brennen's results (1969). Curves are from Brennen (1969)

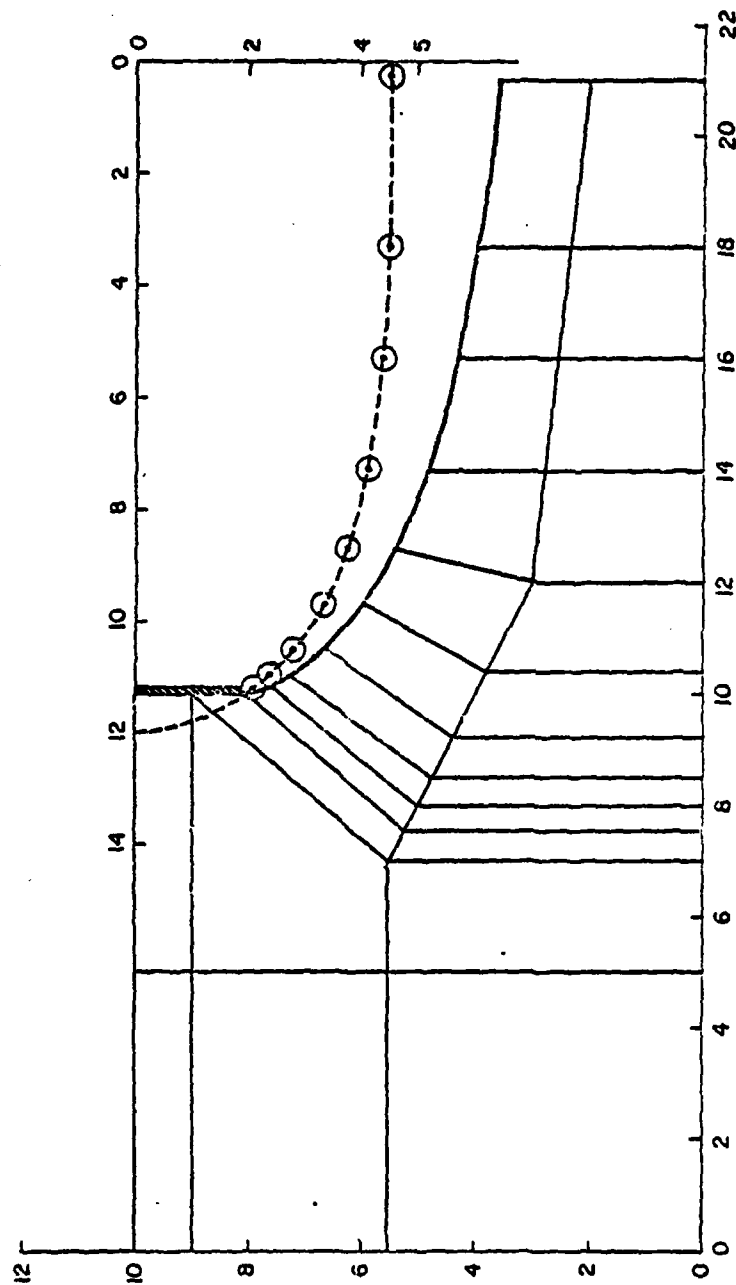


Figure 4.4 Demonstration of convergence of free-surface shifting algorithm

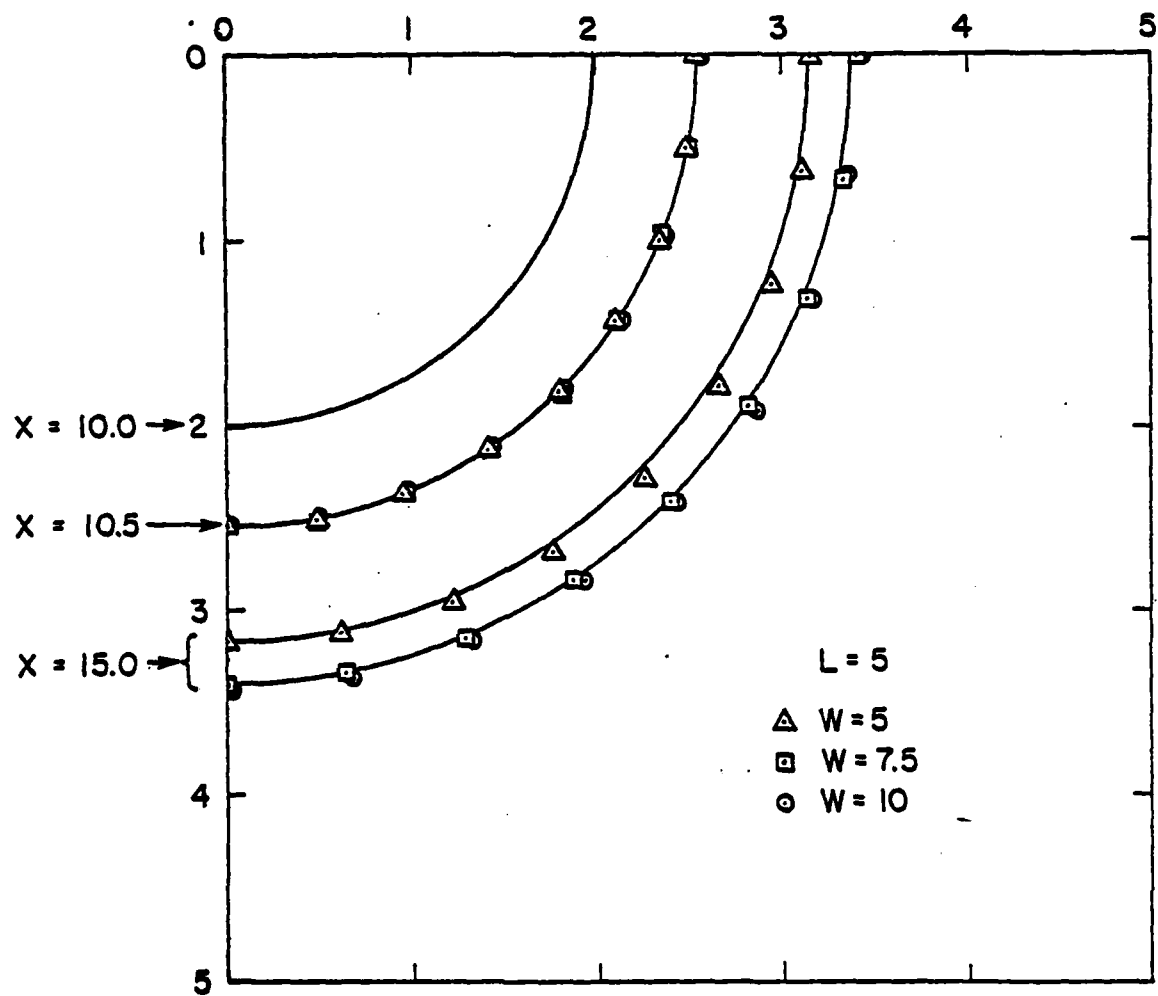


Figure 5.1 Variation of cavity shape with tunnel width and plate diameter ratio.  $P = 2$ ;  $L = 5$ ; cross-sections just off disk and at cavity mid-section



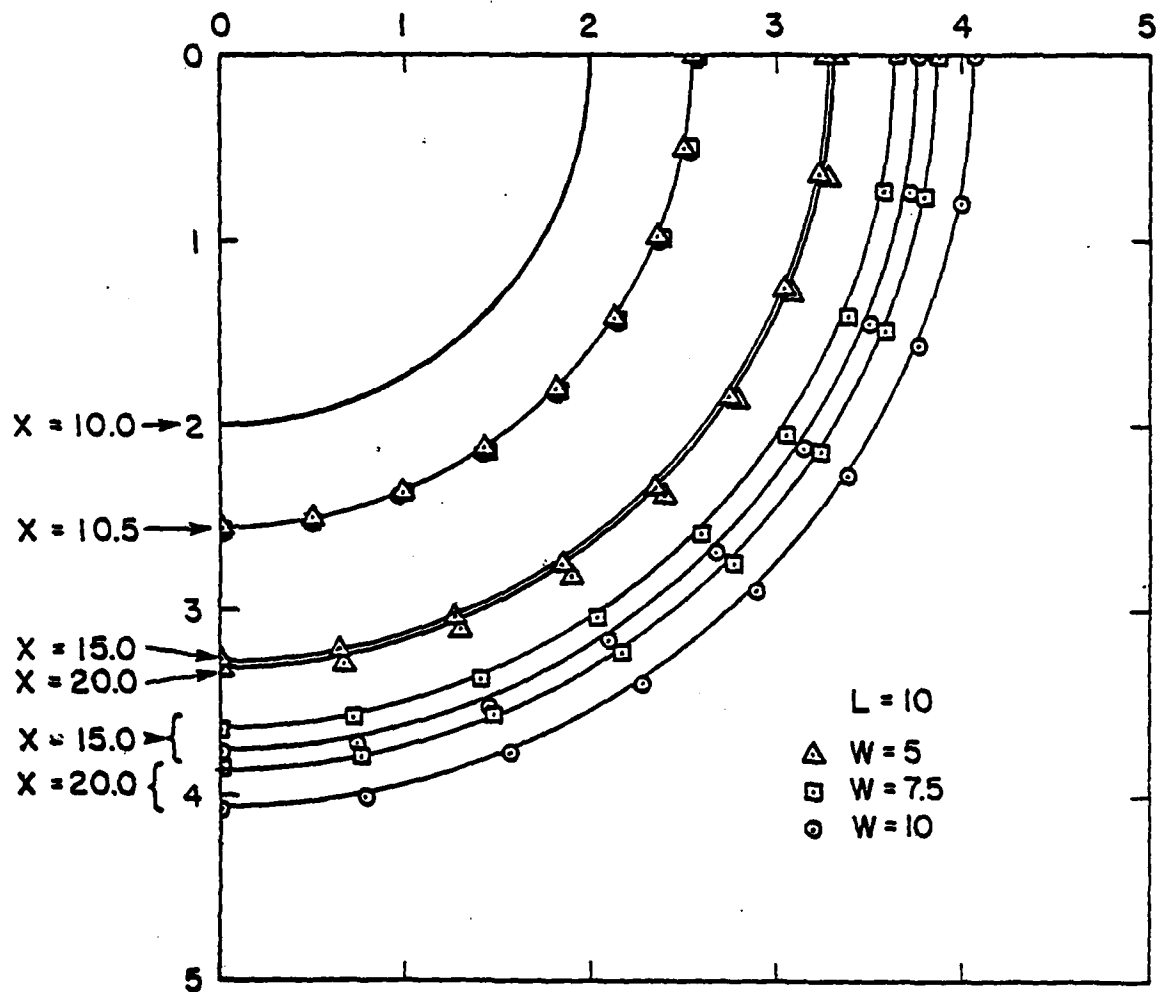


Figure 5.2 Variation of cavity shape with tunnel width and plate diameter ratio.  $P = 2$ ;  $L = 10$ ; cross-section just off disk and at cavity mid-section

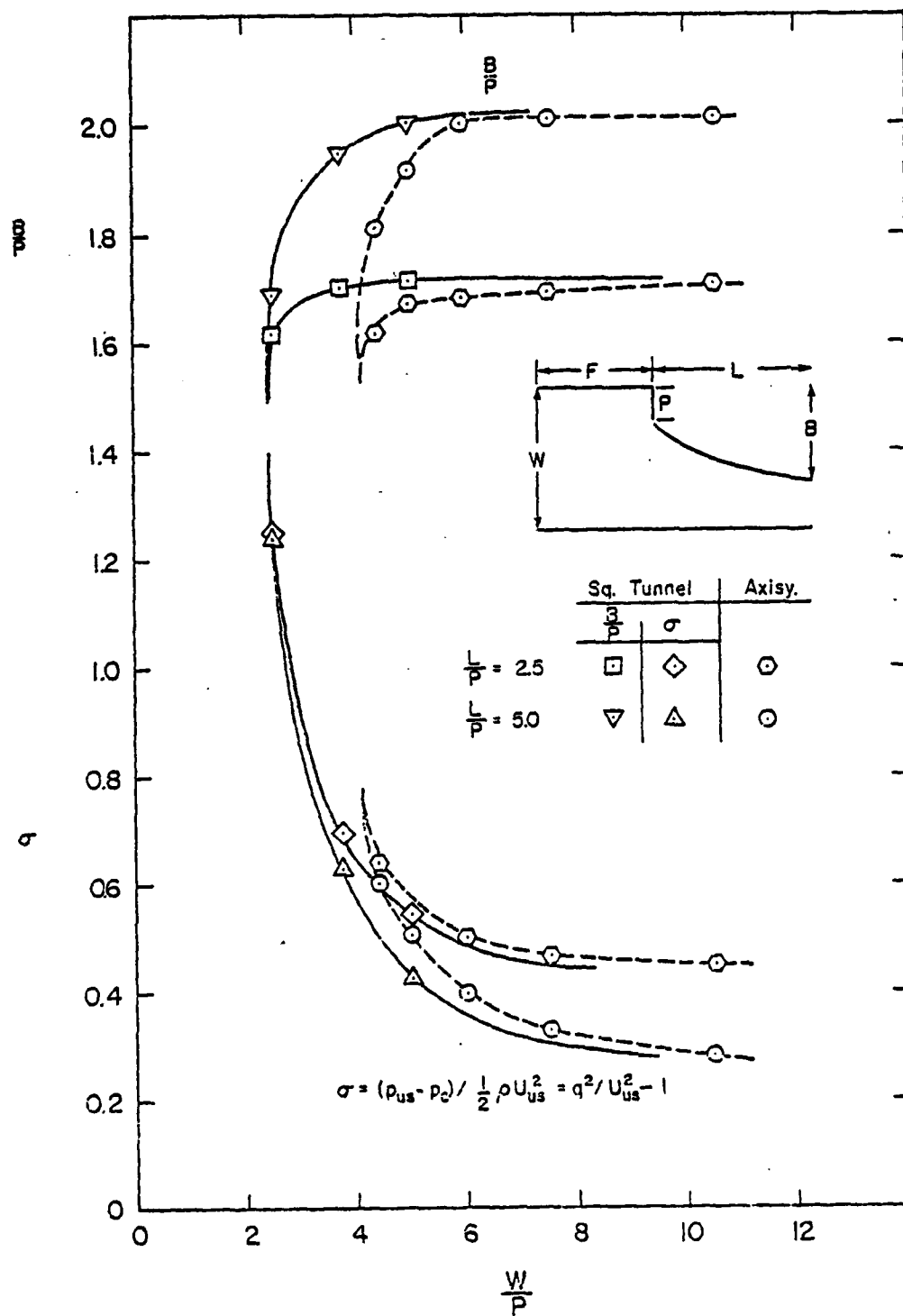


Figure 5.3 Variation of  $\sigma$  and cavity width with relative tunnel width -- the wall effect

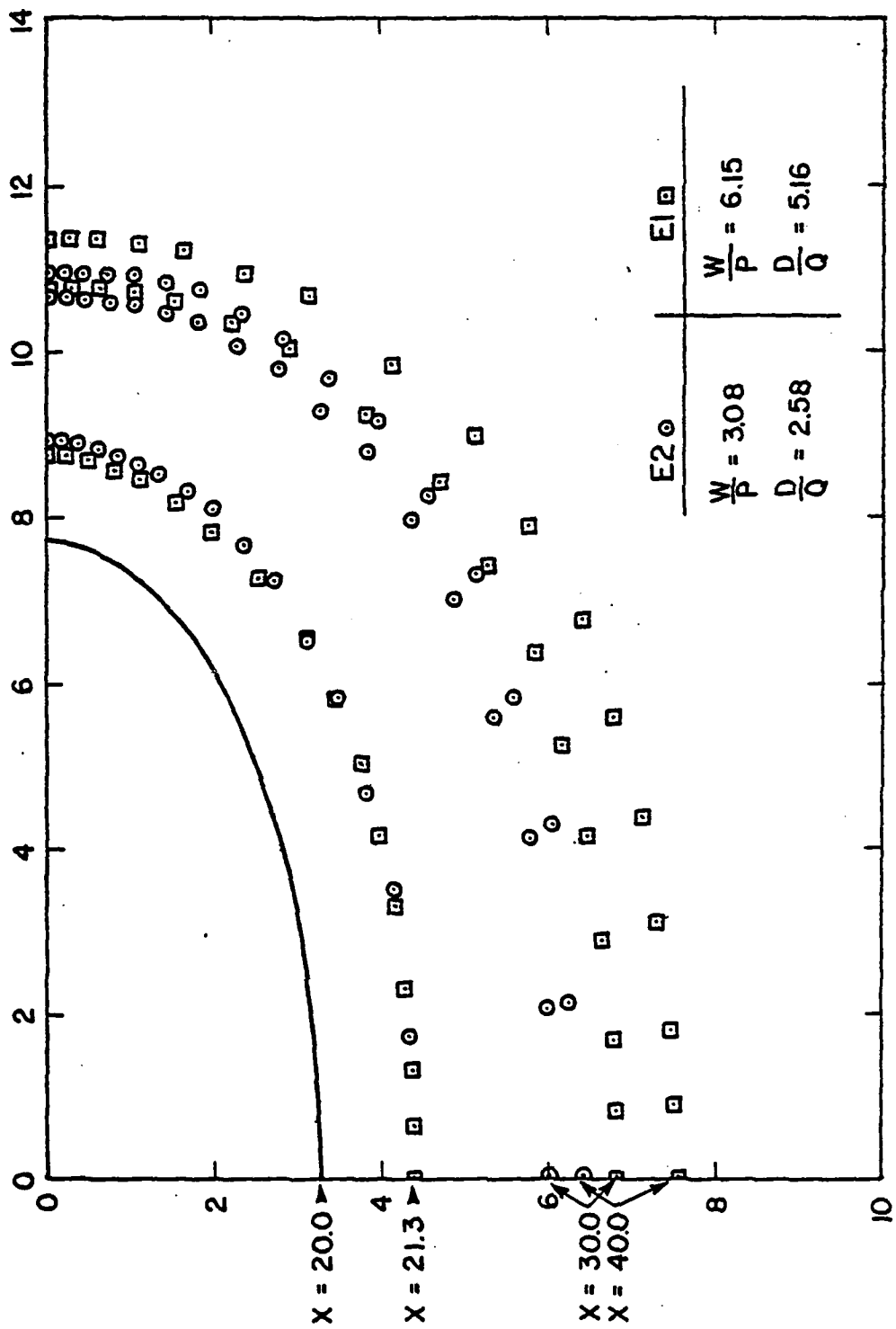


Figure 5.4 Variation of cavity shape with tunnel size and plate diameter ratio for elliptic plates. Cross-section just off disk and at cavity mid-section

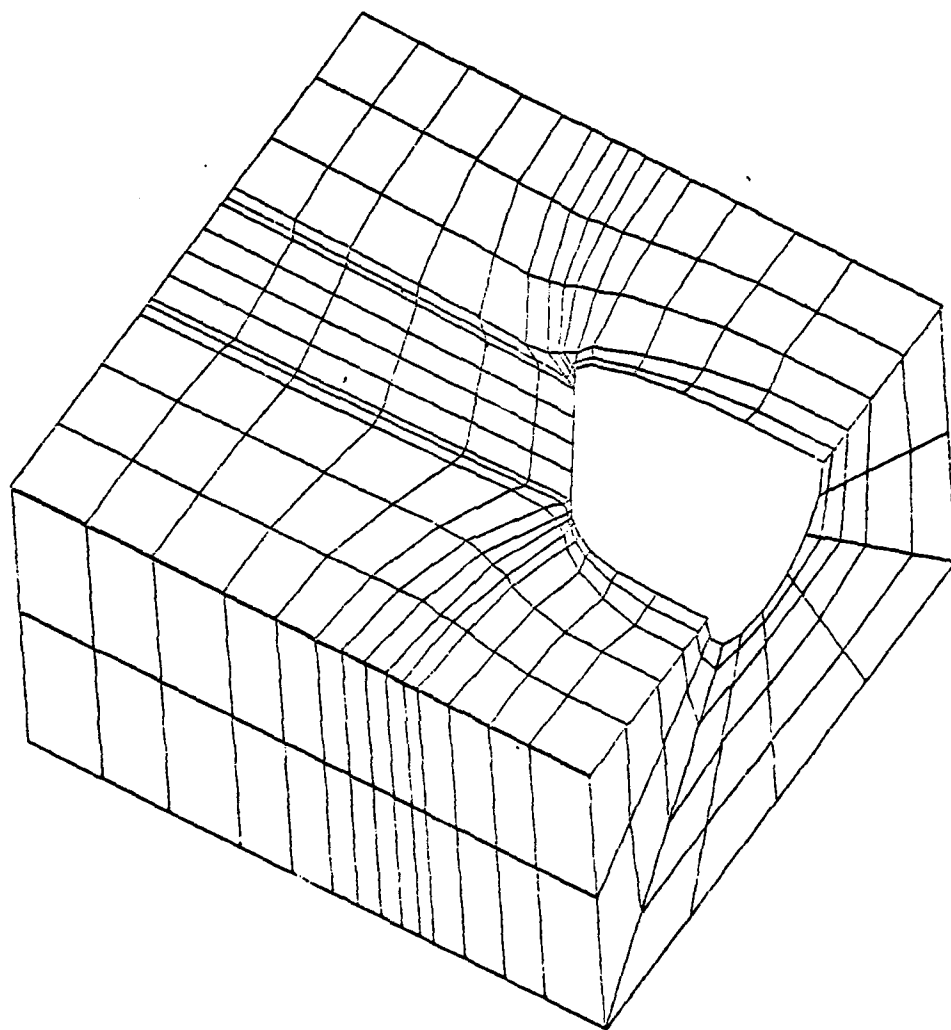


Figure 5.5     Finite element grid and configuration of three-dimensional  
lifting cavity flow; angle of attack =  $60^\circ$

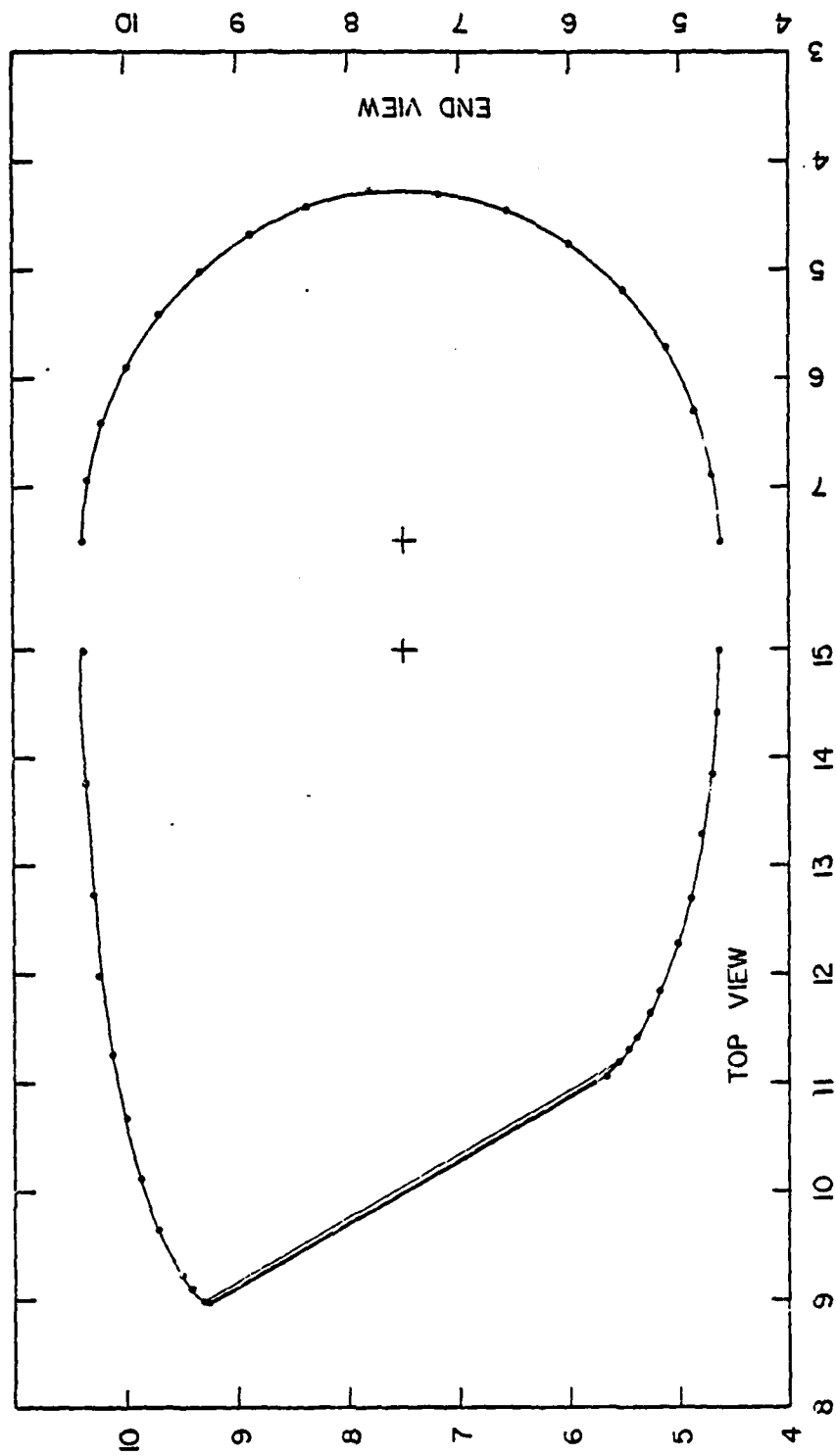


Figure 5.6 Final cavity shape for the lifting cavity flow with circular plate

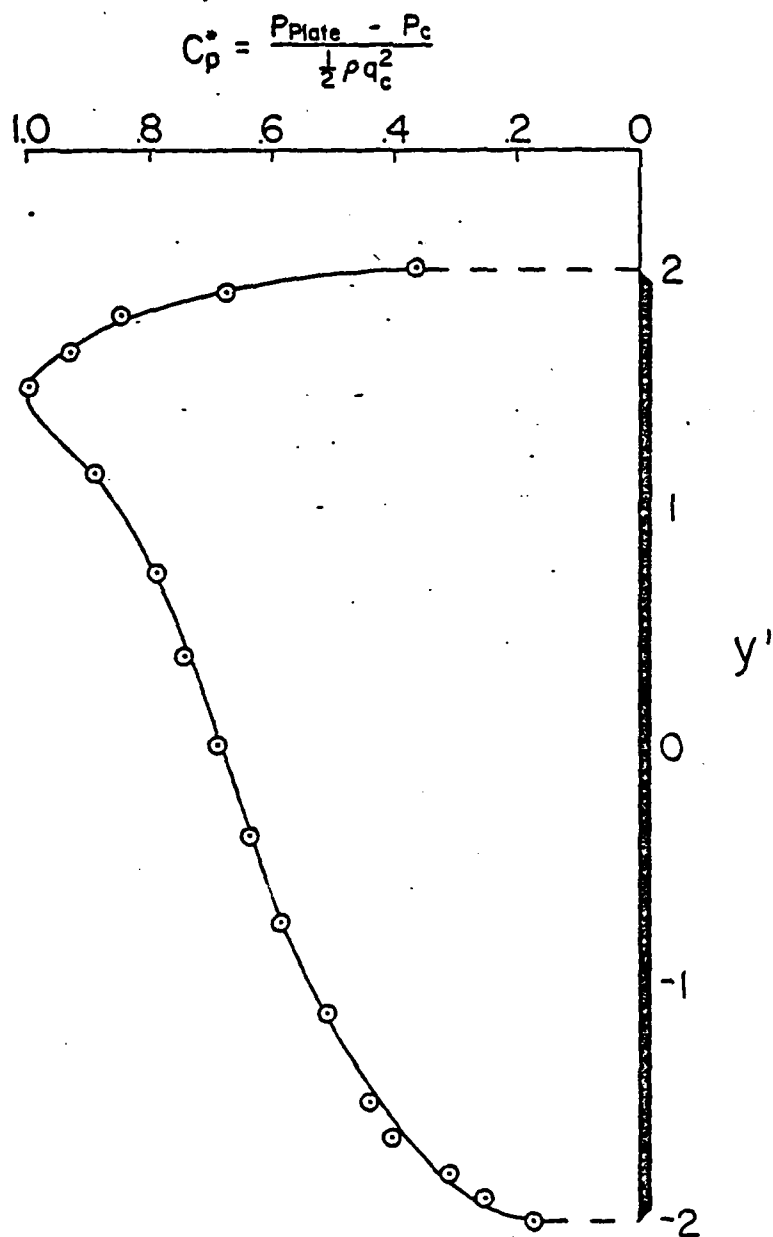


Figure 5.7 Pressure distribution along the centerline of the plate;  
angle of attack =  $60^\circ$

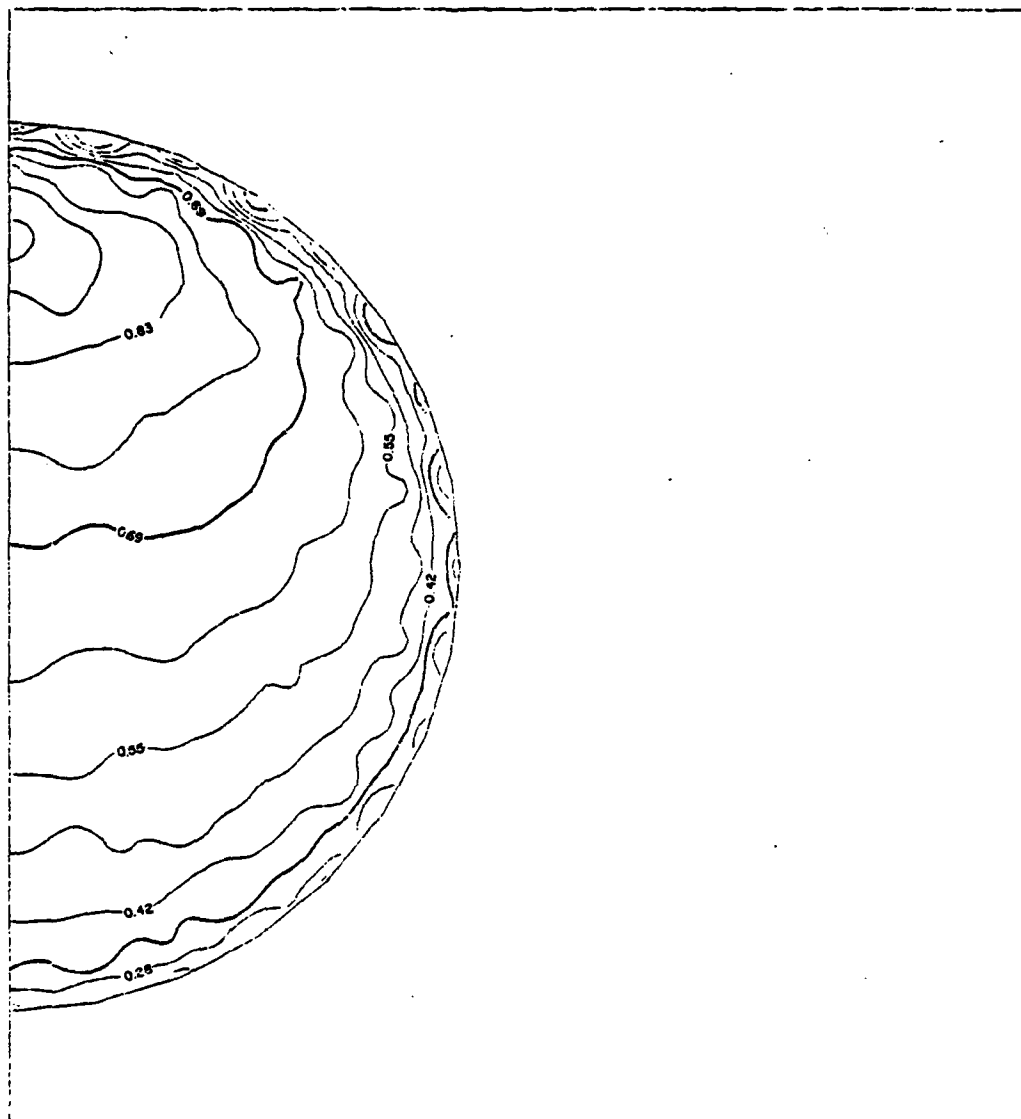


Figure 5.8 Pressure distribution  $C_p^*$  on plate; angle of attack =  $60^\circ$

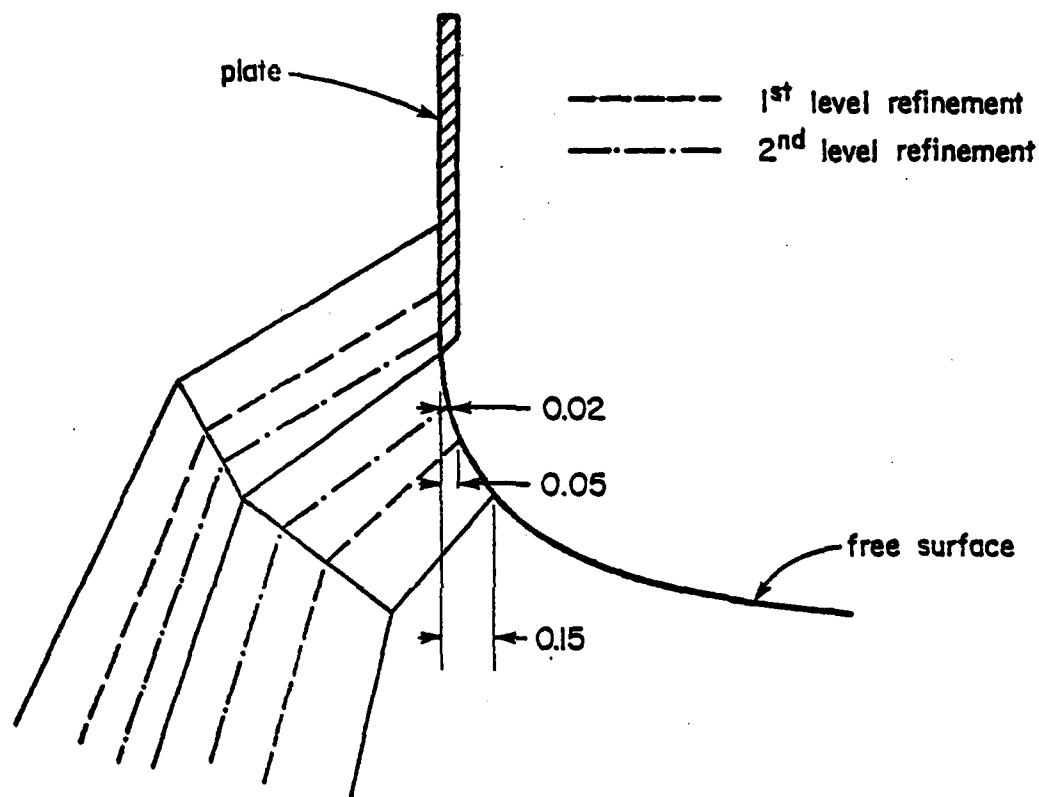


Figure 6.1 Grid refinement at separation



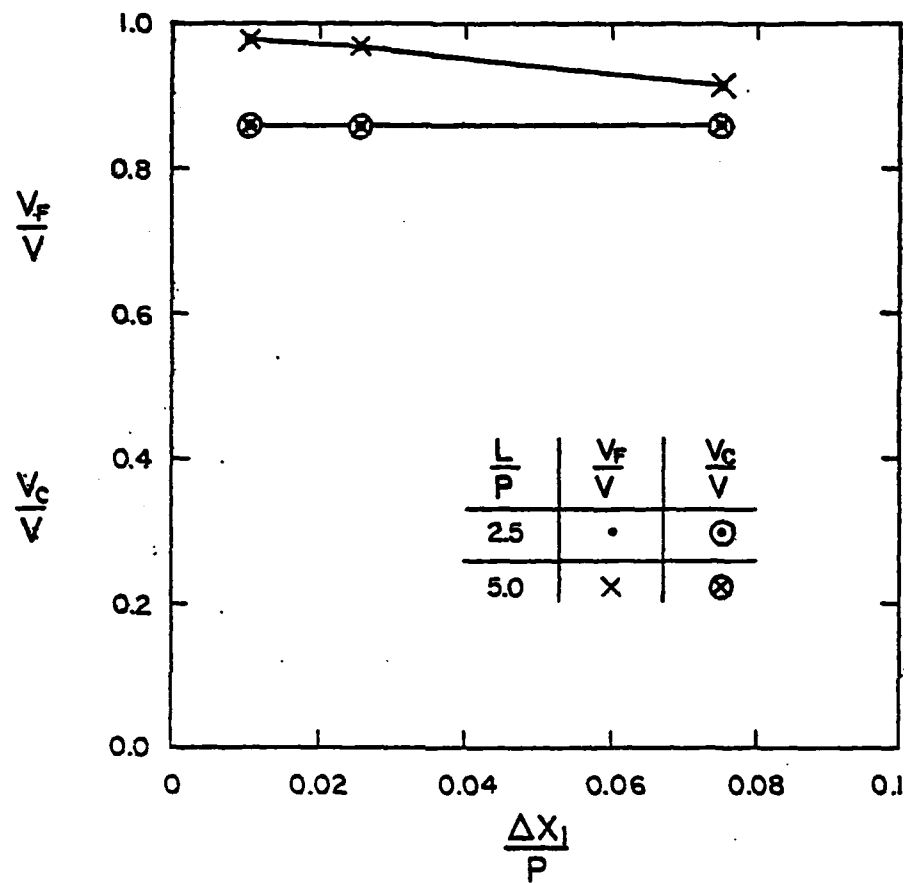


Figure 6.2 Effect of grid refinement near separation in circular-plate pure-drag cases:  $W/P = 2.5$ ;  $\sigma = 1.25$

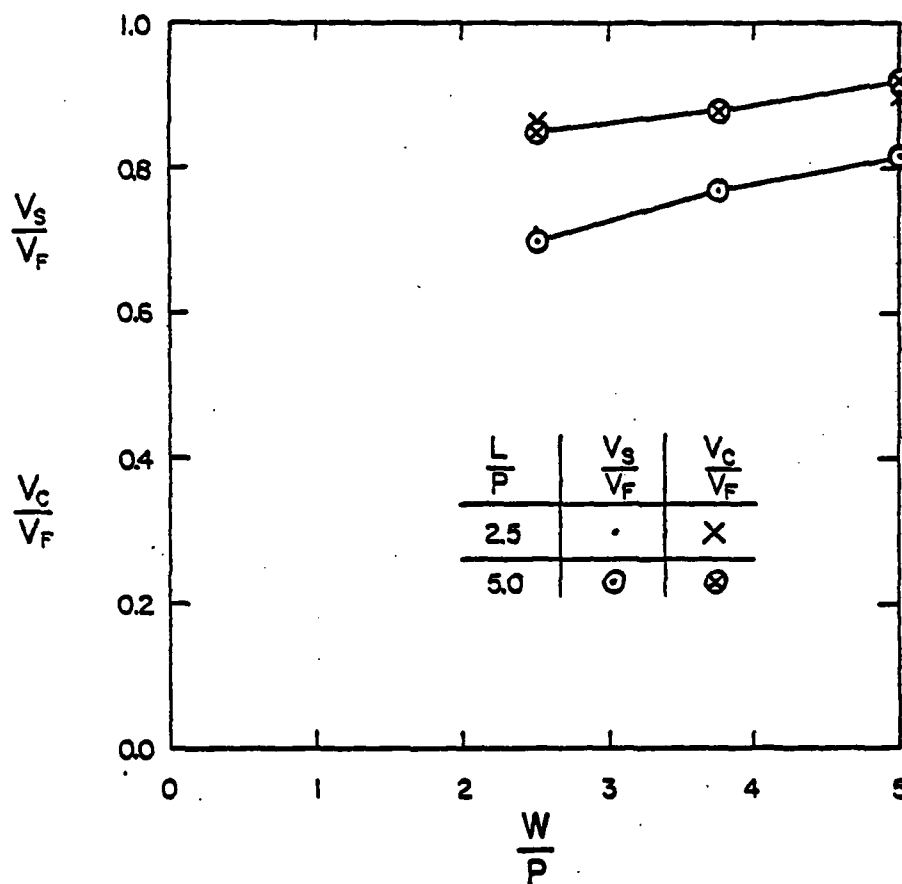


Figure 6.3 Effect of tunnel size on separation velocities in circular-plate pure drag cases:  $\Delta x_1 P = 0.075$

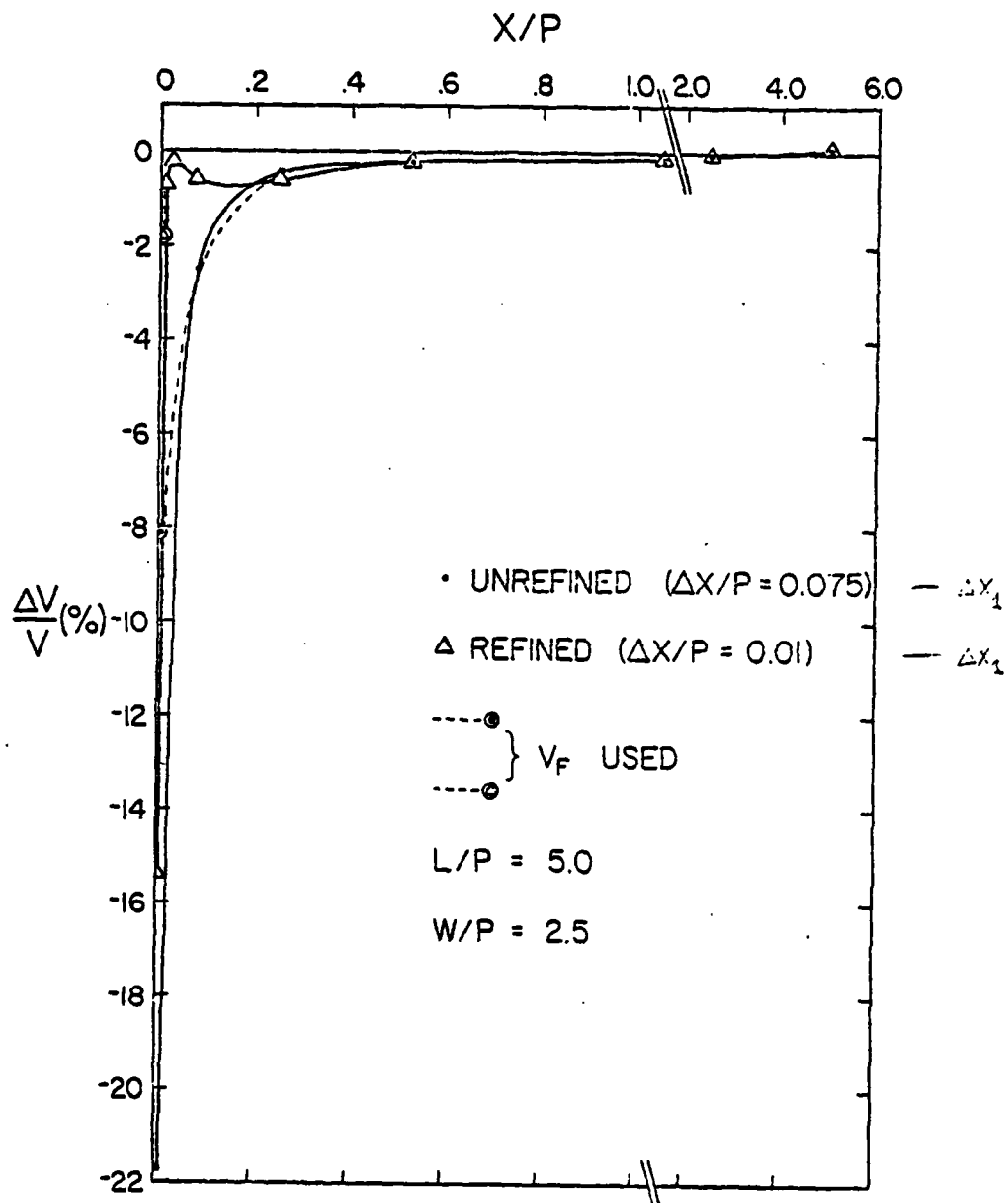


Figure 6.4 Variation of freestream velocity  $V_{fs}$  (as a percentage difference from the average freestream velocity) for a circular plate pure drag case

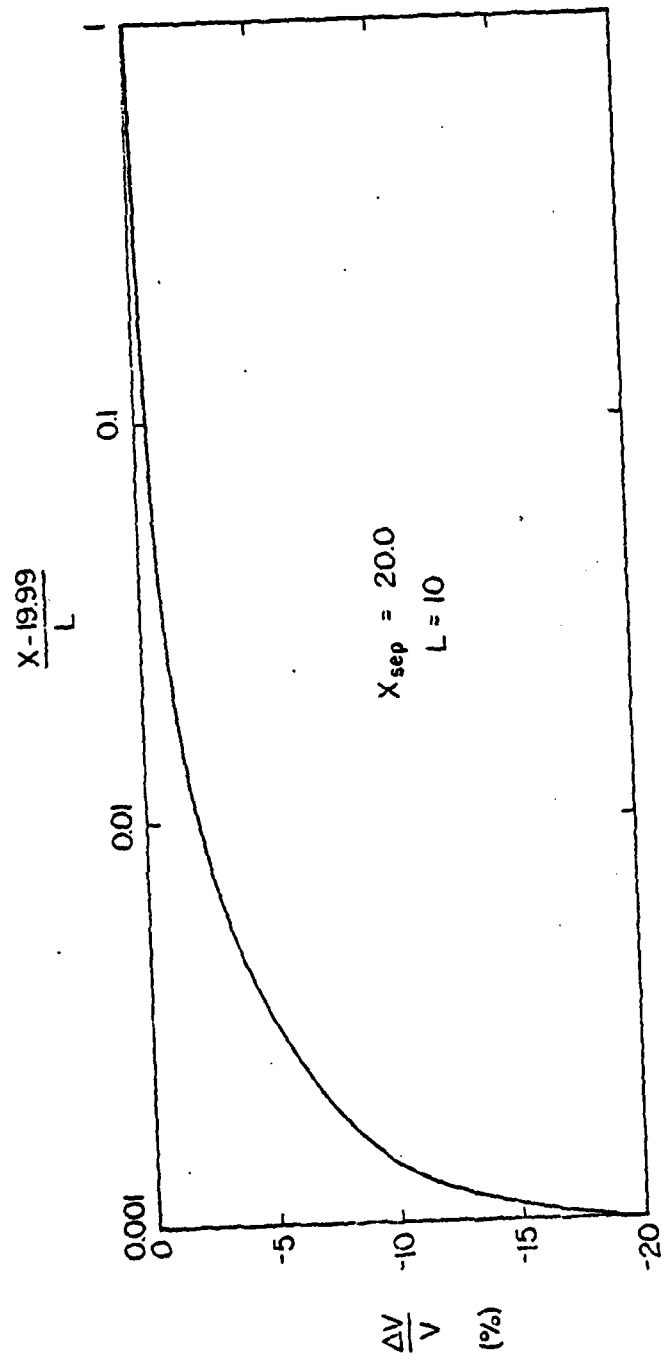
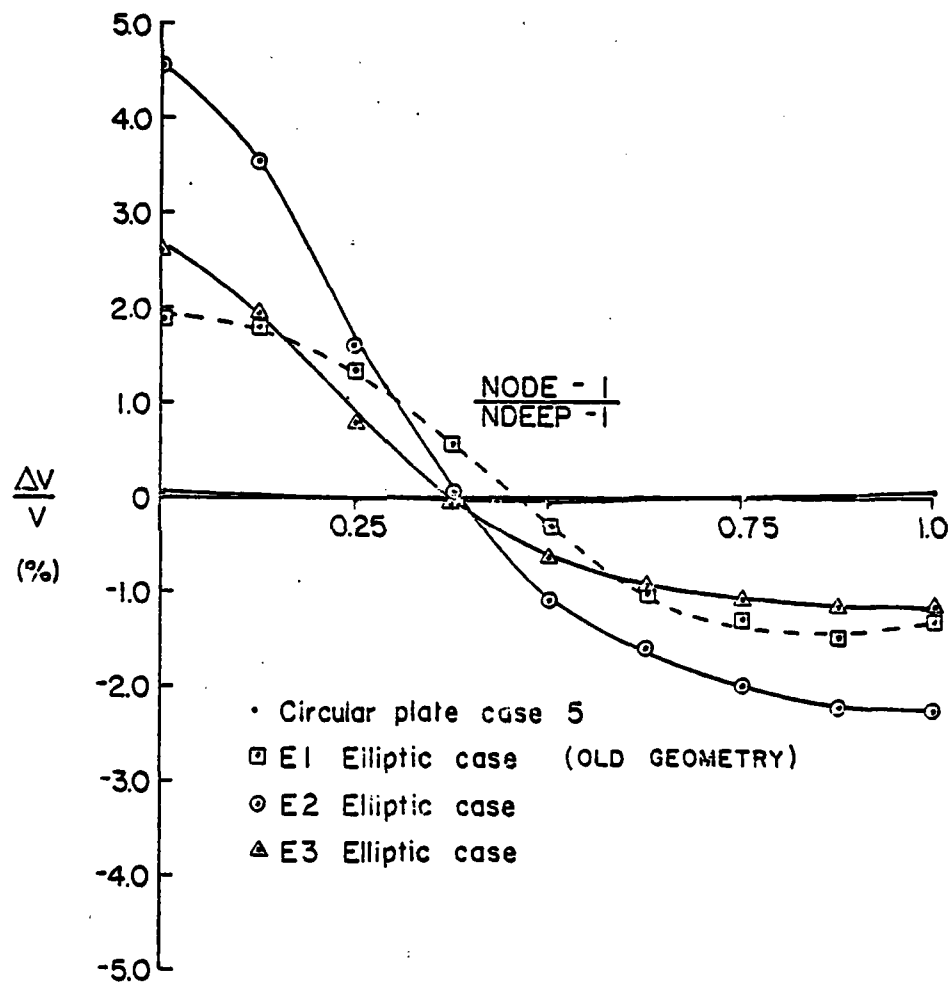


Figure 6.5 Variation of freestream velocity  $V_{\infty}$  for elliptic case E2



**Figure 6.6** Pure drag cases: variation of freestream velocity across end of cavity (as a difference percentage from the average free-stream velocity)

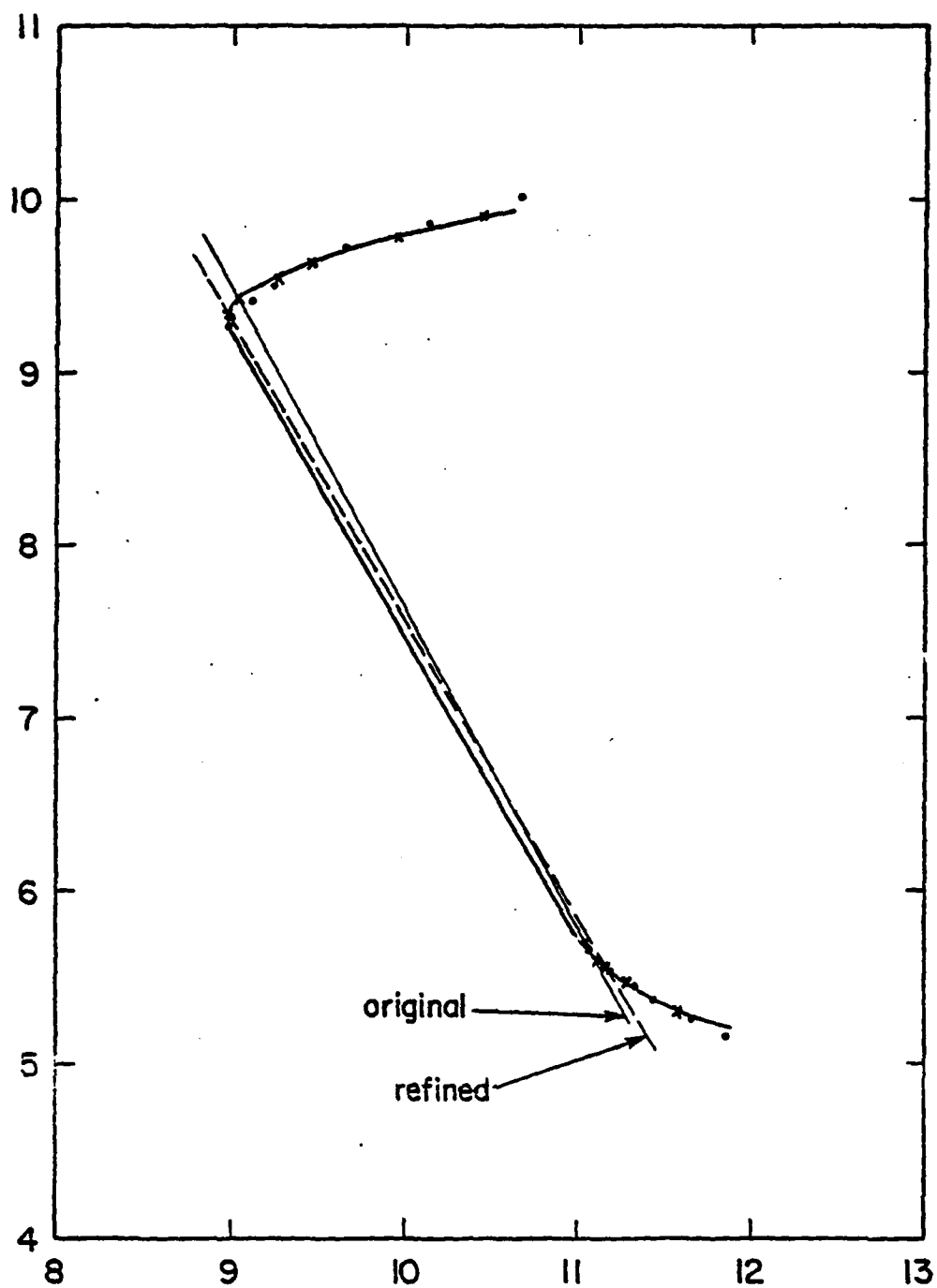


Figure 6.7 Grid refinement for lifting plate case

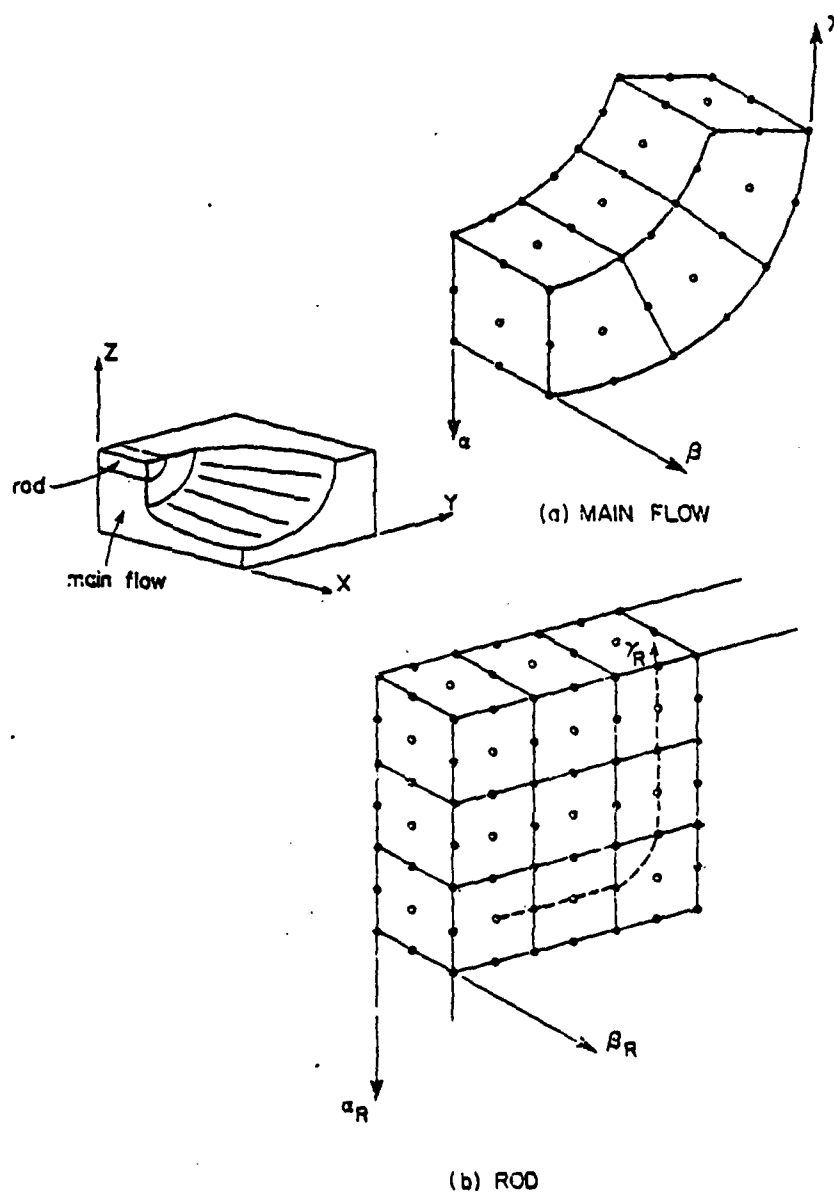


Figure A.1.1 Curvilinear axes for node numbering: (a) main flow section  
(b) rod section





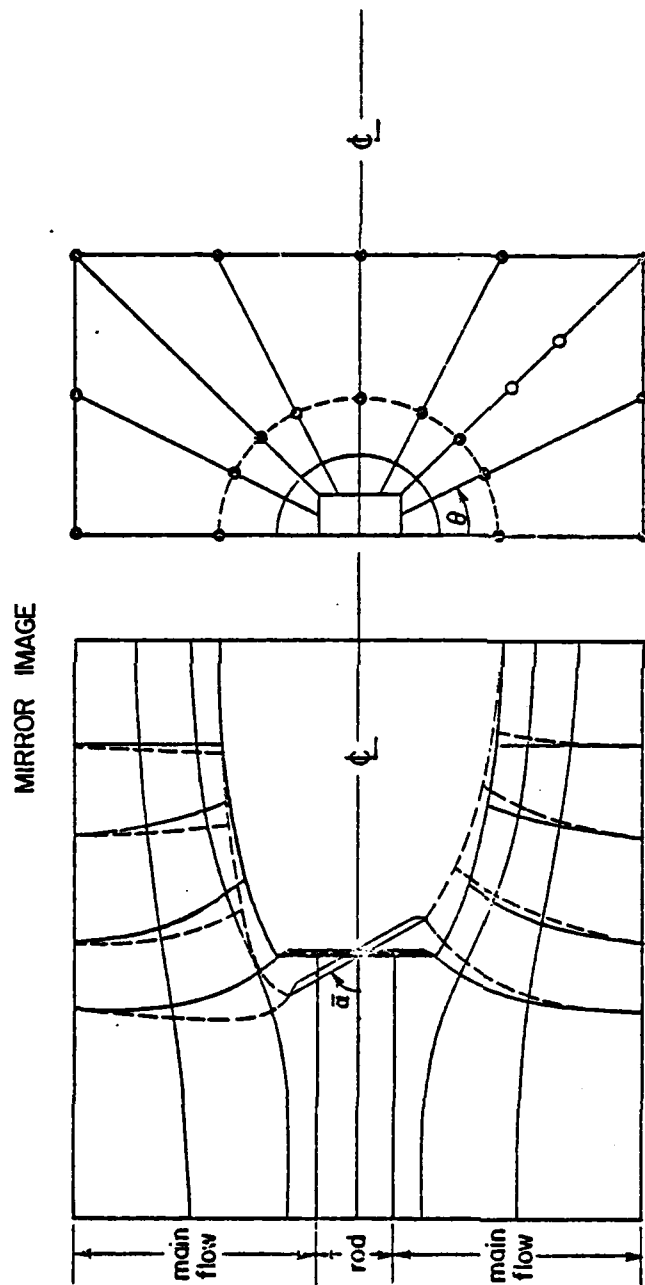


Figure A.1.3 Schematic of the geometry generation procedure for lifting flow

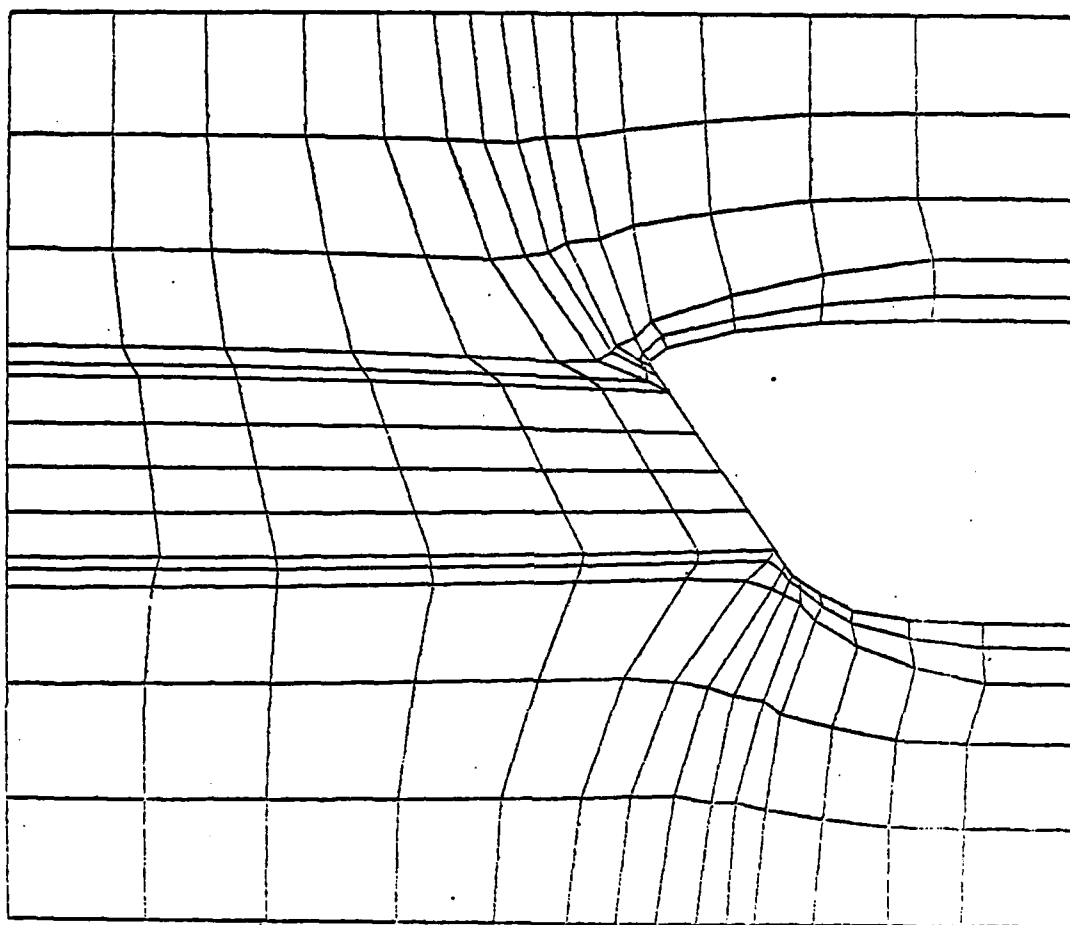


Figure A.1.4 Top view of a typical grid for lifting flow; angle of attack of  $60^\circ$

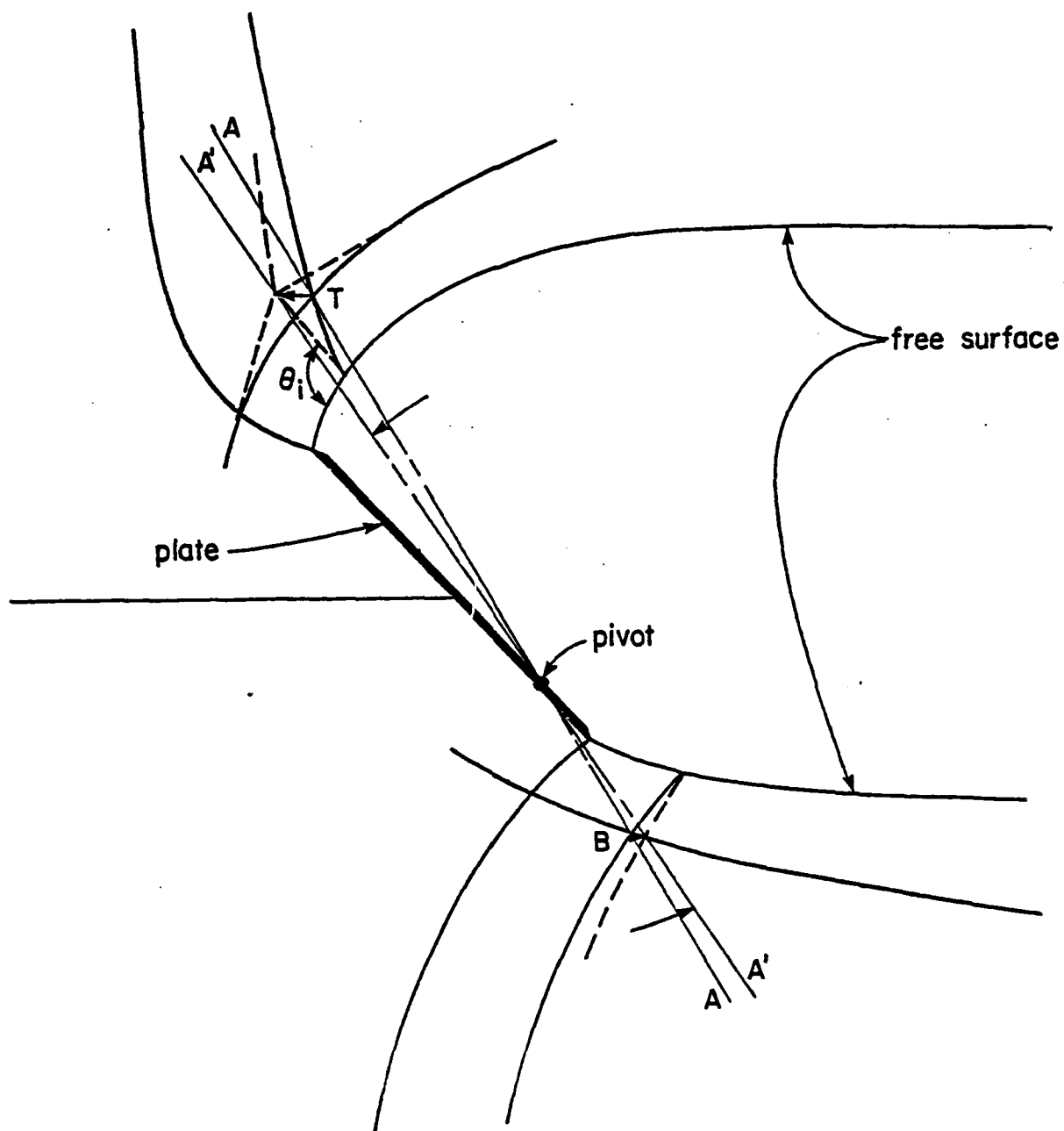
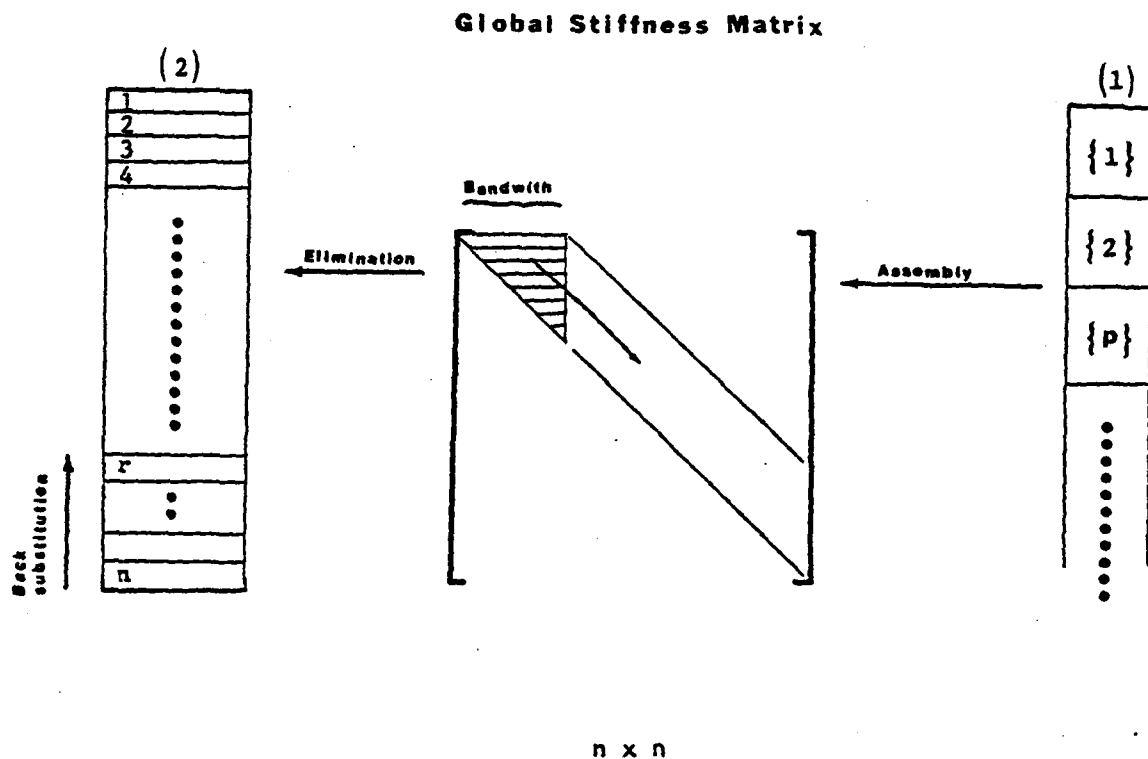


Figure A.1.5 Schematic of semi-manual grid adjustment at the separation for the lifting flow




- $n$  = number of node points
- (1) = disk file for the element stiffness matrices
- (2) = disk file for temporary storage
-  = core storage required
- $\{p\}$  = nodal connection matrix and elemental stiffness matrix for  $p$ th element
- $r$  = resulting values for the  $r^{\text{th}}$  equation of the Global Stiffness Matrix

Figure A.2.1 Schematic diagram showing the data structure for direct method which uses Gaussian Elimination

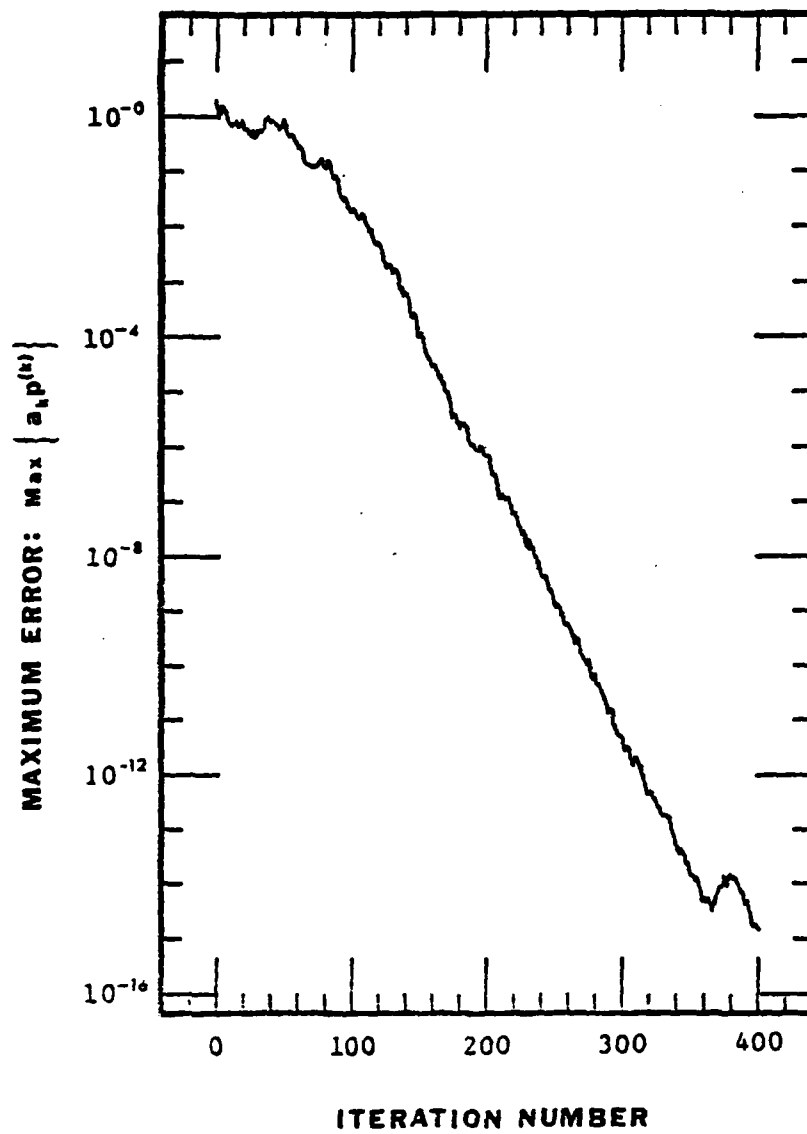


Figure A.2.2 Maximum error as defined in Step 3 of CG algorithm versus iteration number for the test problem

UNCLASSIFIED

SECURITY CLASSIFICATION OF THIS PAGE (When Data Entered)

REPORT DOCUMENTATION PAGE		READ INSTRUCTIONS BEFORE COMPLETING FORM
1. REPORT NUMBER TR 241	2. GOVT ACCESSION NO.	3. RECIPIENT'S CATALOG NUMBER
4. TITLE (and Subtitle) FINITE ELEMENT SIMULATION OF SIMPLE THREE- DIMENSIONAL FULLY CAVITATING FLOWS.		5. TYPE OF REPORT & PERIOD COVERED Final <del>18 October 1974</del> - 31 December 1979
6. AUTHOR(s) Peter Y. Ko (Now at George Washington Univ.) Robert L. Street		7. PERFORMING ORG. REPORT NUMBER TR-241
8. PERFORMING ORGANIZATION NAME AND ADDRESS Department of Civil Engineering Stanford University Stanford, California 94305		9. CONTRACT OR GRANT NUMBER(s) N00014-75-C-0277
10. CONTROLLING OFFICE NAME AND ADDRESS David W. Taylor Naval Ship R&D Center Bethesda, Md., 20084 (Code 1505)		11. PROGRAM ELEMENT, PROJECT, TASK AREA & WORK UNIT NUMBERS 61153N R0230101 SR 023 01 01
12. MONITORING AGENCY NAME & ADDRESS (if different from Controlling Office) Office of Naval Research 800 N. Quincy Street Arlington, Virginia 22217		13. REPORT DATE November 1979
14. DISTRIBUTION STATEMENT (of this Report) APPROVED FOR PUBLIC RELEASE; DISTRIBUTION UNLIMITED		15. NUMBER OF PAGES ix plus 110
15. DISTRIBUTION STATEMENT (of the abstract entered in Block 20, if different from Report)		16. SECURITY CLASS. (of this report) Unclassified
16. SUPPLEMENTARY NOTES This research was carried out under the General Hydromechanics Research Program (SR-023-01-01) of the Naval Sea Systems Command and administered by the David W. Taylor Naval Ship Research and Development Center, Code 1505, Bethesda, Md. 20084		17. DECLASSIFICATION/DOWNGRADING SCHEDULE
18. KEY WORDS (Continue on reverse side if necessary and identify by block number) GHR Program, cavitation, hydrofoils, digital computing, finite elements.		
19. ABSTRACT (Continue on reverse side if necessary and identify by block number) Based on potential flow theory, a formulation is given for three- dimensional fully cavitating flow with a Riabouchinsky model. The model is nonlinear and the location of the free surface of the cavity is not known priori. Therefore, an iterative procedure is used to locate the free surface boundary. The employment of a trial-free-boundary approach effectively reduces the fully nonlinear model to a linear one, and the solution at each iteration is obtained by means of the finite element method (FEM). Examples		

DD FORM 1473  
1 JAN 73EDITION OF 1 NOV 65 IS OBSOLETE  
S/N 0102 LF 014 6601

UNCLASSIFIED

SECURITY CLASSIFICATION OF THIS PAGE (When Data Entered)

UNCLASSIFIED

SECURITY CLASSIFICATION OF THIS PAGE(When Data Entered)

studied were fully cavitating flow past flat plates in a water tunnel. Results are given for pure drag flows past circular and elliptic plates and a lifting flow past a circular plate.

Three-dimensional, 20-node, quadratic isoparametric finite elements are used. The locations of the mid-side nodes on the free-surface just off the edge of the plate are found to have significant effects on the separation condition which must be enforced while keeping the Jacobian of the isoparametric transformation nonsingular. The free surface is shown to be a characteristic surface and this leads to the development of a weighting scheme for assigning the free surface potential in the iterative scheme the shifting of the free surface. A new three-dimensional "local" interpolation scheme for the location of the mid-side nodes is also developed for the lifting flow configuration.

The various algorithms were tested against known analytic solutions as well as published numerical and experimental results in two-dimensional and axisymmetric flows. Results from several pure-drag three-dimensional geometries are presented and the cavity shapes and the tunnel wall effects are examined. Then lifting flow results are given.

Because of the change in flow boundary conditions at the separation edge and the failure of the FEM to resolve these conditions accurately, the ability of the numerical solution to maintain a constant pressure over the entire cavity decreases as the three dimensionality of the free surface increases. However, the present procedure produces absolutely stable iterations and shows no sign of drifting of the free surface. It is found that satisfaction of a tangent separation condition of the free surface from the flat plate body is crucial for the stability of the iterative procedure. Grid refinement in both the streamwise and transverse directions reduces the computational error. While free surface movement between iterations is a useful convergence criterion, a flow-rate balance between upstream and downstream cross-sections appears not to be a good criterion. Finally, alternate formulations which may reduce the difficulties encountered are discussed.

UNCLASSIFIED

SECURITY CLASSIFICATION OF THIS PAGE(When Data Entered)